SUBTASK 1.1 – ADVANCED CHARACTERIZATION OF UNCONVENTIONAL OIL AND GAS RESERVOIRS TO ENHANCE CO_2 STORAGE RESOURCE ESTIMATES

Topical Report

(for the period of May 1, 2016 – April 30, 2019)

Prepared for:

AAD Document Control

National Energy Technology Laboratory
U.S. Department of Energy
626 Cochrans Mill Road
PO Box 10940, MS 921-107
Pittsburgh, PA 15236-0940

Cooperative Agreement No. DE-F0024233
DOE Technical Monitor: Jerry Carr

Prepared by:

Alexander Azenkeng
Bethany A. Kurz
Blaise A.F. Mibeck
Steve A. Smith
Shane K. Butler
Kurt E. Eylands
Christopher J. Beddoe
Loreal V. Heebink
Charles D. Gorecki

Energy & Environmental Research Center
University of North Dakota
15 North 23rd Street, Stop 9018
Grand Forks, ND 58202-9018

2019-EERC-04-17 April 2019

EERC DISCLAIMER

LEGAL NOTICE This research report was prepared by the Energy & Environmental Research Center (EERC), an agency of the University of North Dakota, as an account of work sponsored by Red Trail Energy, the U.S. Department of Energy National Energy Technology Laboratory, and the North Dakota Industrial Commission. Because of the research nature of the work performed, neither the EERC nor any of its employees makes any warranty, express or implied, or assumes any legal liability or responsibility for the accuracy, completeness, or usefulness of any information, apparatus, product, or process disclosed or represents that its use would not infringe privately owned rights. Reference herein to any specific commercial product, process, or service by trade name, trademark, manufacturer, or otherwise does not necessarily constitute or imply its endorsement or recommendation by the EERC.

ACKNOWLEDGMENT

This report was prepared with the support of the U.S. Department of Energy (DOE) National Energy Technology Laboratory Cooperative Agreement No. DE-F0024233. However, any opinions, findings, conclusions, or recommendations expressed herein are those of the authors(s) and do not necessarily reflect the views of DOE.

DOE DISCLAIMER

This report was prepared as an account of work sponsored by an agency of the United States Government. Neither the United States Government, nor any agency thereof, nor any of their employees, makes any warranty, express or implied, or assumes any legal liability or responsibility for the accuracy, completeness, or usefulness of any information, apparatus, product, or process disclosed, or represents that its use would not infringe privately owned rights. Reference herein to any specific commercial product, process, or service by trade name, trademark, manufacturer, or otherwise does not necessarily constitute or imply its endorsement, recommendation, or favoring by the United States Government or any agency thereof. The views and opinions of authors expressed herein do not necessarily state or reflect those of the United States Government or any agency thereof.

TABLE OF CONTENTS

LIST OF FIGURES

Continued . . .

LIST OF FIGURES (continued)

LIST OF TABLES

SUBTASK 1.1 – ADVANCED CHARACTERIZATION OF UNCONVENTIONAL OIL AND GAS RESERVOIRS TO ENHANCE CO_2 STORAGE RESOURCE ESTIMATES

EXECUTIVE SUMMARY

The Energy & Environmental Research Center (EERC) developed methods and approaches for advanced characterization of unconventional oil and gas reservoirs to enhance CO_2 storage resource estimates using samples collected from organic-rich shales of the Bakken Formation. The project was funded under U.S. Department of Energy (DOE) Cooperative Agreement No. DE-FE0024233, with nonfederal cost share provided by Hitachi High Technologies America. The project participants included the EERC, Hitachi High Technologies America, the team at the National Energy Technology Laboratory's (NETL's) computed tomography (CT) scanning laboratory in Morgantown, West Virginia, and several NETL staff who have worked on CO_2 storage resource estimation.

Investigations on the use of subsurface geologic formations for CO_2 storage have been ongoing for many years. In the last decade, improvements in directional drilling technology and hydraulic fracturing of organic-rich shale and other tight rock formations have opened new opportunities for CO_2 storage, with the potential cobenefit of enhancing gas and oil recovery. Gas-bearing, organic-rich shales have been of particular interest as a carbon storage target because their ability to store large volumes of CO_2 is implied by their ability to store methane; however, estimating the CO_2 storage resource of organic-rich shales and other unconventional reservoirs is challenging because of the lack of detailed geologic and petrophysical data that are needed to develop improved volumetric equations. According to NETL's method for estimating regional-scale CO_2 storage resources, the key factors that control CO_2 storage in geologic formations include void space within induced fractures, natural fractures and matrix pores, as well as the occurrence and distribution of organic matter (OM) and clay minerals.[1]

A key goal of this effort was to use field emission scanning electron microscopy (FESEM) analysis of fine-grain unconventional reservoir rocks coupled with advanced image analysis and machine learning techniques to quantify the occurrence and distribution of porosity, OM, and clay minerals. By better understanding the potential migration pathways of CO_2 within tight rocks and quantifying the occurrence of sorptive components (OM and clays) along potential flow pathways, methods to estimate the CO_2 storage resource of such rocks can be refined. The Bakken petroleum system (Bakken) was used as the source of rock samples for this effort because it includes organic-rich shales with contrasting degrees of thermal maturity as well as tight, nonshale clastic rocks with varying clay mineral content.

To better understand the key components of interest in tight rock samples, the EERC worked closely with Hitachi to optimize the FESEM settings necessary to resolve the sample mineralogy, porosity and OM content at micro- to nanoscale resolution. The EERC also worked closely with Hitachi to apply and improve its advanced mineral identification and characterization system (AMICS) software so that it is better suited for mineral identification at the high resolution necessary to resolve features of interest in fine-grained rocks such as organic-rich shales.

[1] Goodman, A., Fukai, I., Dilmore, R., Frailey, S., Bromhal, G., Soeder, D., Gorecki, C., Peck, W., Rodosta, T., and Guthrie, G., 2014, Methodology for assessing CO_2 storage potential of organic-rich shale formations: Energy Procedia, v. 63, p. 5178–5184.

The EERC also applied advanced image analysis software packages, including Ilastik, to classify and quantify the key components of interest within the samples using FESEM imagery. These advanced techniques allowed for quantification and differentiation of the void space within fractures, pores and OM, as well as a technique to determine and quantify the key mineral and OM components surrounding pore spaces. Being able to better quantify the void space and the potential accessibility of CO_2 to sorptive minerals or OM within tight rocks allows for improved estimation of the CO_2 storage resource potential of organic-rich shales and other unconventional formations. The information derived from the image analysis techniques was used to refine NETL's method for estimating regional-scale CO_2 storage resources in collaboration with staff from NETL.

An additional goal of this work was to better understand rates of CO_2 permeation, flow pathways, and sorption in organic-rich shales and nonshale reservoir rocks and to evaluate potential changes in CO_2 flow over time. The EERC conducted long-duration (several weeks) CO_2 flow-through testing at reservoir conditions using Bakken shale and nonshale samples to assess CO_2 permeation rates and retention/sorption within core plugs to represent bulk matrix behavior. Conventional isothermal adsorption testing over a range of pressure conditions was also performed on pulverized Bakken samples to better assess potential maximum sorptive capacity of the samples. The results of this testing illustrated the higher sorptive capacity of the Bakken shales when compared to the sorptive capacity of the nonshale reservoir rock, which contains very little OM when compared to the Bakken shales. The results also illustrate the differences in permeation behavior as a function of fracture flow versus matrix flow.

In an attempt to visualize CO_2 permeation and flow behavior in Bakken shale samples over time, the EERC collaborated with NETL's CT Lab in Morgantown, West Virginia. A variety of tests were performed at the NETL lab on unfractured and fractured samples of the Bakken shale. The unfractured Bakken shale samples did not result in CO_2 migration within the samples over the testing duration; thus imagery of CO_2 migration pathways within the matrix of Bakken samples was not obtained. The results of the flow-through testing within fractured samples illustrate changes in CO_2 permeation rates over time, with a trend of decreasing CO_2 flow over time.

The results of this effort suggest that FESEM analysis coupled with advanced image analysis and machine learning techniques are effective in characterizing and quantifying the mineralogy, porosity, fractures, and OM content of 2-D imagery at the high resolution needed to identify features of interest in tight rocks. In addition, the image analysis techniques allow for identification and quantification of different porosity types as well as the key mineral components and/or OM that CO_2 would contact in the reservoir as it migrates through pores and fracture networks. This is key information needed to better estimate the CO_2 storage resource potential of organic-rich shales and other tight reservoirs.

Additional work is needed to determine the sorptive capacity of the individual sample components (OM and clay minerals) at reservoir conditions so that this approach and the refined CO_2 storage resource equation can be applied to other shale and unconventional reservoirs. In addition, subsequent work should be performed to better understand the number of images needed to use stereological approaches to estimate the volume of sample components using 2-D imagery, to explore machine learning techniques to differentiate between induced vs. natural fractures, and to estimate the connectivity of pores and fracture networks using 2-D imagery. Being able to derive this information at the microscale would facilitate scaling up of the sample characterization data used for reservoir modeling and simulation to estimate the CO_2 storage resource potential of tight formations.

SUBTASK 1.1 – ADVANCED CHARACTERIZATION OF UNCONVENTIONAL OIL AND GAS RESERVOIRS TO ENHANCE CO_2 STORAGE RESOURCE ESTIMATES

BACKGROUND

Investigations on the use of subsurface geologic formations for carbon dioxide (CO_2) storage have been ongoing for many years. Of specific interest has been the use of saline aquifers, depleted oil and gas formations, and unminable coal seams (Goodman and others, 2014; U.S. Department of Energy National Energy Technology Laboratory, 2012). Injection of CO_2 into any of these sinks has the potential to facilitate a decrease in atmospheric CO_2 concentrations, thereby helping to meet short- and long-term CO_2 reduction goals. In the last decade, improvements in directional drilling technology (Watney, 2016) and hydraulic fracturing (King, 2010) of organic-rich shale and other tight rock formations have opened new opportunities for CO_2 storage, with the potential cobenefit of enhancing gas and oil recovery. Gas-bearing, organic-rich shales have been of particular interest as a carbon storage target because their ability to store large volumes of CO_2 is implied by their ability to store methane (Goodman and others, 2014; Godec and others, 2013).

Although significant progress has been made globally to investigate the suitability of subsurface geologic sinks for CO_2 storage (Preston and others, 2005; Torp and Gale, 2004; Chadwick and others, 2004; Hamling and others, 2013), estimating the storage resource of emerging reservoir types such as organic-rich shale formations faces serious challenges (Goodman and others, 2014). One of the unresolved difficulties with organic-rich shales, as pointed out by Goodman and others (2014), is the lack of detailed geologic and petrophysical data that are needed to develop improved volumetric equations for assessing the CO_2 storage resource of such formations. According to the U.S. Department of Energy (DOE) National Energy Technology Laboratory (NETL) method for estimating regional-scale CO_2 storage resources, the key factors that control CO_2 storage in geologic formations include void space within induced fractures, natural fractures and matrix pores, as well as the occurrence and distribution of kerogen and clay minerals (Goodman and others, 2014). Because it is difficult to differentiate between free-phase CO_2 storage in fractures versus pore space, currently the total void space available for free-phase storage is grouped into a total porosity parameter in the equation used to estimate the mass CO_2 storage resource for organic-rich shale formations. Similarly, the capacity of the solid fraction of the shale to sorb CO_2 is described by a parameter that groups the sorptive capacity of clay minerals and kerogen. In addition, because very little work has been conducted to better understand the accessibility and/or interconnectedness of the void space within fractures and pores for CO_2 storage or how accessible kerogen or clay minerals are to CO_2 contact, efficiency factors are used to estimate the fraction of void space available for CO_2 storage or the fraction of solid volume that will effectively sorb CO_2 (Goodman and others, 2014).

One of the key challenges in estimating the various parameters that affect CO_2 storage in organic-rich shale reservoirs is that the experimental techniques and/or analytical equipment and methods used to evaluate conventional reservoirs are limited and/or are unsuitable when applied to shales and other tight rocks with pore and grain sizes that can be in the nanometer scale,

permeability in the micro- to nanodarcy range (Kwon and others, 2004), and porosity typically <10% (Erdman and Drenzek, 2013). For example, Kang and others (2011) conducted an evaluation of Barnett shale core samples for CO_2 storage potential and found that the kerogen particles within the organic-rich shale contain nanoscale pore networks that could account for 60% to 97% of the adsorbed CO_2; however, nanoscale pore networks are not features that can be detected by standard analytical techniques such as conventional scanning electron microscopy (SEM). The presence of porosity networks too small to detect by conventional analytical techniques could explain why previous work funded by NETL and conducted by the Energy & Environmental Research Center (EERC) to evaluate the ability of CO_2 to extract oil from organic-rich shales in the Bakken Formation suggested that CO_2 was able to access and extract much more oil from the samples than would be expected from such low-permeability and low-porosity samples (Hawthorne and others, 2013, 2014). Similarly, detailed mineralogical characterization in tight rocks is difficult using conventional analytical techniques such as SEM, x-ray diffraction (XRD), and optical microscopy because of the abundance of very fine clay grain/particle sizes, coupled with extremely lithified rock matrices. Understanding the occurrence and type of clay within these formations is important for better estimating the sorptive capacity of the rock matrix. Clay type and occurrence are also important because clay mobility and/or clay swelling have been observed to cause a significant reduction in permeability (Gray and Rex, 1966; Das and Mehdi, 2015) where the mobilized clay particles cause plugging or swollen clays create increased resistance to flow.

To improve our understanding of the key geologic factors that influence CO_2 storage resource estimates in organic-rich shales and other unconventional reservoirs, a key goal of this effort was to use field emission scanning electron microscopy (FESEM) analysis of fine-grain unconventional reservoir rocks coupled with advanced image analysis and machine learning techniques to quantify the occurrence and distribution of porosity, fractures, OM (organic matter), and clay minerals. By better understanding the potential migration pathways of CO_2 within tight rocks and quantifying the occurrence of sorptive components (OM and clays) along potential flow pathways, methods to estimate the CO_2 storage resource of such rocks can be refined. This work was an extension of ongoing efforts at the EERC to better understand the opportunities that may be available for CO_2 storage in unconventional reservoirs such as organic-rich shales. Although more emphasis was placed on Bakken shales as a classic example of organic-rich shales in a tight oil reservoir in North America, a Marcellus gas-rich shale sample was characterized to demonstrate the applicability of the methods to other shale formations.

The major objectives of the study included:

- Development of advanced FESEM and image analysis methods to better characterize the mineralogy and OM content of organic-rich shales and other tight formations.

- Development of advanced image analysis methods to better estimate porosity and pore-size distributions in organic-rich shales and other tight formations.

- Development of improved methods to estimate the storage resource potential of unconventional formations.

- Evaluation and quantification of CO_2 permeation and sorption in Bakken shale and reservoir samples.

Samples from the Bakken Formation were used in the study as an analogue for both organic-rich shales as well as tight, nonshale reservoir rocks. The Bakken is characterized by several distinctive lithofacies, each with its own unique properties that may (or may not) significantly affect the mobility and ultimate fate of CO_2 within the formation. The lithofacies of the Bakken can be broadly divided into two groups: the shale group, which includes the Upper and Lower Bakken Shale Members (UBS and LBS, respectively), and the nonshale group, which includes the many lithofacies of the Middle Bakken (MB) Member. The fine-grained clastics and carbonates of the MB are representative of a tight, fractured reservoir rock that is capable of transmitting fluids once it has been hydraulically fractured. In North Dakota and Montana, the MB typically comprises between three and seven distinctly different lithofacies that range from silty carbonates to calcite/dolomite cemented siltstones. In most areas of the Bakken Formation, the MB is bounded above by the UBS and below by the LBS. Both shale members are organic-rich, typically oil-wet shales that are the source rocks for the productive areas of the Bakken (Figure 1). Some of the key challenges associated with characterization of the Bakken include low porosity (typically <10%), low permeability (typically <1 mD), very fine grain minerals (4 to 60 μm), and clay-size particles (<4 μm) that are hard to resolve both chemically and physically, and a high degree of rock heterogeneity.

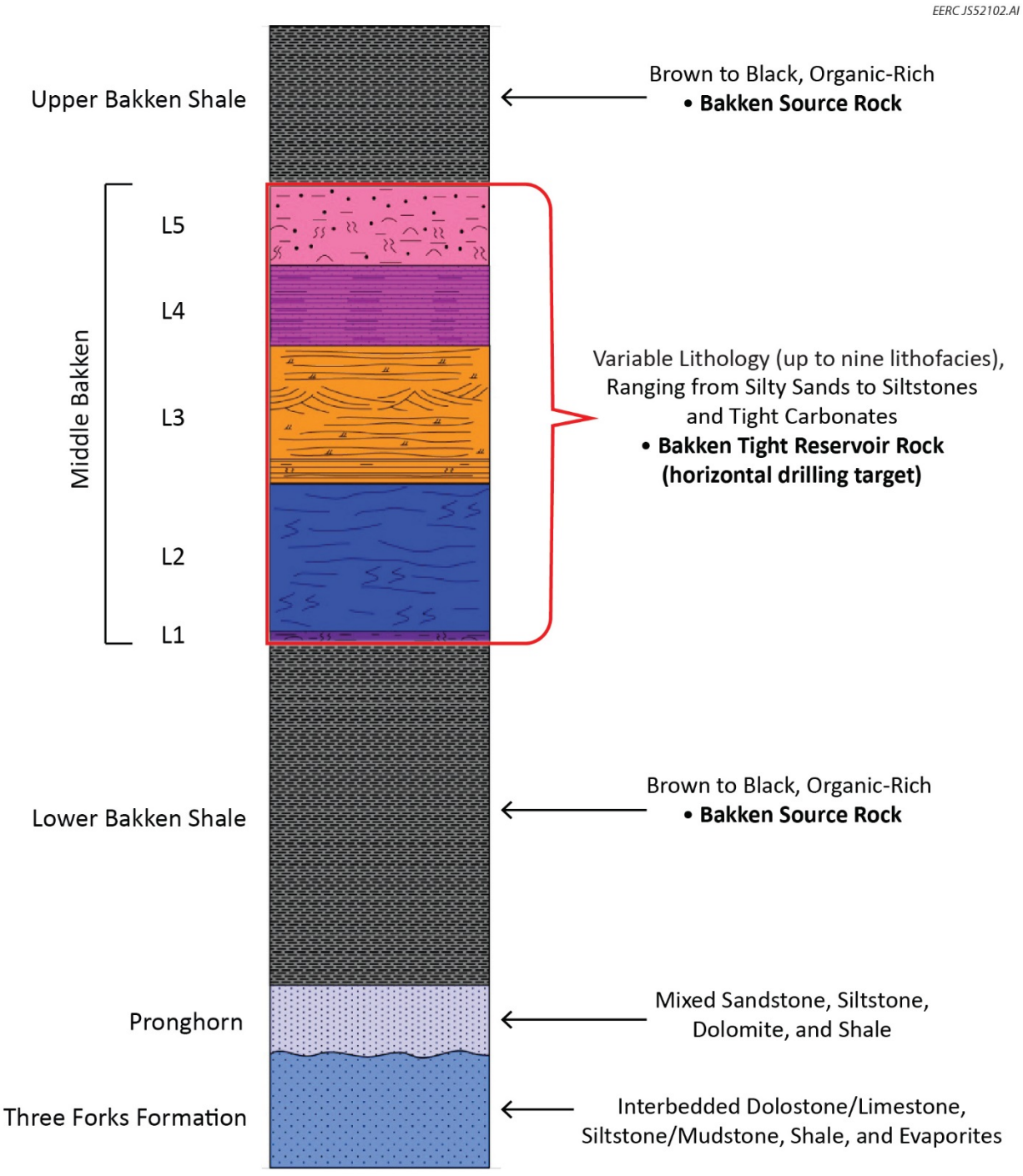

Figure 1. Major oil-producing lithofacies of the Bakken petroleum system. The system also includes the Lodgepole Formation (including the Scallion and False Bakken members) which overlies the Bakken Formation.

CO_2 Storage Resource Equation

Prior to initiating this project, DOE NETL developed a volumetric-based methodology for calculating the prospective CO_2 storage resource of organic-rich shale formations (Goodman and others, 2014; Levine and others, 2016). The DOE NETL formula quantifies the mass of CO_2 stored as either free gas within fractures and pores or as a sorbed component on OM and clays:

$$G_{CO2} = A_t E_A h_g E_h \left[\phi \rho_{CO2res} E_\phi + (1-\phi)\rho_{sCO2} E_m E_{sorb}\right] \quad \text{[Eq. 1]}$$

Where:

G_{CO2}	=	Mass CO_2 storage resource of the organic-rich shale formation, M
A_t	=	Total area of the organic-rich shale formation being assessed for CO_2 storage, L^2
E_A	=	Fraction of formation total area available for CO_2 storage, L^2/L^2
h_g	=	Gross thickness of organic-rich shale formation being assessed for CO_2 storage, L
E_h	=	Fraction of shale formation gross thickness available for CO_2 storage, L/L
φ	=	Percentage of bulk volume that is void volume (porosity), L^3/L^3
ρ_{CO2res}	=	Density of CO_2 at formation pressure and temperature, M/L^3
ρ_{sCO2}	=	Maximum mass of CO_2 sorbed per unit volume solid rock, e.g., the asymptotic value of an appropriate isotherm, M/L^3
E_φ	=	Fraction of shale porosity within the effective formation volume, Ve, available for CO_2 storage. This is a reservoir-scale efficiency factor that is meant to address the probability that CO_2 will never reach some of the pore space because of transport heterogeneities associated with fracture networks and low matrix permeability, L^3/L^3
E_m	=	Fraction of the shale matrix within the effective formation volume, Ve, available for CO_2 storage. This is a reservoir-scale efficiency factor that is meant to address the probability that CO_2 will never reach some of the shale matrix rock because of transport heterogeneities associated with fracture networks and low matrix permeability, L^3/L^3
E_{sorb}	=	Fraction of ρ_{sCO2} due to reductions in sorptive packing at reservoir pressure and temperature conditions. This is a reservoir-scale efficiency factor that is meant to address the inefficiency of sorptive packing on shale matrix rock because of competitive sorption (sorption/desorption with other species) and nonideality of sorption surfaces (reduction of surface coverage) in the shale matrix, L^3/L^3

The green-highlighted text in Equation 1 ($A_t E_A h_g E_h$) calculates the effective formation volume, V_e, of the formation being assessed for CO_2 storage (i.e., area × height after eliminating acreage due to social or physical restrictions and formation-scale characteristics that change as a function of depth). The blue-highlighted text in Equation 1 ($\phi \rho_{CO2res} E_\phi$) calculates the portion of the effective formation volume associated with the mass of CO_2 stored as free gas within fractures and pores. Lastly, the red-highlighted text in Equation 1 ($(1-\phi)\rho_{sCO2} E_m E_{sorb}$) calculates the solid portion of the effective formation volume and the mass of CO_2 stored as a sorbed component on OM and clays.

Work conducted by the EERC through the DOE-funded Bakken CO_2 Storage and Enhanced Recovery Program (Phase II, 2018) resulted in a modified version of this equation. The EERC study also included isotherm data collected under reservoir pressure and temperature conditions (approximately 110°C [230°F] and 400 bar [5800 psi]) (Sorensen and others, 2018). These laboratory measurements provide results in units of mass of CO_2/mass of OM (as defined by total organic carbon [TOC] content) and clay in the rock sample; therefore, ρ_{sCO2} is not necessary, and Equation 1 becomes Equation 2:

$$G_{CO2} = A_t E_A h_g E_h \left[\phi \rho_{CO2res} E_\phi + \rho_{bulk} F_{OM+clay} C_S E_S\right] \quad \text{[Eq. 2]}$$

Where:

ρ_{bulk} = Bulk density of the formation, kg rock/m^3 rock

$F_{TOC+clay}$ = Mass of OM and clay in the rock sample, kg (OM + clay)/kg rock

C_S = Mass of CO_2 sorbed per mass of (OM + clay) in the rock at reservoir pressure and temperature conditions, kg CO_2/kg (OM + clay)

E_S = Combined efficiency of the volume of matrix rock contacted by gas (E_m), i.e., reductions due to transport processes and the efficiency of sorptive packing of gas at reservoir conditions (E_{sorb})

In the aforementioned EERC effort, Equation 2 was used to estimate the prospective CO_2 storage resource of the Bakken. Advanced core characterization of Bakken rock samples revealed that the UBS and LBS comprise a mix of clays and OM, consisting of kerogen and bitumen, whereas the MB member contains little to OM. Thus, CO_2 sorption in the shales could occur on or within both OM and clays, while in the MB sorption occurs largely on or within clay minerals (Sorensen and others, 2017). This prior study conducted by the EERC did not distinguish CO_2 sorption among different types of OM matter or between OM and clays and simply relates C_S as a function of the total OM and clay content of the rock matrix. This was due to the lack of data regarding the CO_2 sorptive capacity of each individual component (OM vs. clay minerals) at reservoir conditions, as well as the difficulty in determining the proportion of OM or clay components that would be in contact with CO_2 in the reservoir.

A key objective of this effort was to use advanced image analysis to better understand and quantify the various minerals, OM, and/or pore and fracture networks that could serve as CO_2 storage sites within fine-grained rocks such as organic-rich shales or other unconventional reservoirs. Improved identification and quantification of these relationships were used to expand the CO_2 storage resource potential equation and build upon prior work conducted by NETL and the EERC. The primary emphasis of the image analysis-based work was to expand the red-highlighted text in Equation 1 ($(1-\phi)\rho_{sCO2} E_m E_{sorb}$), which estimates the solid portion of the effective formation volume and the mass of CO_2 stored as a sorbed component on OM and clays. While image analysis techniques were successfully developed to better identify and quantify the void space in OM and to differentiate between void space in pores versus fractures, additional work is needed in that area to determine connected versus nonconnected porosity before it can be incorporated into the revised storage resource equation. In addition, the modified storage resource equation developed by the EERC expanded the porosity term to account for reservoir fluid displacement efficiency; however, the methods developed through this effort were not

focused on calculating those parameters. Additional work is needed to better understand reservoir fluid displacement efficiencies in organic-rich shales and other tight formations.

The proposed modified storage resource equation for organic-rich shale formations developed through this effort is as follows:

$$G_{CO_2} = V_e\left[\rho_{CO_2}\phi_{PF}E_{\phi} + M_{OMCO2}F_{OM}E_{OM} + M_{ClaysCO2}F_{Clays}E_{Clays} + Others\right] \quad \text{[Eq. 3]}$$

Where:

G_{CO_2}	=	CO_2 mass storage resource
V_e	=	Effective reservoir volume available for CO_2 storage
ρ_{CO_2}	=	Density of CO_2 at reservoir temperature and pressure
ϕ_{PF}	=	Total free-phase void volume fraction due to pores and fractures
E_{ϕ}	=	Efficiency factor associated with free-phase storage
F_{OM}	=	Fraction of solid OM within the effective reservoir volume
M_{OMCO_2}	=	Maximum mass of CO_2 adsorbed per unit volume of solid OM
E_{OM}	=	Efficiency factor associated with adsorption of CO_2 on OM surfaces
F_{Clays}	=	Fraction of clays within the effective reservoir volume
$M_{ClaysCO_2}$	=	Maximum mass of CO_2 adsorbed per unit volume of clays
E_{Clays}	=	Efficiency factor associated with adsorption of CO_2 on clay surfaces
$Others$	=	Contribution from other potential CO_2 uptake mechanisms

Equation 3 incorporates image analysis-based measurements of the fraction of OM (F_{OM}) and fraction of clays (F_{Clays}), which improves estimates of the adsorbed CO_2 storage in shale for each of these fractions. The individual component fractions for OM and clays were determined from using advanced image analysis, as described in the following sections of this report. The efficiency factor associated with free-phase storage, E_{ϕ}, was redefined to include two terms: $E_{\phi eff}$, which is the ratio of connected-to-total void volume, and E_D, which is the reservoir fluid displacement efficiency. The displacement efficiency term accounts for the fact that existing fluids in the void spaces in the reservoir have to be displaced during CO_2 injection to create the net void space that can store CO_2. E_D is further divided into a volumetric displacement efficiency (E_{vol}) and microscopic displacement efficiency (E_d). Volumetric displacement efficiency describes the fraction of void volume contacted by injected CO_2 as a result of the density difference between the CO_2 and the formation fluids which results in a buoyancy effect. Microscopic displacement efficiency represents the actual fraction of void spaces available for CO_2 storage excluding any irreducible oil and/or water saturation. Depending on the geology of the reservoir, this CO_2 buoyancy effect can significantly limit contact of CO_2 with the lower portions of the injection target, although this effect is likely less pronounced in shales than in sandstone reservoirs because of the much lower vertical permeability versus horizontal permeability in shales.

As shown in Equation 3, the term involving solid-phase adsorption of CO_2 has been split and considered as additive terms because of individual adsorptive components in the solid rock, with efficiency factors associated with each component. The maximum mass of CO_2 adsorbed by each component will have to be determined from CO_2 adsorption testing, where “pure”

component samples are isolated from the rock matrix and used to perform the adsorption experiment. The component fractions and efficiency factors associated with CO_2 adsorption on OM and surfaces of clay particles were determined using an advanced image analysis approach described herein.

METHODS

Sample Collection

The samples used in this study were selected from three different locations in the Bakken Formation with varying levels of thermal maturity within the oil window to see if there were differences in OM porosity. The sample selection process involved consulting available literature data on thermal maturity for the Bakken Formation. Specifically, vitrinite reflectance contour maps (Webster, 1984) and T_{max} maps (LeFever, 2008) were combined into a composite index map in Figure 2 that shows thermal maturity levels across prolific areas of the Bakken. Based on the map in Figure 2, Wells 18829 (A), 16974 (B), and 22388 (C) were selected for the study to represent immature, marginally mature, and mature locations (with respect to the oil window), respectively. The cores that were sampled had been stored at the North Dakota Geological Survey (NDGS) core library, with no special preservation other than maintaining normal room temperature conditions in well-secured boxes. Three key lithofacies were selected from each well for this study, including the UBS, the MB, and the LBS. The Upper and Lower shales are representative of typical organic-rich shales found in many Basins in North America and around the world, and the MB sample is a good example of a clastic, siltstone tight oil reservoir rock with relatively low porosity and low permeability. Figure 3 shows the geographic locations of the sampled wells in the North Dakota portion of the Bakken Formation. Well 18829 is located in Burke County, close to Saskatchewan, Canada, while Wells 16974 and Well 22388 are located in Dunn County and McKenzie County, respectively, which are in the northwestern corner of North Dakota.

Analytical Methods

The routine analytical techniques employed in this project included FESEM coupled with energy-dispersive x-ray spectroscopy (EDS), x-ray diffraction (XRD), x-ray fluorescence (XRF) spectroscopy and optical microscopy, and ultraviolet fluorescence microscopy of thin sections. Prior to FESEM analysis, polishing of the samples was achieved using a broad ion beam milling system. Nonroutine analytical methods were also employed, including nuclear magnetic resonance (NMR) and isothermal sorption testing. These techniques are listed in Table 1. A detailed description of the analytical techniques are included in Appendix A.

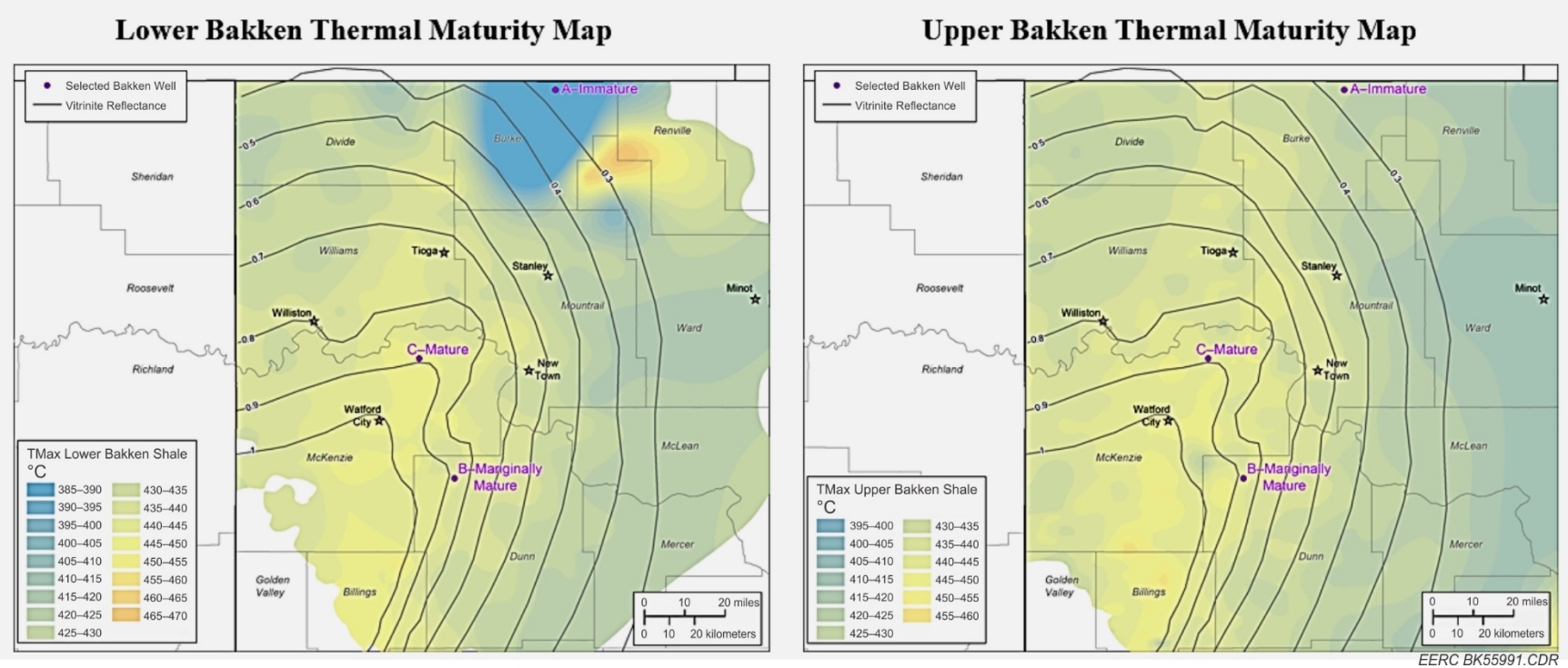

Figure 2. Lower and Upper Bakken thermal maturity index maps to show the maturity level of the selected wells. Vitrinite reflectance (VR_o) measurements are adapted from Webster (1984), and T_{max} values are from LeFever (2008) NDGS, Geologic Investigation No. 63.

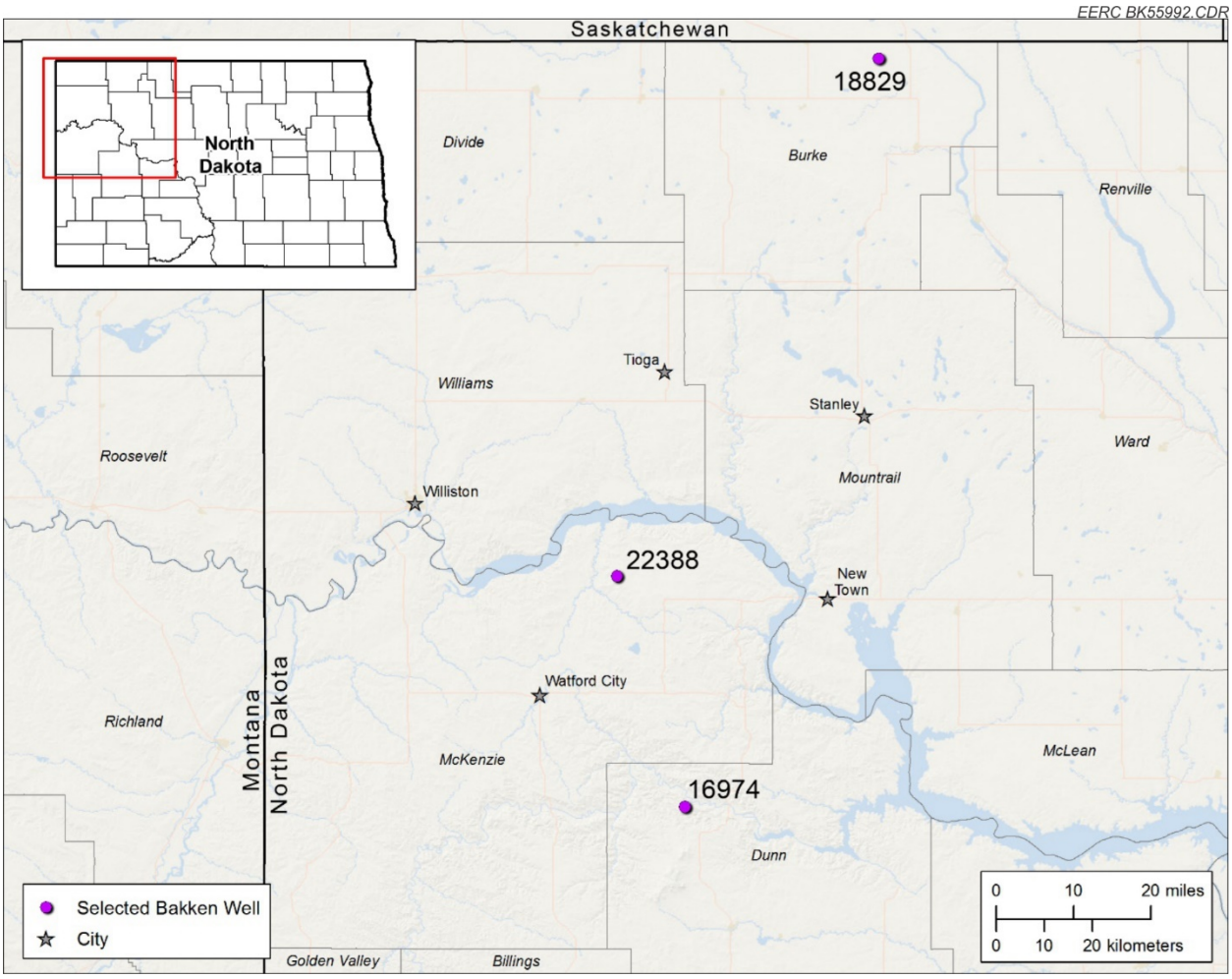

Figure 3. Section of North Dakota map with locations of wells selected for this study.

Table 1. Summary of Routine Analytical Methods

Analysis Type	Information Derived
FESEM	General sample morphology, elemental distribution, and inferred mineralogy
XRD	Bulk mineralogy
XRF	Bulk chemistry
Optical Petrographics	Mineral phases, grains, pores, depositional environment
NMR	Pore-size analysis and fluids detection.
Sorption Testing	CO_2 sorption capacity

Image Analysis Techniques

Advanced Mineral Identification and Characterization System (AMICS)

The AMICS system is a software solution for automated mineral analysis, specifically developed for the identification and characterization of minerals in ores and other types of materials (Bruker, 2019). The target applications include analysis of geological, metallurgical, mining, and oil and gas industries. AMICS is integrated with Hitachi SEM and the accompanying EDS detector for seamless automated image and x-ray acquisition and subsequent classification and quantification of the mineral phases in the sample. AMICS has three key technical components, including automated mineral identification and classification, proprietary computerized mineral grain boundary/phase segmentation, and comprehensive library database management and spectral deconvolution. The reporting tools include mineral maps showing grains and their associations, quantitative mineralogy based on stereological 2-D area approximations (Gundersen and Jensen, 1987; Howard and Reed, 1998; Weibel, 1979), grain size and distributions, and other graph and chart export options.

In this project, specific emphasis was placed on developing AMICS approaches that enhance the characterization of unconventional organic-rich shales of the Bakken Formation, but which can also be applied more generally to other tight oil and/or gas reservoirs. To perform an AMICS analysis, the samples were prepared by polishing using an ion mill system and then coated with carbon to avoid static charging effects when analyzed under high-vacuum conditions in the FESEM. The AMICS workflow that automatically acquired and analyzed several image frames from the sample was set up using the AMICS graphical user interface (GUI). The mineral classifications detected and quantified automatically were further refined to account for any new mineral phases that may not be in the library database to obtain a final product. A more detailed description of the AMICS software and application to this effort is provided in Appendix A.

Additional Advanced Image Analysis and Classification Techniques

The images acquired by FESEM were processed using an advanced image analysis approach that included a combination of Ilastik (Sommer and others, 2011), Image-J (Rasband and others, 2016), and Fiji (Schindelin and others, 2012). Ilastik was used for advanced segmentation, and Image-J and Fiji were used for further processing of the segmented images to obtain feature particle statistics. Whereas the AMICS image analysis software is designed primarily for mineralogical characterization based on gray-scale imagery and x-ray data, Ilastik has built-in advanced capabilities for efficient segmentation of image features based on attributes such as texture, shape, and gray scale. Hence, high resolution, crisp images with high feature contrast are critical for optimal and efficient segmentation. To improve the spatial resolution of different pore/feature scales in the tight rock matrix and within the OM particles, two sets of images were acquired. The first set of images was obtained at a magnification of about 3000× (LowMag), and a second set was obtained at about 20,000× (HighMag). Both sets of images were acquired in backscatter electron (BSE) and secondary electron (SE) modes to facilitate distinction of different surface topological and textural attributes of features such as pores, clays, OM, and fractures within the matrix and within OM particles. The LowMag images were used to segment and quantify the total contents of pores, OM, clays, medium-density minerals (MDmin),

and high-density minerals (HDmin), while the HighMag images were used primarily to segment and quantify the porosity associated with OM (PAOM). The LowMag images were acquired in a random manner to increase the chances of collecting a set of images that is the best representation of the sample matrix, while the HighMag images were specifically acquired on OM particles that were found within the sample matrix. For clarification, MDmin refers to major mineral types such as quartz, calcite, dolomite, K-feldspar, etc., that do not have high atomic number elements, while HDmin includes primarily pyrite and occasionally zircon or monazite; i.e., minerals that contain high atomic number elements. Figure 4 is a display of typical segmented images together with the corresponding gray scale images for comparison.

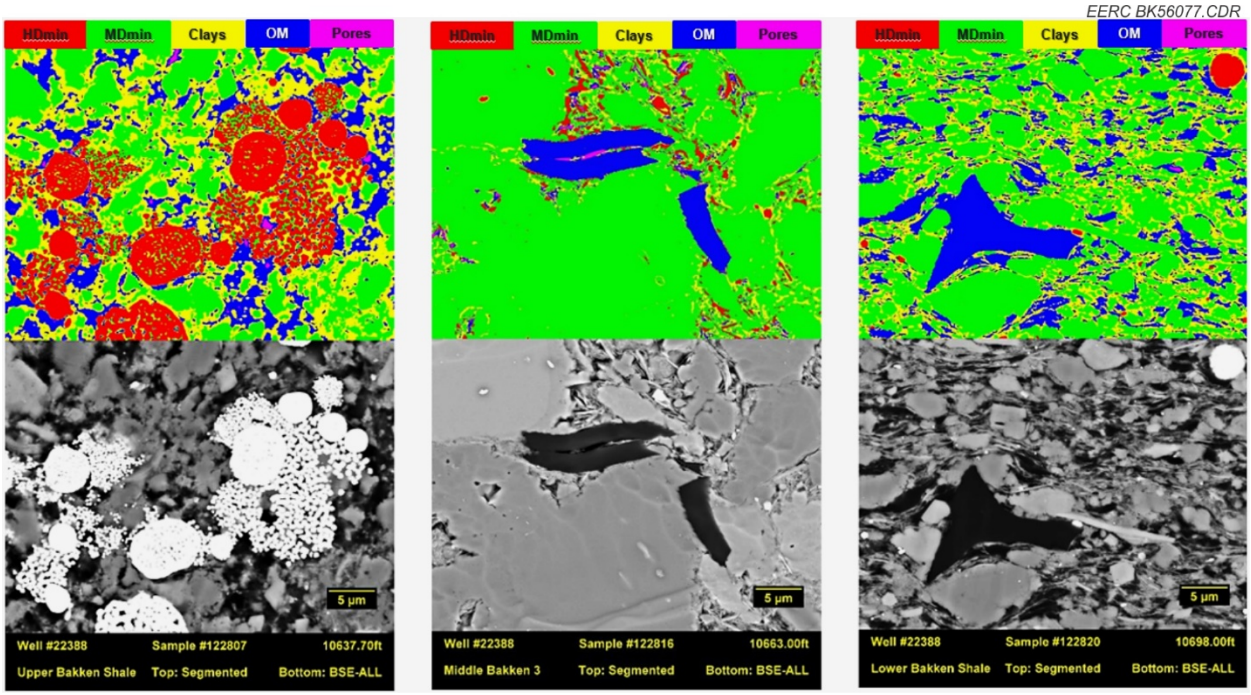

Figure 4. Illustration of finalized Ilastik segmentation images and the corresponding gray-scale versions for UBS (left), MB3 (middle), and LBS (right) samples.

Image Segmentation Workflow

A workflow developed for segmenting the FESEM images into different classes based on features of interest is shown in Figure 5. As part of the segmentation process, Ilastik uses complex information about the image such as texture, shape, and gray scale. In addition, mathematical algorithms using functions such as Gaussian blur and probabilistic approaches are used to obtain class probability images that are then merged to derive a final version of the segmented image. Algorithms such as those utilized by Ilastik that include classification down to the pixel-level detail are very useful for shale characterization because of the fine-grained nature of the material.

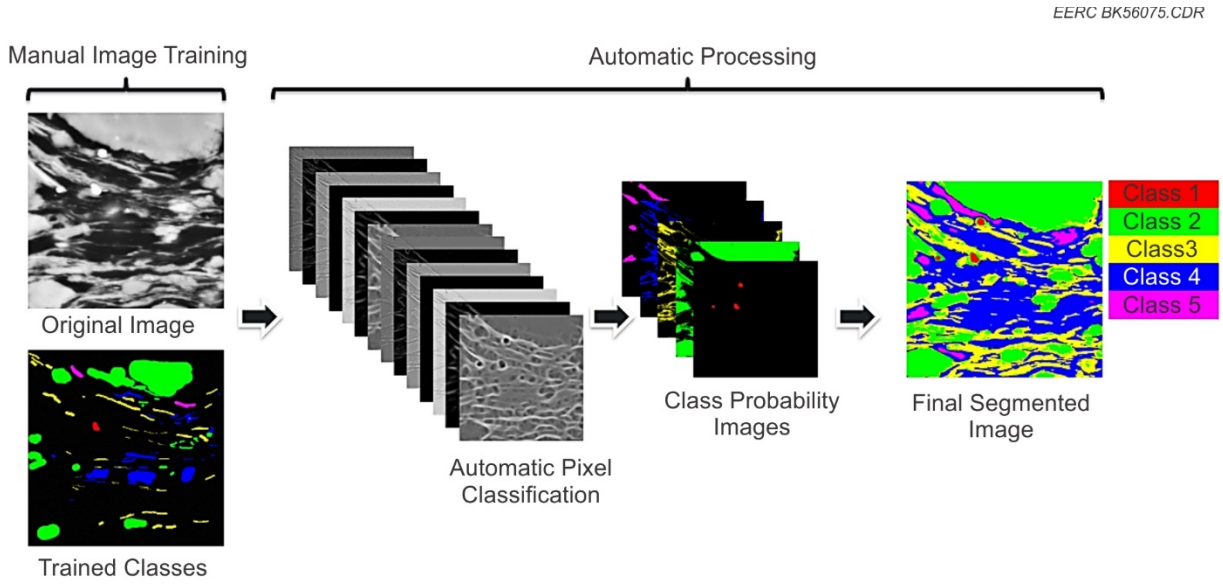

Figure 5. Workflow of Ilastik segmentation for shale and tight rock characterization.

Flow-Through Test Procedure

Flow-through tests were performed to evaluate the permeation rates of CO_2 into Bakken Formation samples and to estimate the retention of CO_2 within the bulk samples. Each test was conducted using a temperature-controlled high pressure test apparatus. Prior to testing, the plug was weighed and loaded into a CO_2-resistant sleeve consisting of an inner layer of Teflon, middle layer of lead, and outer layer of Teflon. This inner sample assembly was inserted into a thick rubber gasket to distribute the confining pressure load evenly across the sample. The assembly was then loaded into a high-pressure (10,000 psi) Hassler-style core holder and placed into a temperature-stable convection oven (Figure 6).

Figure 6. Inner gasket assembly and Hassler-style core holder.

With the core holder in place, the injection and receiver side of the system were plumbed to computer-controlled syringe-style pumps capable of running in constant pressure and flow rate modes. Because of the low flow rates and total volume anticipated for these low permeability samples, the system tubing was minimized to aid in the final quantification of injected and received CO_2. After plumbing, the oven was adjusted to near reservoir temperature of 160°F and monitored during a series of long-duration leak checks to ensure that a baseline systematic leak rate was obtained prior to permitting flow through the core. Figure 7 show the experimental set up of the flow-through system.

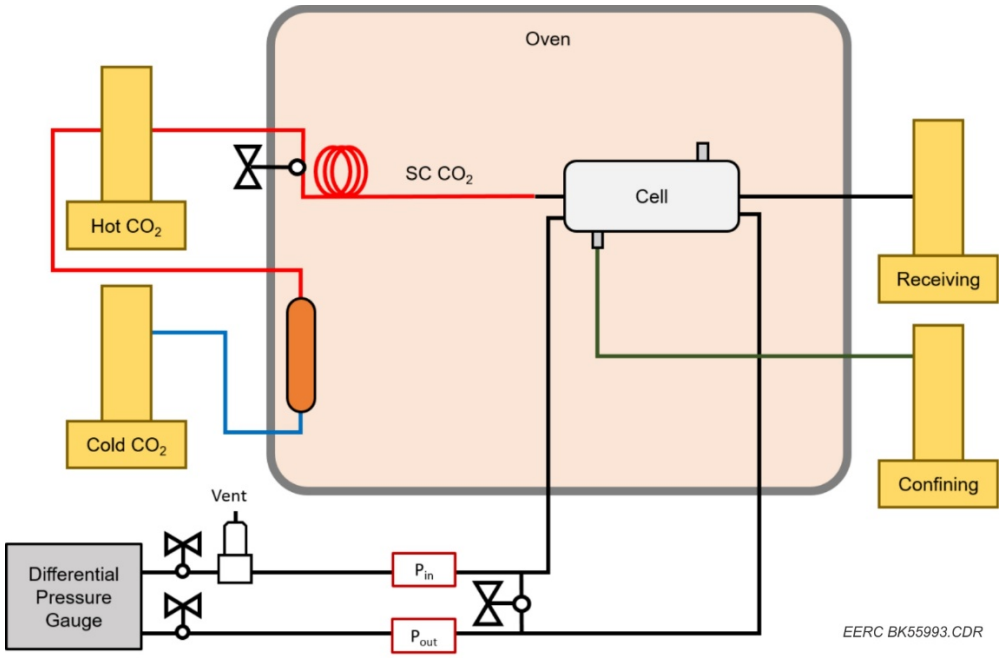

Figure 7. Schematic diagram illustrating the flow-through system as it was configured for low-flow testing.

At the onset of testing, the confining pressure within the annular space of the core holder (between the gasket and steel body) was adjusted to 7500 psi to ensure CO_2 slippage between the core sample and gasket was not occurring. Both the injection and receiver pumps were set to 4600 psi and allowed to stabilize. The system was monitored for a brief period to ensure that the system leakage is minimal and stable. The injection pressure was increased to 5000-psi pressure while the outlet side was maintained at 4600 psi, resulting in a 400-psi differential pressure. Throughout the test, the differential pressure was not changed. Data collected during testing included injection and receiver pump volume, flow rates, and pressures. Because the pump transducers are prone to drifting, the system pressure was monitored at the core inlet and outlet faces using high-accuracy pressure/temperature transducers. Data generated throughout the testing period were collected at a predetermined interval using a data acquisition system communicating with all pumps, regulators, transducers, and temperature probes on the instrument. Each test was conducted for a period of time that sufficiently captured the stable flow through each sample, and data were collected on a continuous basis over the same time frame.

Micro-CT Experiments at NETL's CT Scanning Laboratory in Morgantown

NETL's flow-through system, coupled with CT imaging capabilities, was used to investigate potential changes in sample permeability (transmissivity) and/or fracture and pore networks during dynamic CO_2 exposure tests. To complement those experiments, the EERC conducted FESEM analysis of the samples pre- and post-CO_2 exposure to determine whether any geochemical changes occurred to the minerals in the samples. Samples sent to NETL included two UBS samples from a mature location and one LBS sample from a marginally mature location.

For each test, the core was initially scanned using a NorthStar Imaging Inc. M5000 industrial CT scanner. The sample was then loaded into Buna-N nitrile rubber confining sleeve and a Hassler-style core holder. A confining pressure was applied with deionized water, and pore pressure was increased with gaseous CO_2. The temperature was set to the test condition value of 160°F (although the raw data from the test suggest that this temperature may not have been maintained in the system), and the pressure was increased to reach the final testing pressure state. The inlet pore pressure was maintained at 1600 psi, and the receiver pump pressure was kept at 1200 psi, thus maintaining a differential pressure (dP) of 400 psi across the core. The confining pressure was kept at 2000 psi. Flow rates, pressures, and volumes were recorded for the duration of the test. In order to conserve CO_2, a bypass valve was used to empty CO_2 from the receiving pump back to the injection pumps. For the entire duration of the test, the bypass was used twice, which resulted in minor pressure fluctuations; the data points corresponding to the fluctuations were removed prior to processing the final data set.

NMR Testing Methods

An Oxford Instruments Geospec2 NMR system (Oxford Instruments, 2017), coupled with GIT software, LithoMetrix™ (GIT, 2017), was used for all scans reported herein. Prior to any scan, the NMR instrument was calibrated according to procedures provided by Oxford Instruments and GIT. NMR is a special core analysis technique that can be used to determine several petrophysical properties of geologic core samples, including porosity, permeability, capillary pressure, and wettability/imbibition characteristics. In this study, the focus was to derive porosity data from core samples using NMR T2 relaxation profiles. Furthermore, T1–T2 maps were used to determine fluid mobility within core samples before and after CO_2 flow-through experiments. Additional details about NMR analysis are provided in Appendix A.

Sorption Test Procedures

Two types of tests were performed to determine the sorptive properties of the organic-rich shales of the Bakken. One type of test included high-pressure, high-temperature adsorption and desorption testing using a Rubotherm magnetic suspension balance. The other type of sorption isotherms were generated at Core Laboratories using a more conventional Langmuir-type experiment. Each test procedure is described in more detail in Appendix A.

Because these tests were performed on ground samples of rock, they are thought to represent the maximum sorptive capacity of the rocks. In addition, because it is difficult to

differentiate between adsorption and absorption in these tests, the general term of “sorption” is used throughout this document and is intended to include both potential mechanisms.

RESULTS

Sample Mineralogy

To better understand the key mineral phases within the Bakken samples evaluated for this effort and to support the FESEM mineralogical characterization, several samples from the UBS, MB, and LBS were analyzed for quantitative bulk mineralogy using traditional powder pack samples, as well as analysis of isolated clay fractions to determine the different clay species and amount of each. The results, presented in Figures 8 and 9, show that the shales are dominated by fine-grained quartz and clays, with smaller amounts of K-feldspar, dolomite, and pyrite. There is very little calcite in the shales. Although pyrite occurs in relatively smaller quantiles, it is almost ubiquitous in Bakken shale, where it often occurs as pyrite framboids and occasionally as regular and irregularly shaped precipitates. The Upper shale member also appears to have a comparatively smaller clay content than the Lower member, with the immature core having the most clay mineral content.

Results of isolated clay fraction analysis presented in Figure 8 show that there are two main clay species in Bakken shales and the middle member, including illite and chlorite. The amount of illite in the shales is higher than in the middle member, while the chlorite content is somewhat similar in the shales as in the middle member. The UBS clay fraction results show a rather simple clay matrix with 100% illite at the mature and immature locations, while illite and chlorite were observed at the marginally mature location. The MB3 and LBS samples showed slightly more complicated clay mineralogy with the presence of illite, chlorite, and potentially illite/smectite mixture at all three locations. The impact of clay minerals is significant for CO_2 storage. Although illite, which appears to the dominant clay in Bakken shales, is not a typical swelling clay, it can contain tight pore spaces that can trap CO_2 through geochemical interactions. These interactions facilitate adsorption of CO_2 in the matrix. Hence, the larger the clay content is, the larger the fraction of CO_2 adsorbed, which results in higher CO_2 storage resource potential for the shale. The appearance of small quantities of swelling clays like smectite in the LBS unit could indicate an even higher potential for CO_2 storage, where CO_2 molecules can form intercalated layers in smectite in addition to the adsorbed fraction.

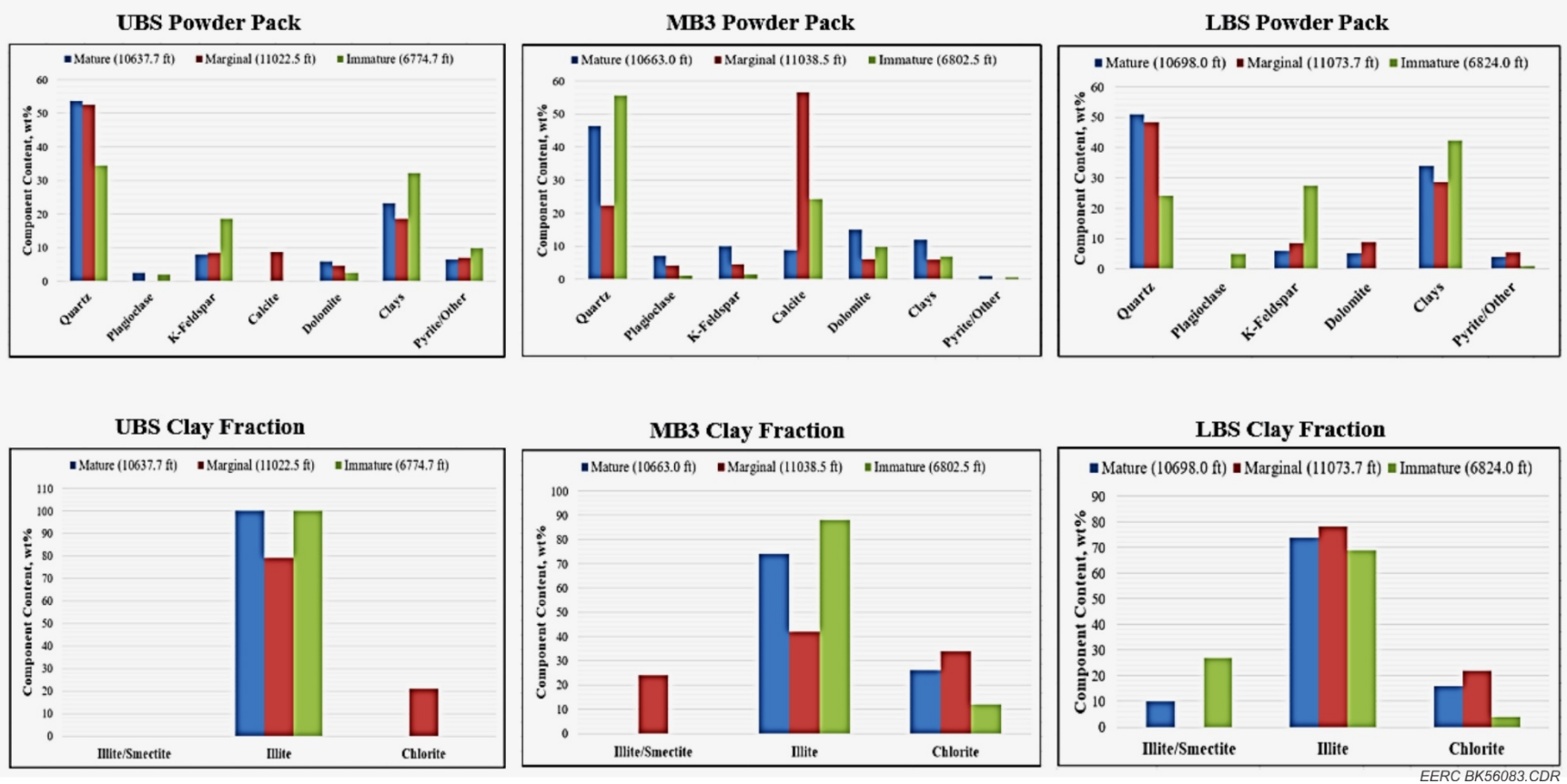

Figure 8. XRD results of traditional powder pack samples and isolated clay fractions.

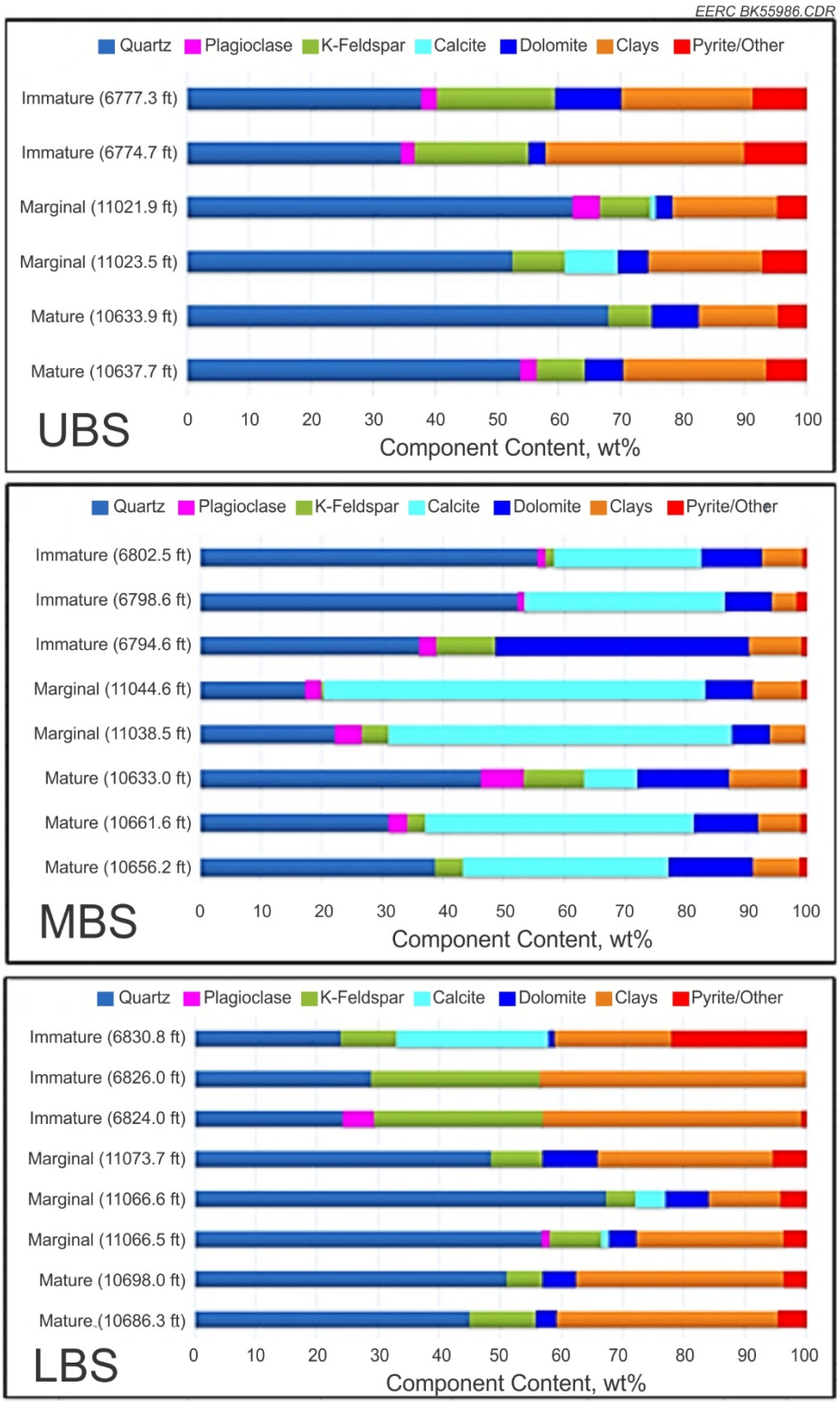

Figure 9. Expanded set of XRD bulk mineral analysis data to illustrate lateral and vertical variability and heterogeneity within Bakken Formation lithofacies.

Morphology, Structure, and Occurrence of OM and Clay Minerals

The main purpose of conducting advanced FESEM mineral characterization was to gain better insights into the detailed morphologies of the sample minerology, OM, pores, and fractures at the micro- to nanoscale that can significantly impact CO_2 storage, but which cannot be easily observed by conventional approaches. Specifically, image analysis techniques were used to detect and quantify these features for the purpose of improving prospective estimates of CO_2 storage in organic-rich shales. The most important phases of interest were clays and OM that have high CO_2 sorptive capacity.

FESEM analysis was conducted to evaluate porous and nonporous types of OM and to determine if advanced image analysis techniques could be developed to quantify OM porosity. Figure 10 shows nanopores within OM with sizes in the range of about 20–50 nm. The porosity determined by using image analysis techniques for the OM particle shown in Image 10B is about 4.5% and that for the OM particle in Image 10C is about 6.5%. It should be noted that these are 2-D area% as a fraction of the total OM particles area and are not relative to the entire frame area. Characterization of OM nanoporosity is critical because of the relevance in the determination of CO_2 transport and sorption mechanisms in organic-rich shales. Figure 10A is a very high magnification (100,000×) image of the pore structure and network within the OM particle. Such detailed imagery provides very useful information about OM pore network structures, shapes, and tortuosity. This type of information can be used to develop first-principle reservoir models for estimating CO_2 flow patterns and/or storage resource potential. In this study, a characterization of porosity within OM was also useful as a first step in deriving an image-based equation for estimating the CO_2 mass storage resource potential for organic-rich shales, which is discussed later in this report.

Figure 11 shows the porous and nonporous OM types observed in Bakken shale samples (Image A), and Images B and C show more details of the texture of porous OM. Image C OM texture is consistent with spongy OM descriptions that have been suggested in the literature (Bousige and others, 2016). Figure 12 illustrates that even nonporous OM in Bakken and Marcellus shale samples can contain void space in the form of microfracture networks, which are important features that could affect CO_2 migration and transport. Figure 12D illustrates that, in some cases, microfractures occur at the OM–mineral interfaces rather than within the OM. Image C within Figure 12 shows an OM particle with bright radioactive (uranium-rich) particles in the middle. The presence of radioactive elements in source rocks is important and has been linked to quickened hydrocarbon maturation (Mao and others, 2014).

The presence of porous OM in shale matrices is important for CO_2 storage as well as CO_2-based enhanced oil recovery (EOR). The porosity provides a pathway for gas migration with the potential for trapping through adsorption or physical trapping because of high capillary pressure. In addition, the mixing of CO_2 with hydrocarbon molecules trapped within the OM can cause swelling, which leads to greater mobilization of the hydrocarbons for improved recovery. In addition, the void space within OM particles also increases the CO_2 storage potential beyond just sorption onto the OM.

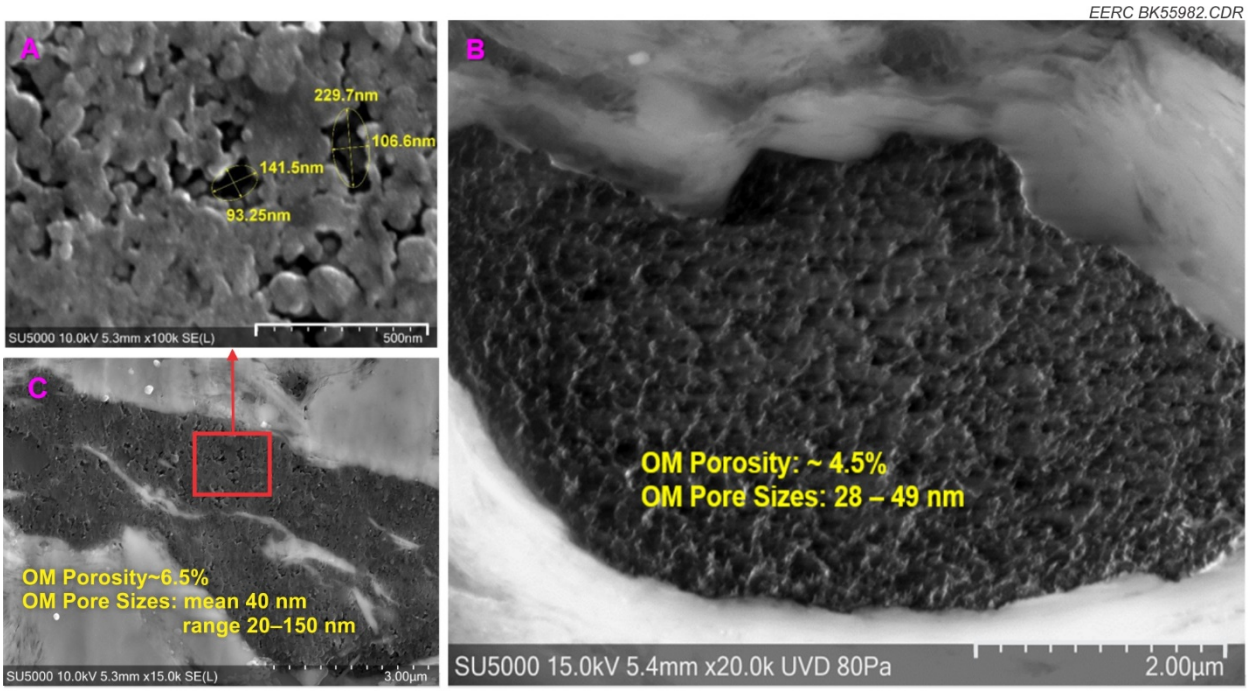

Figure 10. Porosity associated with OM in Bakken shales.

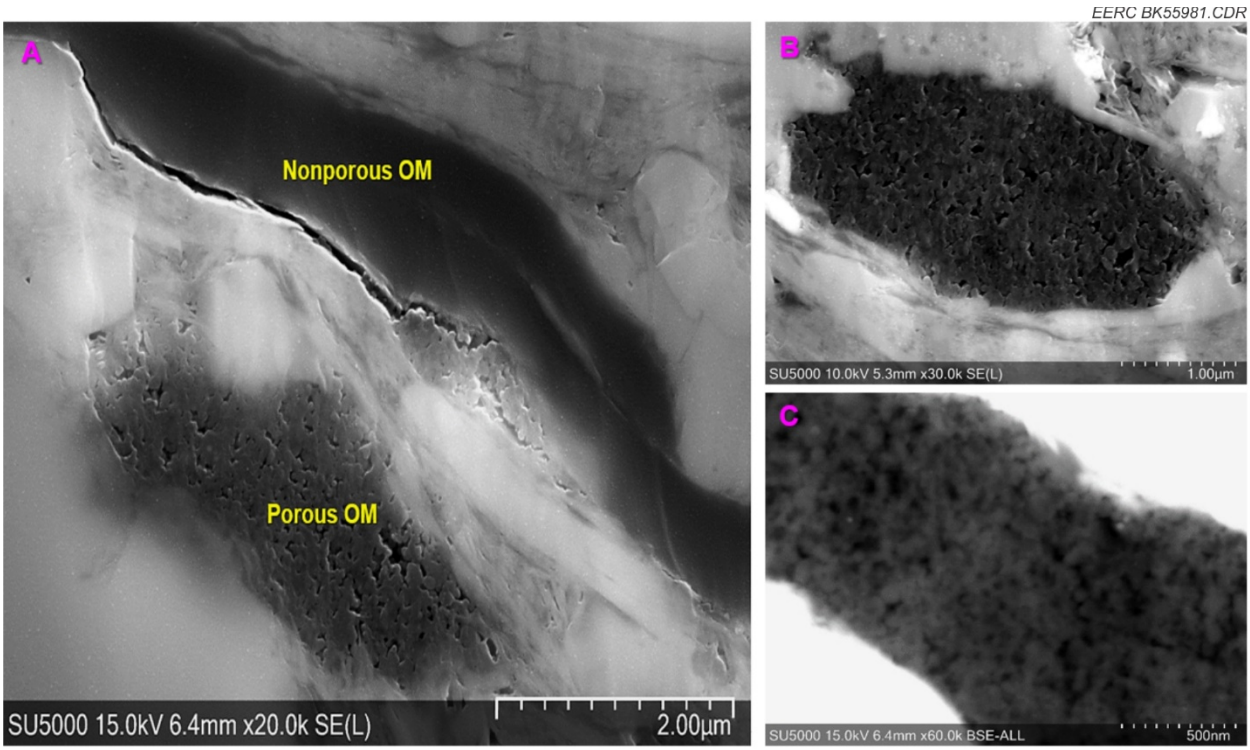

Figure 11. Porous and nonporous OM and their textures.

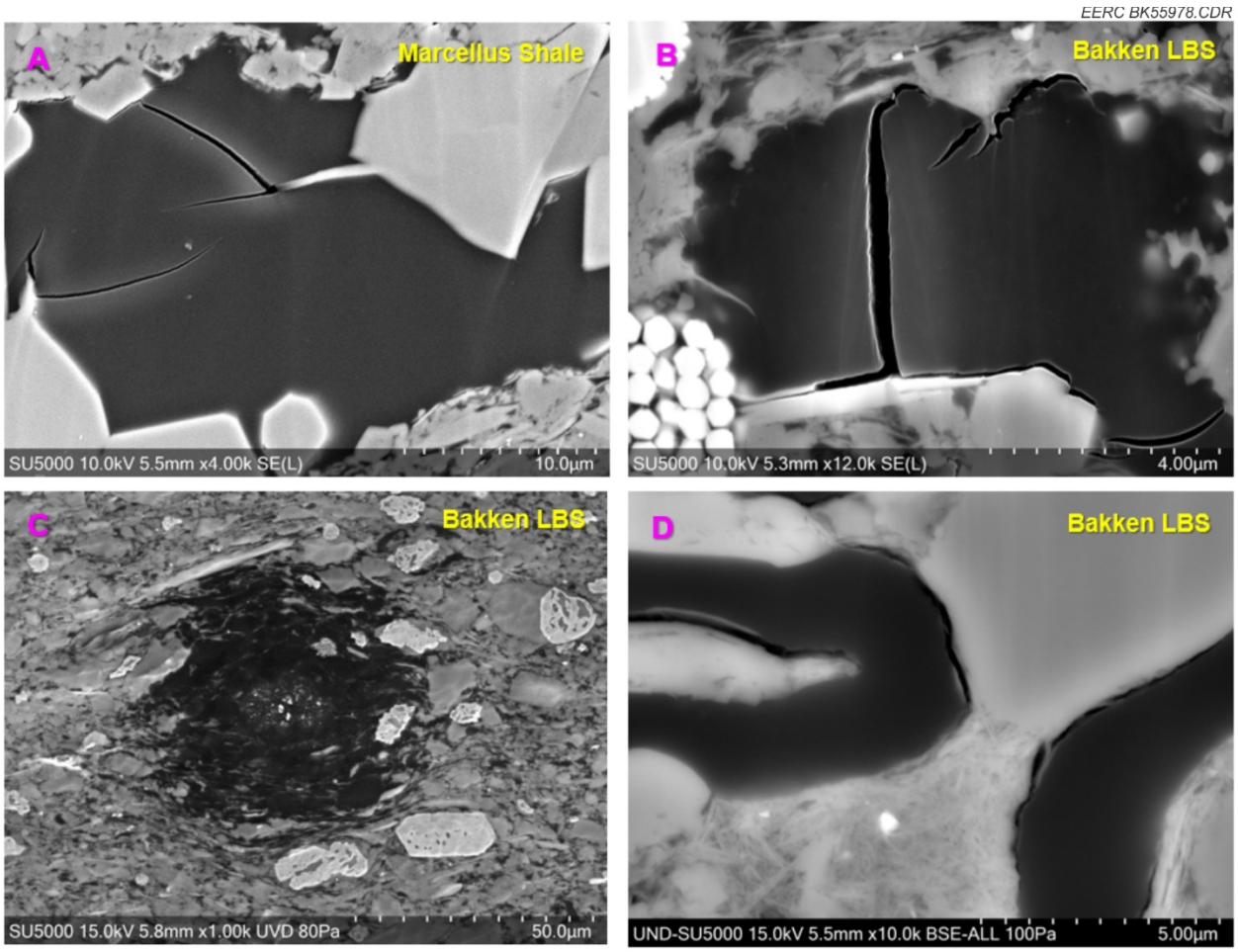

Figure 12. Nonporous OM in Marcellus and Bakken shales. Images A and B show that both Marcellus and Bakken shales have OM that is nonporous but contains microfractures; Image C shows bright radioactive material in the middle of OM, and Image D shows algae-derived OM with fractures occurring at the OM–mineral interfaces.

Detailed clay mineral structures obtained by FESEM for Bakken shale and reservoir (MB) samples are displayed in Figures 13 and 14, respectively. Based on FESEM and XRD analysis, the major types of clay minerals observed in Bakken shale and reservoir rock samples are illite, muscovite, and a minor occurrence of chlorite, with illite being the dominant clay mineral type in the Bakken Formation. All clay types are believed to be authigenic; i.e., they are formed in situ through various diagenetic processes. In most cases observed in this study, clays are the main pore-filling minerals in the shales and MB samples as shown in both Figures 13 and 14. In Figure 14 Image B, it can be seen that authigenic illite and muscovite growth appears to be cutting off intergranular connected porosity to form two pore chambers that are poorly connected. While a clay mineral presence can be detrimental to reservoir quality, it can be instrumental for CO_2 storage. CO_2 molecules are small enough to be able to migrate through the tight pore spaces within clays to potentially become trapped via adsorption. Consequently, tight reservoirs with relatively high clay content can constitute substantial CO_2 storage opportunities.

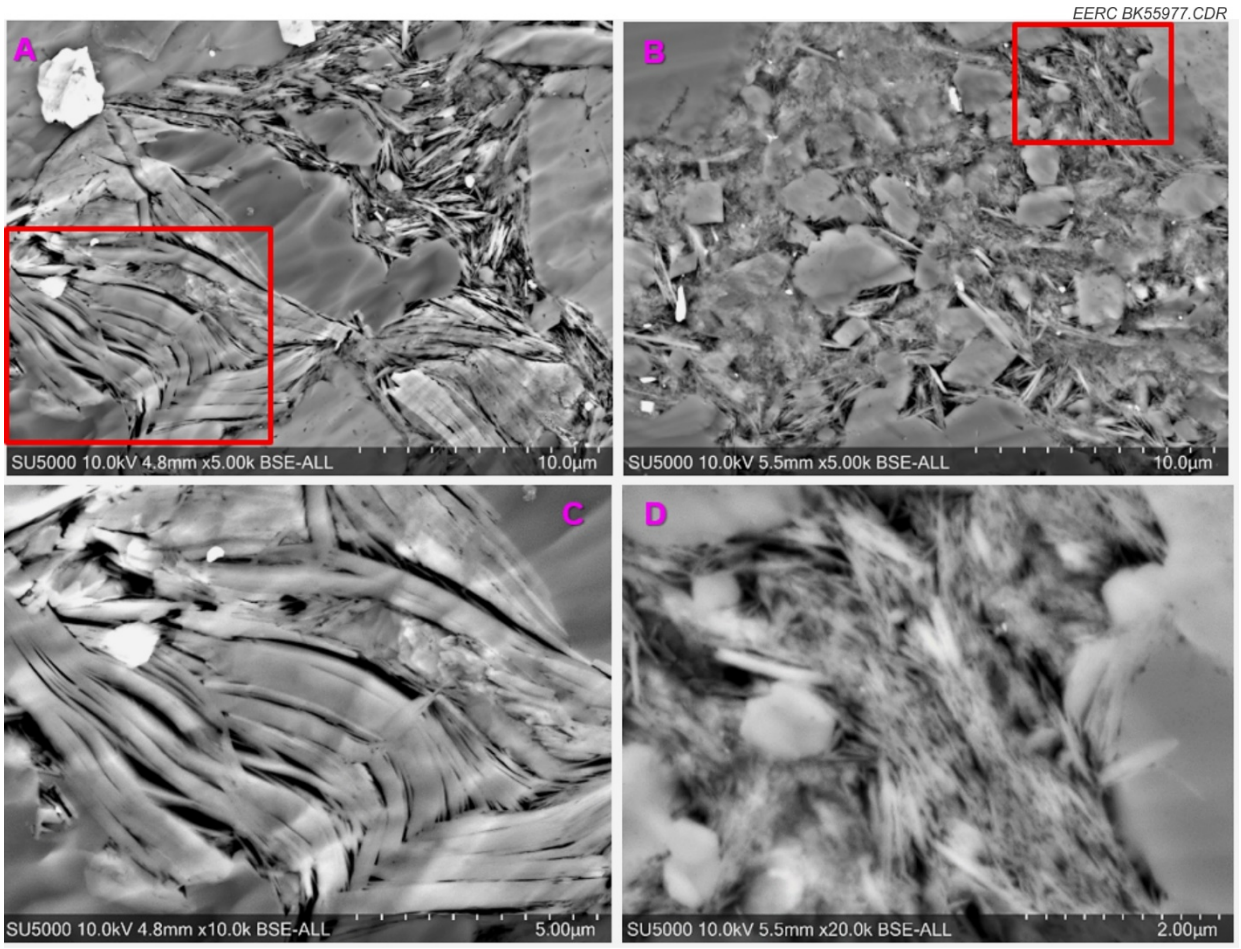

Figure 13. Clay mineral textures in a Bakken reservoir (MB) sample. The red box in Image A is enlarged in Image C, and the red box in Image B is enlarged in Image D.

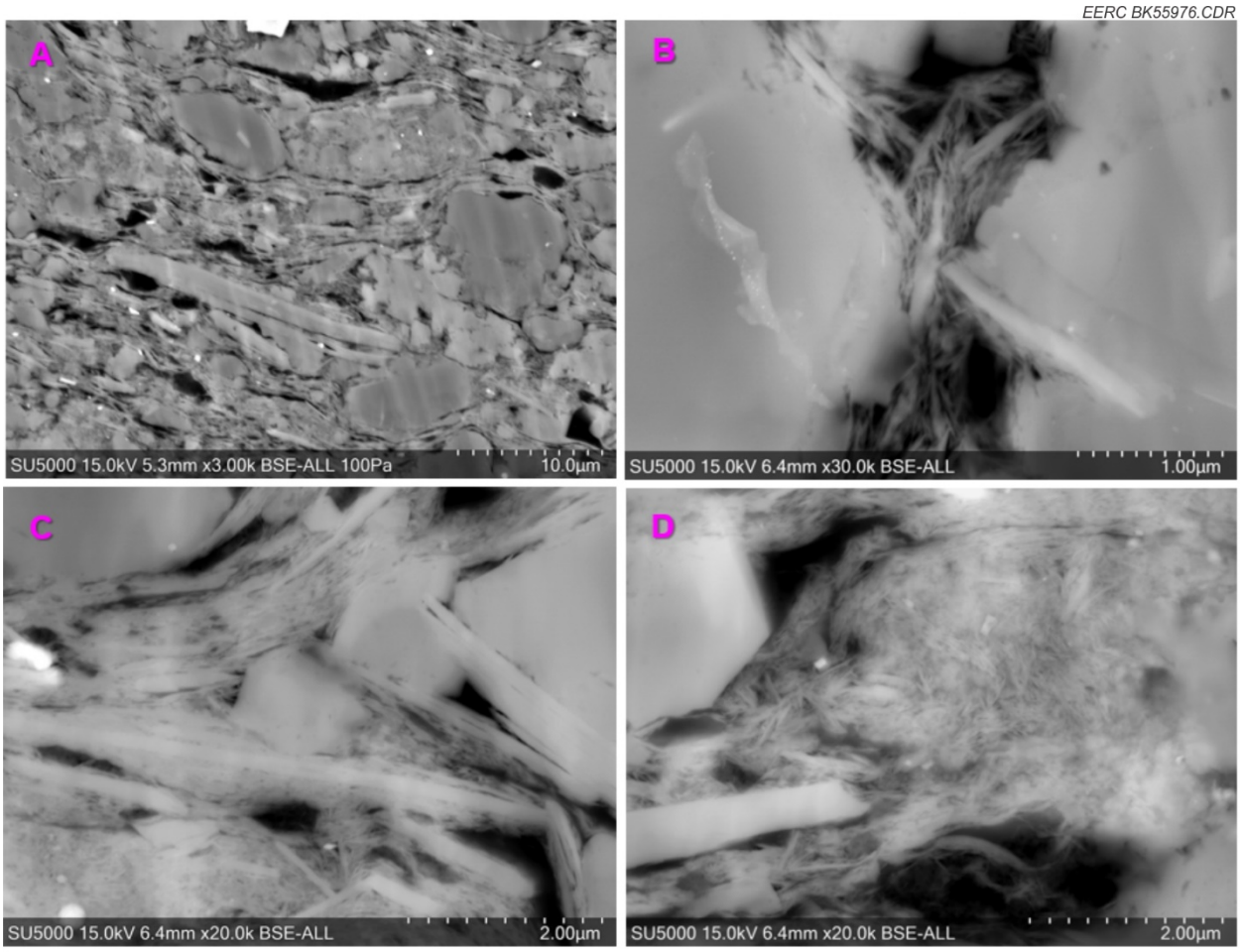

Figure 14. Clay mineral textures in LBS sample. Image A shows a view of the matrix, and Images B, C, and D show various textures of clays. Image B also show intergranular pore space blockage.

Image Analysis Results

AMICS Mineralogy

The mineral composition of the samples determined by AMICS software is presented in Table 2, and the accompanying mineral maps are displayed in Figure 15. Figure 16 summarizes the three broad components of interest, including OM, clays, porosity, with all other phases lumped together as "others." In Figure 17, individual charts of the three key components or interest as well as microcrystalline quartz (chert) are shown to illustrate the variations in sample composition between different lithofacies, well locations, and thermal maturities. Also shown in Table 2 and Figures 16 and 17 are the results obtained from a Marcellus shale sample (M-Shale) for comparison and to demonstrate the applicability of the AMICS-based approach to other shale reservoirs. As previously mentioned, XRF and thin-section analyses were also performed to support the mineralogical identification using AMICS.

Table 2. Mineral Composition Obtained by AMICS Software

	Mature			Marginal			Immature			
	UBS	MB3	LBS	UBS	MB3	LBS	UBS	MB3	LBS	M-Shale
Component	Area%	Area%	Area%	Area%	Area%	Area%	Area%	Area%	Area%	Area%
Quartz	26	43	25	15	30	24	6	43	16	36
Chert	9	0	5	42	2	16	5	0	1	21
K-Feldspar	9	8	7	6	6	7	9	5	20	0
Dolomite	6	13	4	2	8	5	1	9	0	3
Calcite	0	9	0	9	38	0	0	36	0	18
Albite	2	5	2	2	5	1	1	0	2	2
Pyrite	3	1	2	9	1	5	2	0	0	1
Rutile	0	1	0	0	0	0	0	0	0	0
Muscovite	4	8	6	3	5	4	3	1	7	2
Illite	27	10	37	5	2	28	31	3	49	10
Apatite	0	0	0	0	2	0	0	0	0	0
Chlorite	1	0	1	1	0	2	0	0	0	0
Organics	12	0	11	6	0	7	39	0	4	6
Sphalerite	0	0	0	0	0	0	0	0	0	0
Halite	0	0	0	0	0	0	0	0	0	0
Zircon	0	0	0	0	0	0	0	0	0	0
Monazite	0	0	0	0	0	0	0	0	0	0
Chromite	0	0	0	0	0	0	0	0	0	0
Porosity	0	3	1	0	1	0	1	2	0	1
Balance	0	0	1	1	0	0	0	1	0	1

The most important observation from Table 2 is the detailed, most comprehensive prediction of the mineralogical composition of any sample by AMICS, including accessory and trace mineral phases that are otherwise not easily detectable by XRD or other methods. However, it should be noted that these results are semiquantitative and reported as area%. Thus the data cannot be directly compared to XRD wt% quantifications but do provide useful trends for broad or generalized interpretations. If desired, the volume of each phase could be obtained by applying a stereological approximation (Gundersen and Jensen, 1987; Howard and Reed, 1998; Weibel, 1979), where 2-D areas are summed over a large number of sample sections and used to estimate the mineral volume. This information could be combined with individual mineral density to determine approximate wt%. Even in such cases, the AMICS-derived mineral wt% is not expected to directly match the XRD wt%, but the trends should be similar assuming representative and enough 2-D areas are sampled during AMICS processing.

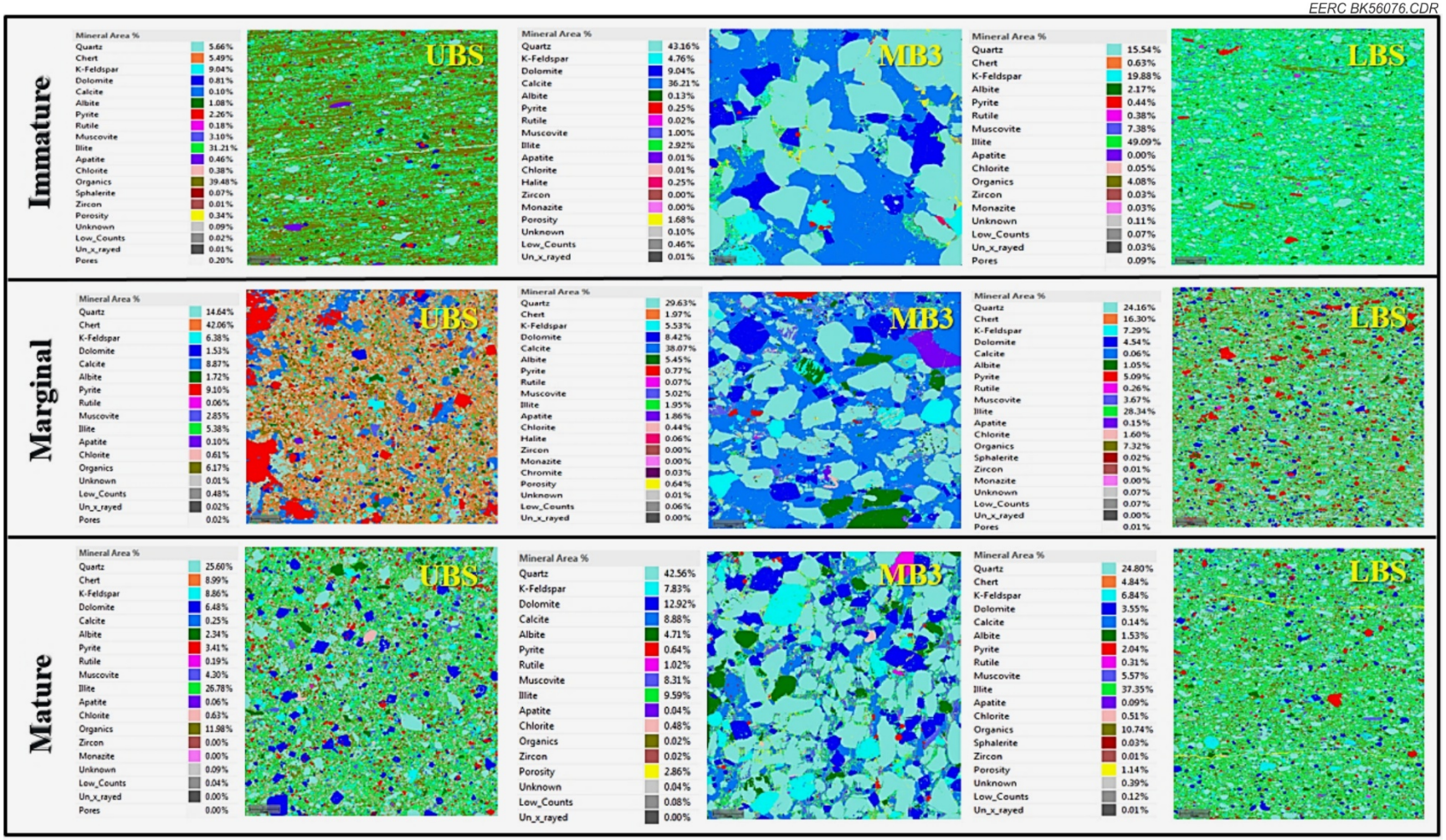

Figure 15. Mineral composition maps generated by AMICS software.

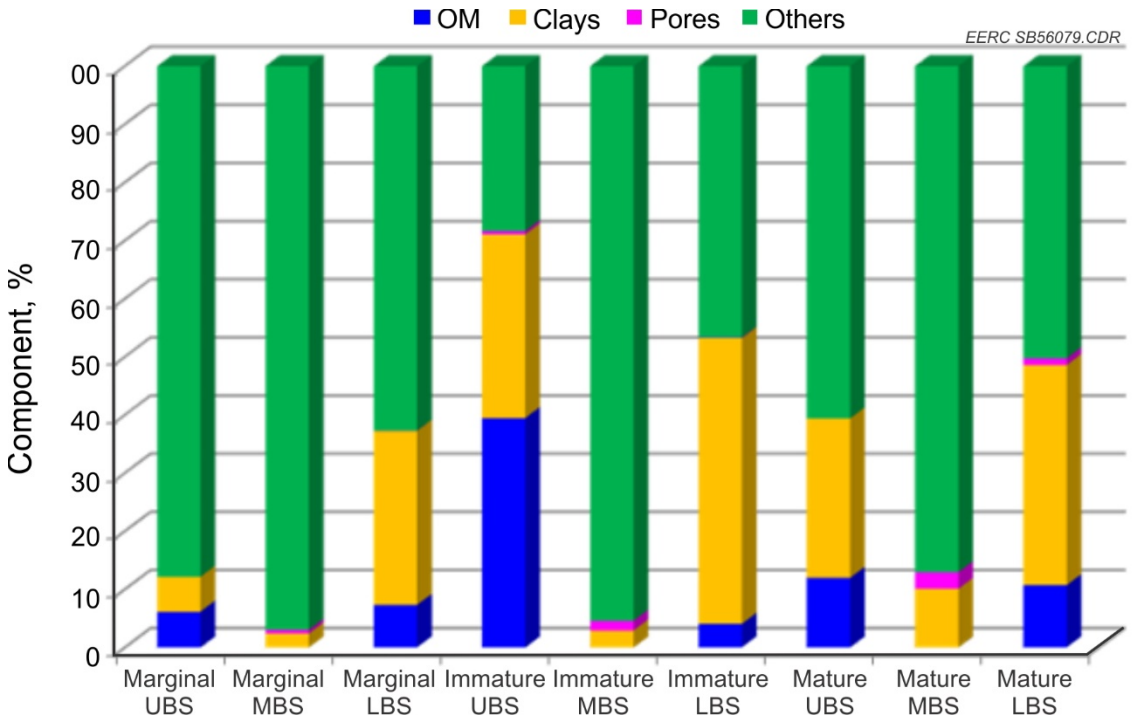

Figure 16. Summary of the mineral composition of Bakken shale and reservoir samples and a Marcellus shale sample determined using AMICS.

In addition to the mineralogical variations between different lithofacies units (UBS, MB, LBS) within each well, the results in Table 2 and Figures 15–17 also illustrate lateral variability for Bakken lithofacies between the three locations that were sampled for this study. For example, the OM content of the Upper and Lower shales are similar for the mature (12% and 11%) and marginally mature (6% and 7%) locations, but are drastically different between the UBS (39%) and LBS (4%) for the immature location. Laterally, there are significant differences in the OM content across the three locations; e.g., for the UBS, the OM content is 12% (mature), 6% (marginal maturity), and 39% (immature). Similar analysis can be made for any mineral species of interest in Table 2 to show both vertical and lateral variability. Given the lateral distance between wells, variations in mineralogy or OM content are not surprising; however, it is an important reminder of the challenges with respect to estimating the CO_2 storage resource potential of an entire formation.

One of the key aspects of the AMICS approach is the ability to generate mineral maps of the various minerals present in a given sample for a more powerful, succinct comparison of different samples or different lithofacies. In Figure 15, the maps illustrate the powerful image visuals that vividly show differences between the UBS, MB, and LBS at each location. These maps allow for qualitative assessment of potential CO_2 flow pathways and sorption sites through the visualization of pores, fractures, and clay and OM occurrence. Furthermore, the maps easily demonstrate vertical or lateral variability between lithofacies units based on a given mineral such as microcrystalline quartz (chert) or illite.

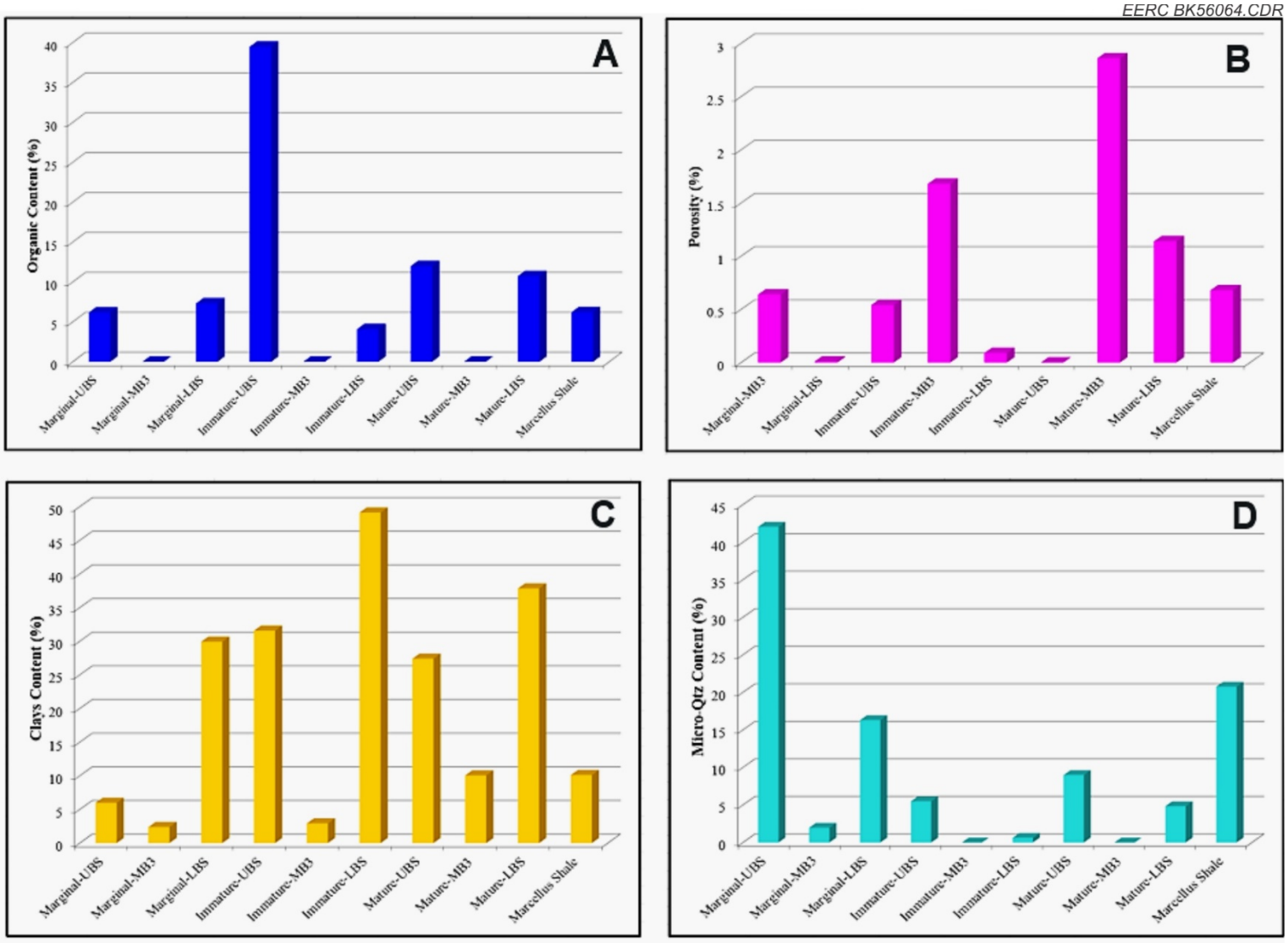

Figure 17. Charts of key individual components in Bakken and Marcellus samples.

OM Porosity and Fracture Networks

The main objective of this task was to develop better image-based approaches for improved estimates of the porosity of organic-rich shale samples, especially porosity associated with OM (PAOM). To achieve this aim, an advanced image analysis (AIA) protocol using Ilastik was developed and used to quantify the PAOM, the void space within fractures and matrix porosity. The porosity obtained from 2-D image analysis was reported as area percent. As a result, image-derived porosity cannot be directly compared with traditional porosity data obtained from volumetric measurements; however, the distribution of porosity between the different void types is still valid and can provide useful insight into potential fluid and/or CO_2 migration pathways.

A summary of the image analysis-based results is shown in Figures 18 and 19 for the UBS, MB, and LBS samples from the three well locations. Figure 18 shows the total porosity estimates obtained from the AIA method, matrix-only porosity, and PAOM. For organic-rich shales, the PAOM is larger than matrix-only porosity, except for the lower and upper shales of the marginal and immature location samples. Also, as expected, the middle members have higher porosity than the shales. A key observation that has significant implications for CO_2 storage and transport mechanisms is the fact that the larger fraction of organic-rich shale porosity is associated with OM, which is consistent with previous work and findings conducted at the EERC (Sorensen and others, 2018).

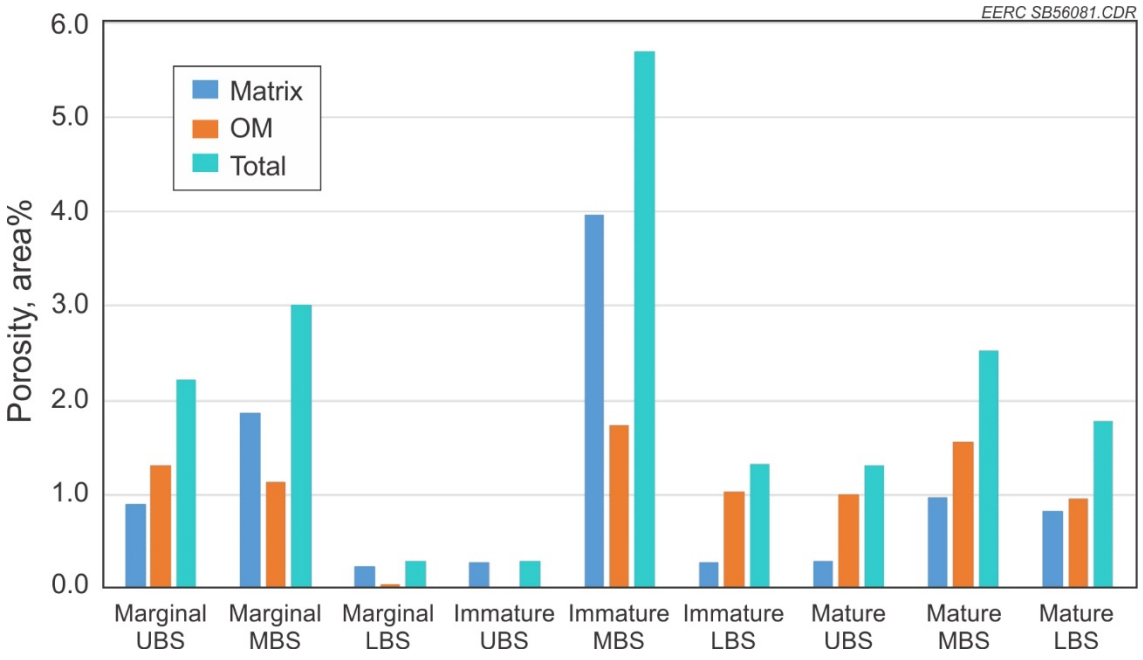

Figure 18. Porosity obtained from AIA techniques.

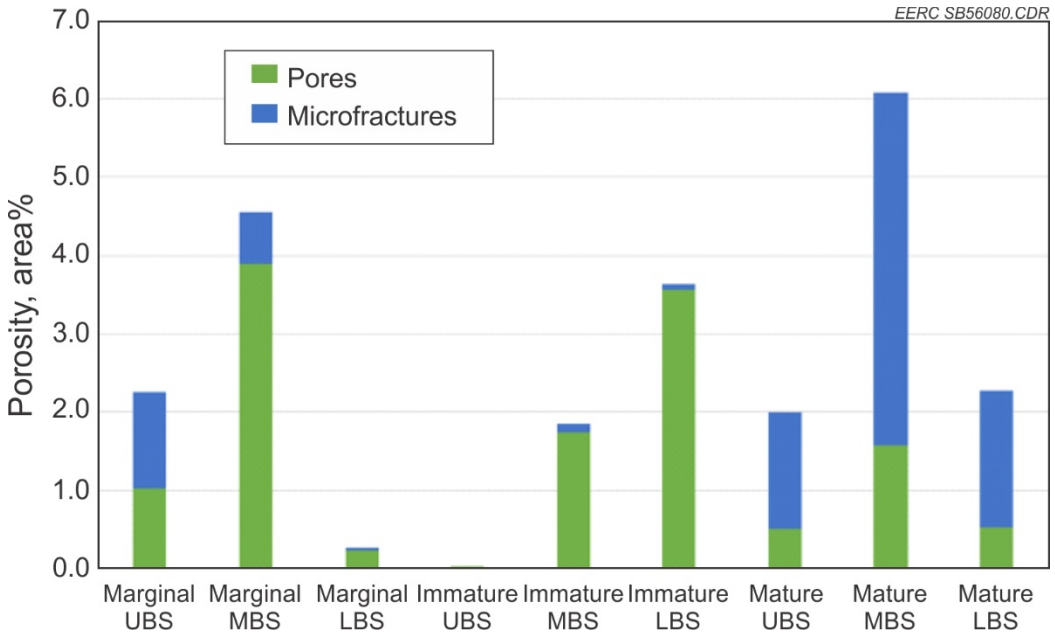

Figure 19. The distribution of void space between pores and fractures within the samples.

Figure 19 illustrates the distribution of void space between pore spaces and fractures within the samples as determined using the AIA method. Again, most of the porosity and fractures in the shales occur within the OM, whereas the Middle Bakken samples contain very little OM and the bulk of the porosity occurs within intergranular pores and fractures. The ability to distinguish and quantify void space within pores versus fractures is a significant step in better understanding the primary mechanisms of fluid and CO_2 flow and storage within tight reservoirs. Additional work is ongoing at the EERC to develop image analysis-based methods to further differentiate between natural fractures and those induced during core collection and handling, as well as to determine connected versus nonconnected pore and fracture networks.

Proposed Modified Storage Equation

The following section described the details of how the AIA method was applied to incorporate image-based parameters into the existing DOE NETL equation for estimating the CO_2 mass storage resource potential for organic-rich shale formations. This modified equation calculates efficiency factors for four solid-phase storage based on image analysis rather than using literature-based values or the bulk properties of the rock samples. As previously described, the proposed updated equation is as follows:

$$G_{CO_2} = V_e\left[\rho_{CO_2}\phi_{PF}E_{\phi} + M_{OMCO2}V_{OM}E_{OM} + M_{ClaysCO2}V_{Clays}E_{Clays} + Others\right] \quad \text{[Eq. 4]}$$

Where:

G_{CO_2} = CO_2 mass storage resource (kg)
V_e = Effective reservoir volume available for CO_2 storage (m^3)
ρ_{CO_2} = Density of CO_2 at reservoir temperature and pressure (kg/m^3)

ϕ_{PF}	=	Total free-phase void volume fraction due to pores and fractures
E_{ϕ}	=	Efficiency factor associated with free-phase storage
F_{OM}	=	Fraction of solid OM within the effective reservoir volume
M_{OMCO2}	=	Maximum mass of CO_2 adsorbed per unit volume of solid OM (kg/m^3)
E_{OM}	=	Efficiency factor associated with adsorption of CO_2 on OM
F_{Clays}	=	Fraction of clays within the effective reservoir volume
$M_{ClaysCO2}$	=	Maximum mass of CO_2 adsorbed per unit volume of clays (kg/m^3)
E_{Clays}	=	Efficiency factor associated with adsorption of CO_2 on clays
$Others$	=	Contribution from other potential CO_2 uptake mechanisms (kg/m^3)

From Equation 4, E_{ϕ} is defined as the fraction of void space that is accessible to CO_2 for free-phase storage. In the expanded equation, E_{ϕ} was redefined to include two terms: $E_{\phi eff}$, which is the ratio of connected-to-total void volume, and E_D, which is the reservoir fluid displacement efficiency. The displacement efficiency term accounts for the fact that existing fluids in the void spaces in the reservoir have to be displaced during CO_2 injection to create the net void space that can store CO_2. E_D is further divided into a volumetric displacement efficiency (E_{vol}) and microscopic displacement efficiency (E_d). Volumetric displacement efficiency describes the fraction of void volume contacted by injected CO_2 as a result of density difference between the injected CO_2 and the formation fluids. Microscopic displacement efficiency represents the actual fraction of void spaces available for CO_2 storage excluding any irreducible oil (S_{oil}) and/or water (S_{wirr}) saturation. Therefore, E_{ϕ} can be computed as follows:

$$E_{\phi} = E_{\phi eff} E_D \quad \text{[Eq. 5]}$$

$$E_{\phi eff} = \frac{\phi_{con}}{\phi_{PF}} \quad \text{[Eq. 6]}$$

$$E_D = E_{vol} E_d \quad \text{[Eq. 7]}$$

$$E_d = 1 - S_{wirr} - S_{oil} \quad \text{[Eq. 8]}$$

The calculation of E_{ϕ} presented herein is a step toward an improved estimate over conventional methods for organic-rich shales by accounting for factors such as fluid displacement in the reservoir and diffusion of CO_2 as it moves through the rock matrix. Until data become available from field deployment of CO_2 storage in shale reservoirs, the estimation of reservoir fluid displacement efficiency will likely occur through laboratory-based tests and/or reservoir modeling and numerical simulation. The determination of connected versus nonconnected porosity can be achieved by using advanced porosity measurement techniques developed for shales, such as pressure pulse decay (Gilicz and Bodi, 2012; Neuzil and others, 1981), which is a direct measurement of sample permeability and connected (or accessible) porosity. To further understand void space within pores versus fractures, advanced image analysis techniques were employed by this study to identify and quantify the fraction of void space that was in fractures versus pores. Additional image analysis-based methods are being explored and developed to further differentiate between connected versus nonconnected fractures and pores. Once these methods are developed, it will greatly help to expand our current

knowledge of CO_2 and fluid flow mechanisms in tight reservoirs and help to better understand the sorptive components that CO_2 could contact as it migrates through the reservoir.

Volume Fraction of Organic Matter (V_{OM}) and Clays (V_{Clays})

The volume fractions of OM and clays within the effective reservoir volume were determined using AMICS software, where a combination of FESEM backscattered electron images and x-ray chemical composition data were used to derived the mineralogy on a particle-by-particle and grain-by-grain basis. Within the AMICS software, the volume fraction of each mineral component (including total porosity) can be calculated based on a stereological volume approximation where the sum of 2-D areas determined from image analysis is proportional to the volume. Therefore, the volume fraction of OM, V_{OM}, and of clays, V_{Clays}, shown in the second and third terms of Equation 4 are computed from AMICS by the following equations:

$$V_{OM} = \frac{1}{M}\sum_{i=1}^{M}\sum_{j=1}^{N}\frac{A_{(OM)ij}}{A_{Ti}} \quad \text{[Eq. 9]}$$

and

$$V_{Clays} = \frac{1}{M}\sum_{i=1}^{M}\sum_{j=1}^{N}\frac{A_{(Clays)ij}}{A_{Ti}} \quad \text{[Eq. 10]}$$

where $A_{(OM)ij}$ is the area of OM particle *j* in Image *i* and A_{Ti} is the total area of Image *i*; N is the total number of particles analyzed per image; M is the total number of images per sample. The maximum mass of CO_2 adsorbed by each component will have to be determined from a CO_2 adsorption experiment, where "pure" component samples are isolated from the rock matrix and used to perform the adsorption experiment.

Efficiency Factors for Adsorption onto OM (E_{OM}) and Clays (E_{Clays})

The efficiency factors associated with CO_2 adsorption on OM and clays surfaces were computed from advanced image processing protocols using a combination of ImageJ (Rasband, 2016), Fiji (Schindelin and others, 2012), and Ilastik (Sommer and others, 2011) software packages. This method, shown in Figure 20 and referred to as shared border analysis (SBA), assumes that the CO_2 present in any pore space can only adsorb onto surfaces that are exposed to the pore. Hence, the fraction of the surface exposed to the pore space is approximately proportional to the fraction of CO_2 that can adsorb on the surface of the OM or clay particle. Based on segmented high-resolution FESEM images, the calculation of these component-specific sorption efficiency factors occurred through a series of steps illustrated using OM particles as follows:

1. The lengths of the border shared by OM particles and connected pores or fractures was computed and normalized to the total border surrounding each particle.

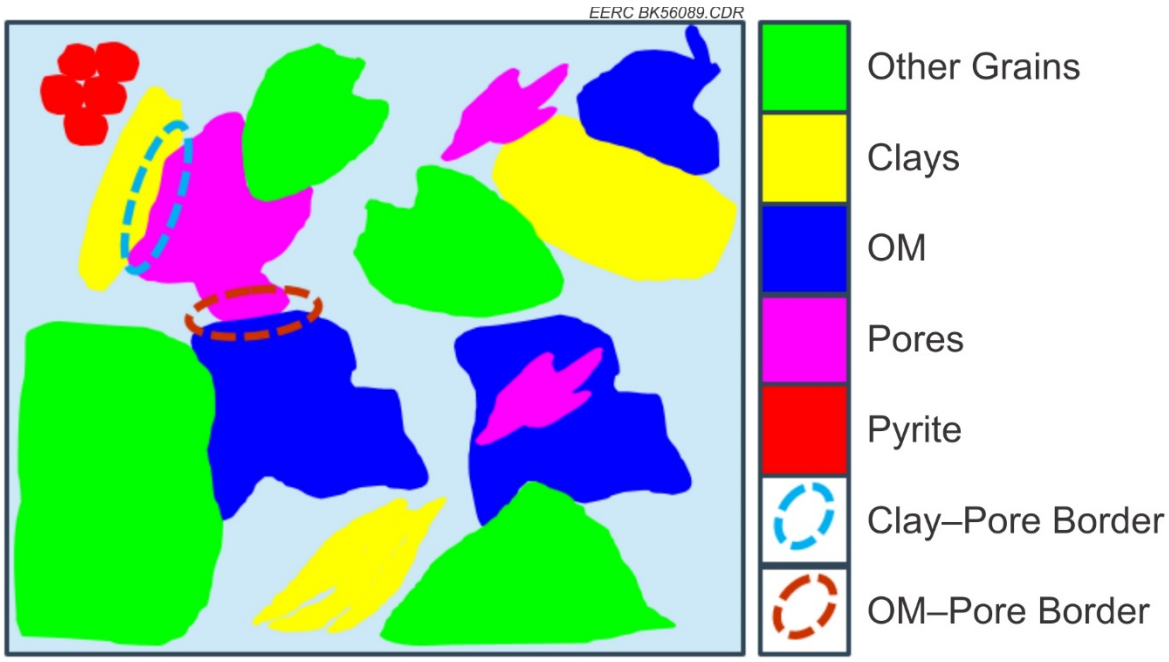

Figure 20. Schematic illustration of SBA using clay and OM borders.

2. The average of the normalized shared borders over all OM particles in an image was determined.

3. An overall average of normalized shared borders computed over all images obtained for a given sample was used as an estimate of the efficiency factor associated with adsorption of CO_2 onto OM for the sample.

The process outlined in Steps 1–3 above was repeated for each component that could potentially adsorb CO_2 to obtain an estimate of the efficiency factor associated with adsorption of CO_2 on particles of that component for a given sample. Hence, the equations for calculating E_{OM} and E_{Clays} are given by

$$E_{OM} = \frac{1}{M}\sum_{i=1}^{M}\frac{1}{N}\sum_{j=1}^{N}\frac{\delta_{(OM-P)ij}}{C_{(OM)ij}} \quad \text{[Eq. 11]}$$

and

$$E_{Clays} = \frac{1}{M}\sum_{i=1}^{M}\frac{1}{N}\sum_{j=1}^{N}\frac{\delta_{(Clays-P)ij}}{C_{(Clays)ij}} \quad \text{[Eq. 12]}$$

where M is the total number of images analyzed per sample, N is the total number of OM or clay particles analyzed per image, $\delta_{(OM-P)ij}$ is the length of OM border shared with connected porosity for OM particle j in Image i, $C_{(OM)ij}$ is the circumference of OM particle j in Image i,

$\delta_{(Clays-P)ij}$ is the length of clay particle border shared with connected porosity for clay particle *j* in Image *i*, and $C_{(Clays)ij}$ is the circumference of clay particle *j* in Image *i*.

Determination of CO_2 Adsorption Terms

This approach assumes that the maximum mass of CO_2 adsorbed by each component (e.g., M_{OMCO2} or $M_{ClaysCO2}$) is determined from CO_2 adsorption experiments, where "pure" component samples are isolated from the rock matrix and used in the adsorption testing. The experiments are expected to model Langmuir monolayer adsorption where the asymptotic limit is proportional to the maximum mass of CO_2 adsorbed onto the particles at in situ pressure and temperature. The mass determined this using crushed particles represents a maximum potential adsorption quantity because some of the surfaces exposed to CO_2 in crushed sample experiments may never be exposed to CO_2 in the natural environment. However, the derived efficiency factors that rigorously require surfaces to be exposed to connected pores or fractures in 2-D cross-sections of natural samples effectively accounts for and reduces the maximum mass obtained from Langmuir experiments.

Key Assumptions of the Approach

The main assumptions made in the course of deriving the CO_2 storage estimation equation for organic-rich shales include:

1. The volume fraction of OM, clays, or other adsorbing solid-phase components was approximated by the sum of 2-D areas of all particles of that component that are analyzed. This approximation is consistent with well-known stereological approximation (Gundersen and Jensen, 1987; Howard and Reed, 1998; Weibel, 1979) for estimating 3-D volumes based on 2-D areas of sample particles.

2. The efficiency factor associated with adsorption onto a given mineral component (e.g., OM or clays) was assumed to be proportional to the fraction of the component's particle borders shared with connected pores or fractures (Figure B-1).

3. Other CO_2 uptake mechanisms, including carbonate dissolution/precipitation, solubility in formation fluids and/or hydrocarbon fluids, trapping in the interlayers of swelling clays, are quite different from a surface adsorption phenomenon and so are not considered in this equation. However, these processes can be accounted for by using the "Others" term in Equation 4 if suitable formulations are derived. This is the subject of ongoing development effort.

4. CO_2 adsorption onto other major mineral grains such as quartz and feldspars was assumed to be negligible.

5. Surface coverage by CO_2 molecules was assumed to be a noncompetitive, monolayer Langmuir-type adsorption process.

6. CO_2 adsorption onto the surfaces of a given mineral component of the rock was assumed to be independent of other components; hence, the contributions can be accounted for by using an additive model.

The additional potential CO_2 uptake mechanisms described in Assumption 3 above involving solubility in formation fluids, carbonates, etc., can be accounted for by using the "Others" term in Equation 4 if suitable formulations are derived. This is the subject of ongoing development efforts. By taking into consideration the key assumptions described above and the fact that OM and clays are the dominant adsorbing components of Bakken organic-rich shales and similar shale formations, the overall image-based CO_2 mass storage resource estimation equation for organic-rich shale reservoirs can be represented as:

$$G_{CO_2} = V_e\left[\rho_{CO_2}\phi_{PF}E_{\phi} + M_{OMCO2}F_{OM}E_{OM} + M_{ClaysCO2}F_{Clays}E_{Clays}\right] \qquad \text{[Eq. 13]}$$

Clay and Organic Matter Efficiency Factors and Total Fractions

The results of using advanced image analysis techniques to calculate the efficiency factors for CO_2 adsorption on clays, OM, and their corresponding total fractions in the Bakken sample matrices are shown in Table 3. These results demonstrate the order of magnitude of the different parameters derived by this effort and also illustrate the variability that exists between samples of the Bakken shale.

Table 3. Clay and OM Fractions and Efficiency Factors Calculated from Advanced Image Analysis

Well	Lithofacies	$E_{\_Clays}$	$E_{\_OM}$	$F_{\_Clays}$	$F_{\_OM}$
22388	UBS	0.00013	0.02394	0.272	0.219
22388	LBS	0.00015	0.02649	0.259	0.210
16974	UBS	0.00546	0.08250	0.281	0.252
16974	LBS	0.00141	0.03771	0.205	0.128
18829	UBS	0.00055	0.01304	0.206	0.373
18829	LBS	0.00027	0.03180	0.234	0.098

Flow-Through Testing and Adsorption Testing

Results of dynamic CO_2 flow-through testing are shown in Figures 21 through 26. The plots shown were corrected for known systematic leak rates that were determined both pre- and posttesting. The data sets shown have been averaged to the minute and also converted to show the mass equivalent of the volumetric information collected. Thermodynamic properties for CO_2 including viscosity and compressibility were obtained from NIST and were used in the analysis of pump volumes and permeability calculations (National Institute of Standards and Technology, 2019). Permeability was calculated using Darcy's law, while permeation rate for each sample was determined based on Equation 6 where P = permeation rate in cm/day, Q = volumetric flow rate (mL/min), A = sample area (cm^2), and Ø = sample porosity (fraction):

$$P = (\frac{Q}{A})/\emptyset \quad \text{[Eq. 14]}$$

NMR scans were performed before and after testing on each of the three samples. 1-D T2 relaxation data and 2-D maps are useful for gaining better insights into potential pore sizes that are accessed by CO_2 as it flows through the core during flow-through experiments. Knowledge of the accessed pore sizes is invaluable for predicting CO_2 injectivity and migration for/or CO_2 storage and/or CO_2 EOR applications.

Upper Bakken Shale, 122806

Figure 21 shows the results of the flow-through testing for the UBS Sample 122806. This sample was cut from the core sample in a parallel-to-bedding orientation and tested for a period of 500 hours (21 days). The average total flow rate over the course of testing was determined to be 0.0006 mL/min. Gaps in the data set are the result of communication errors with the data acquisition system. However, as shown, the data resume the same trend as recorded prior to the gap. As Figure 21 demonstrates, the injection pump rate was higher (0.0007 mL/min) throughout the test when compared to the receiver pump (0.0005 mL/min). The observed difference between the total CO_2 volume injected (blue) versus the total volume received (orange) is notable when compared to the total volume injected. In this case, the difference between the two curves is 2.6 mL. The trend shown in Figure 21 suggests that connected flow was achieved very early in the experiment and was sustained through the experiment. Interpretation of posttest Micro CT data revealed several microfractures occurring along bedding planes parallel to the direction of flow (Figure 22). However, Figure 23 presents the same data set during the first 30 hours of testing. The green curve represents the difference between injected and received volumes and is presented as the mass equivalent. As shown, a pronounced curve developed during the first 5 to 10 hours of testing. It is believed that, during this period, CO_2 migrated along the fracture planes within the sample and simultaneously contacted and sorbed onto OM occurring along or in close proximity to the fractures. The curves continued to deviate over the test duration, suggesting that equilibrium may not have been achieved. A possible mechanism for this overall trend could be that while CO_2 flow was dominated by the fracture permeability, over the duration of the test the CO_2 could have continued to slowly permeate from the fracture(s) into the sample matrix where it was retained in pore spaces and also through sorption with OM (and possibly clay minerals).

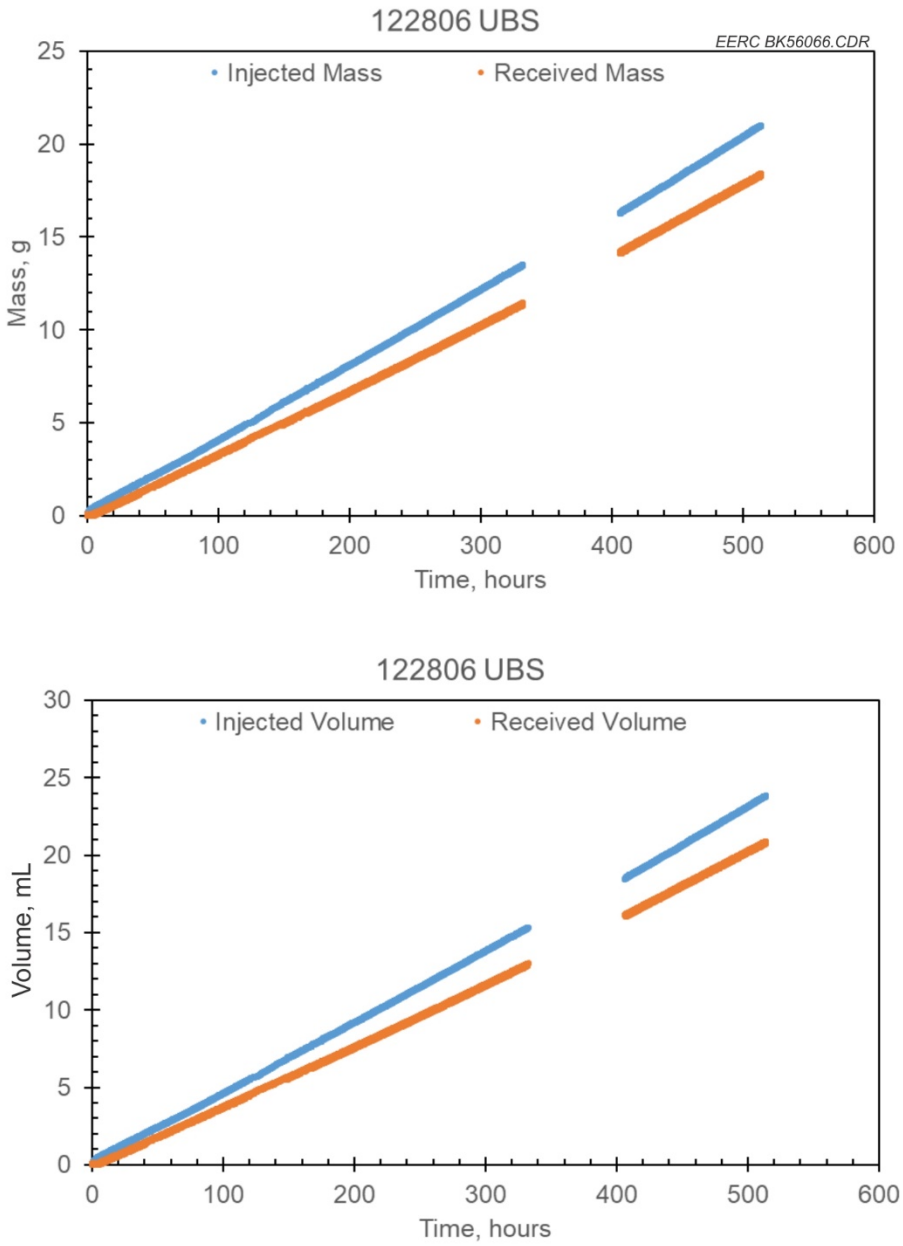

Figure 21. Sample 122806 UBS: two curves are presented showing the volume and mass equivalent results. The permeability of this sample was determined to be 7.6 nD.

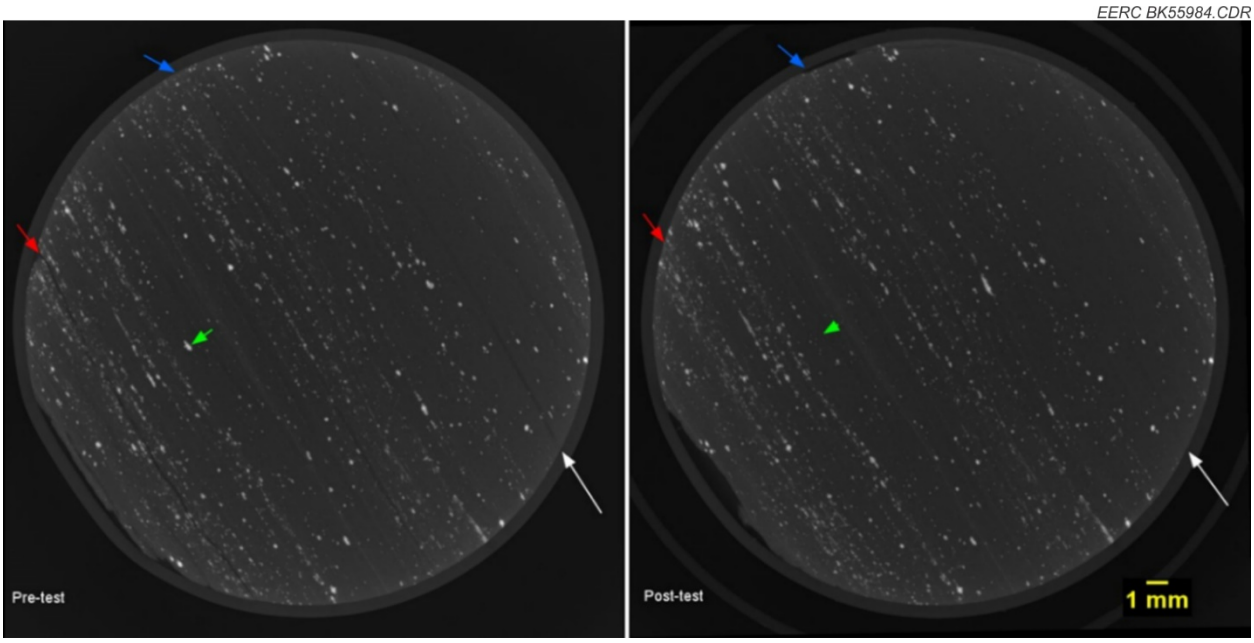

Figure 22. Processed Micro CT data highlighting the presence of fractures in Sample 122806. The pretest sample condition is shown on the left, and the posttest is on the right.

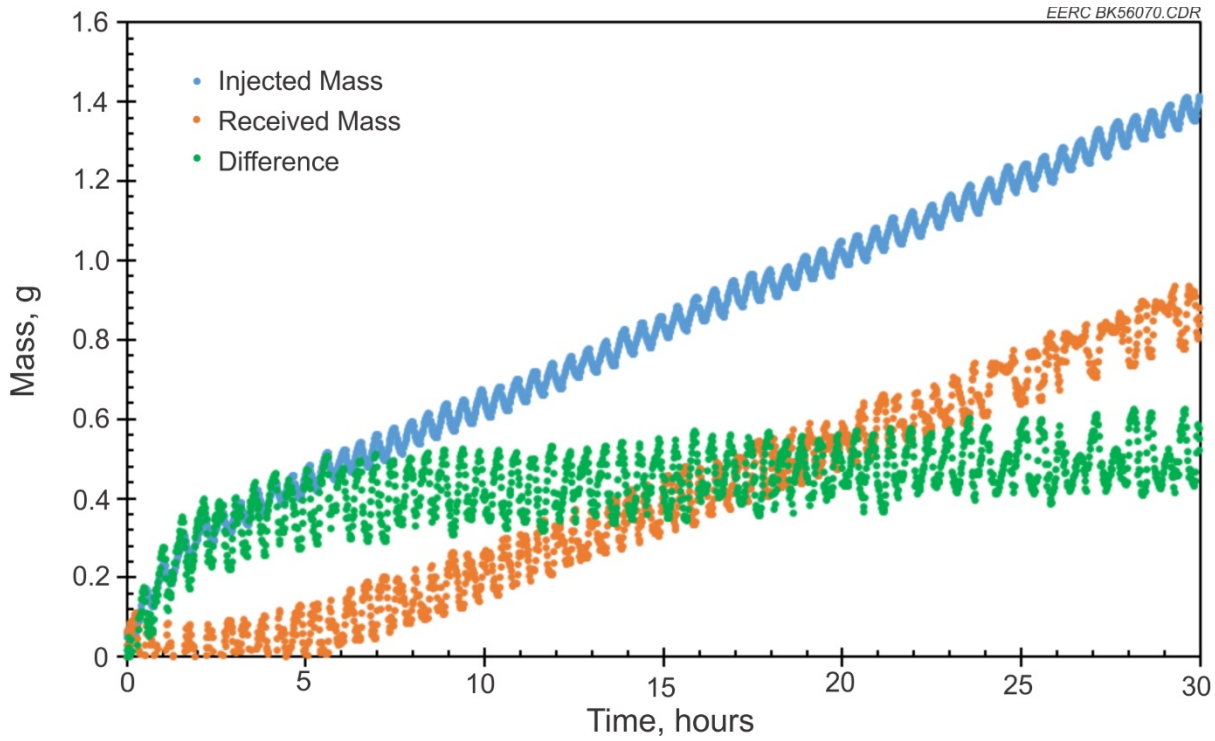

Figure 23. Data collected from UBS Sample 122806 show a distinct curve taking place during the early stages of testing.

Figures 24 and 25 show a selection of FESEM images taken on the inlet and outlet faces of the core plug, respectively, before and after CO_2 exposure tests. Images A, C, and E were obtained before CO_2 exposure, while Images B, D, and F were taken after exposure. Figure 24A shows the general view of the sample inlet surface with OM and pyrite grains in the rock matrix. Image B shows a generalized view of the surface after exposure but not from the same location. The fracturing of the sample shown in Image B is an illustration of some of the challenges that accompany such types of experiments, where relocation to the exact spot after testing is further complicated by the cracking during testing. However, Images C and D are exact spots before and after exposure and show some erosion of the surface on the lower right corner of Image D. It appears the CO_2 flow was not evenly spread over the surface and preferential flow pathways may have removed some of the sample material, especially considering that the left portion of the image does not show similar erosional features. Images E and F are not the same location on the sample, but show a close-up view of the mineral textures and morphologies. It appears some geochemical processes might have occurred to change grain textures as seen on Image F compared to Image E.

The images shown in Figure 25 are direct pairs of the same frame before (A, C, E) and after exposure tests (B, D, F) obtained on the outlet face of the core. The big OM particles (Images A and B pair) do not appear to show major changes, although hydrocarbon mobilization was observed in Bakken shales exposed to CO_2 based on NMR analysis and gas chromatography/flame ionization detector (GC/FID) analysis of effluents from the flow-through test. Additional Images C/D and E/F pairs taken from the same scene, with E/F illustrating a zoomed-in version of the middle portion of C/D, further demonstrate the lack of significant changes to the OM and the embedded quartz and feldspar grains.

A 1-D NMR scan of the sample yielded measurements of fluid-filled porosity of 2.5% before the flow-through test and 1.0% after the test, which suggests that approximately 60% of the residual fluids were expelled from the core. Figure 26 shows 2-D NMR maps obtained before (A) and after (B) CO_2 flow-through testing. The after exposure map shows a spread in the NMR signal clusters compared to the before test map, which is consistent with mobilization of the hydrocarbon fluids within the core. In addition, analysis of the fluid expelled from the core by GC/FID indicated the presence of hydrocarbons. Given that for organic-rich Bakken shales most of the residual fluids comprise hydrocarbons (light oil, heavy oil, bitumen), these results suggest that hydrocarbons were mobilized and removed from the sample during the CO_2 flow-through experiment.

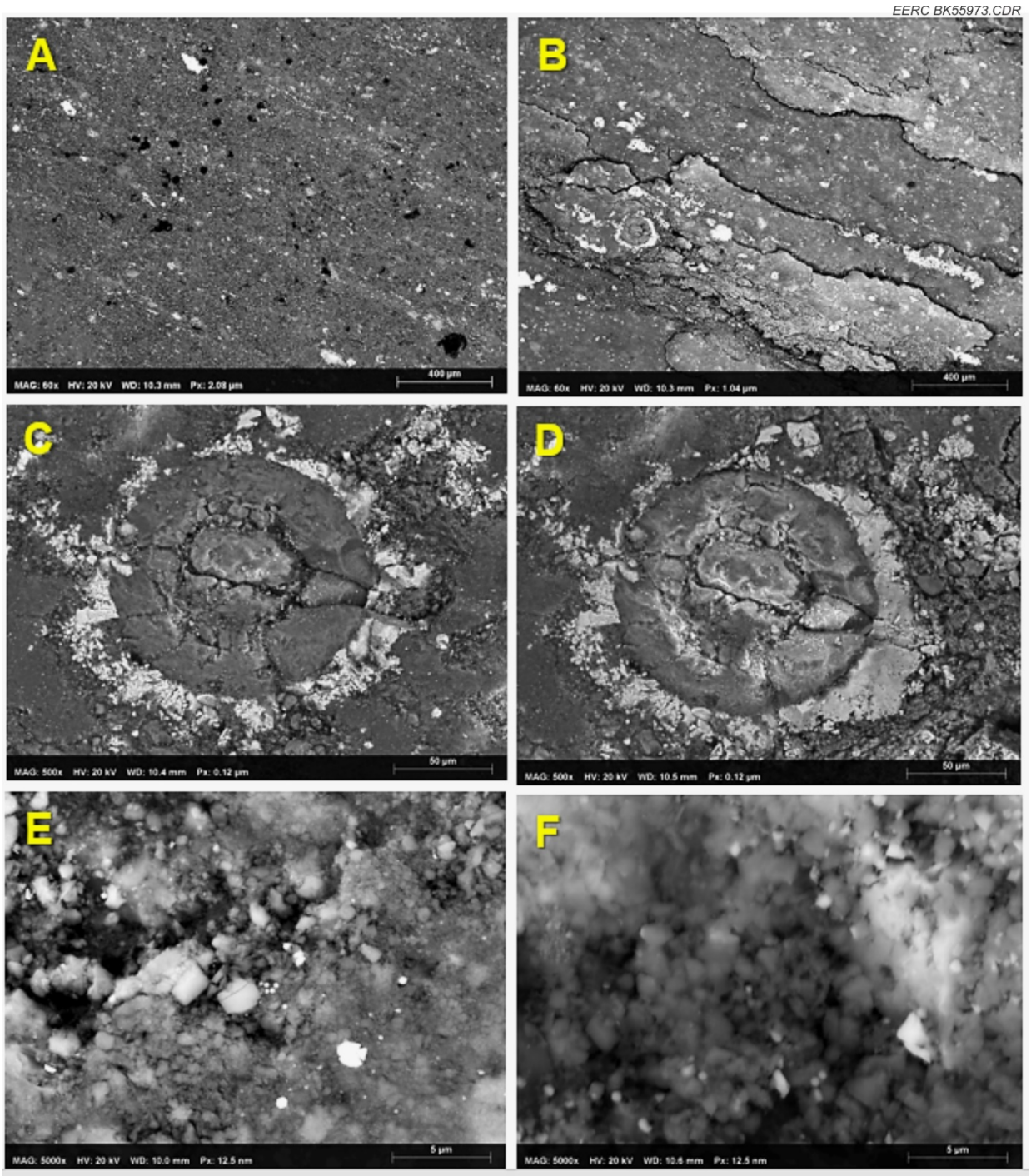

Figure 24. Inlet face of UBS core pre- and postexposure to CO_2. Images A, C, and E are from the preexposure inlet face of the core, and Images B, D, and F are from postexposure inlet face of core (Sample 122806).

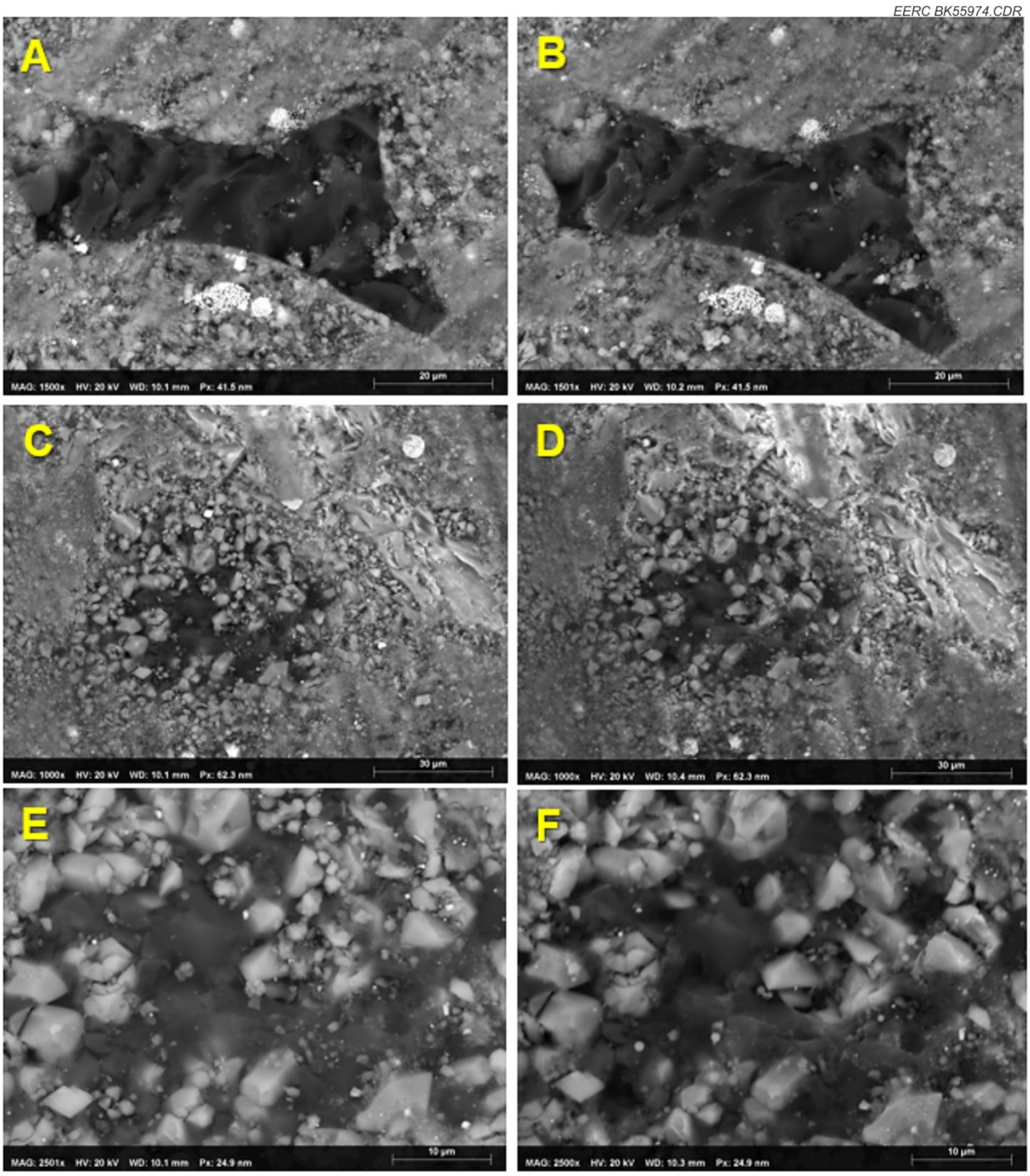

Figure 25. Outlet face of UBS pre- and postexposure to CO_2. Images A, C, E are from preexposure, and Images B, D, F are postexposure (Sample 122806).

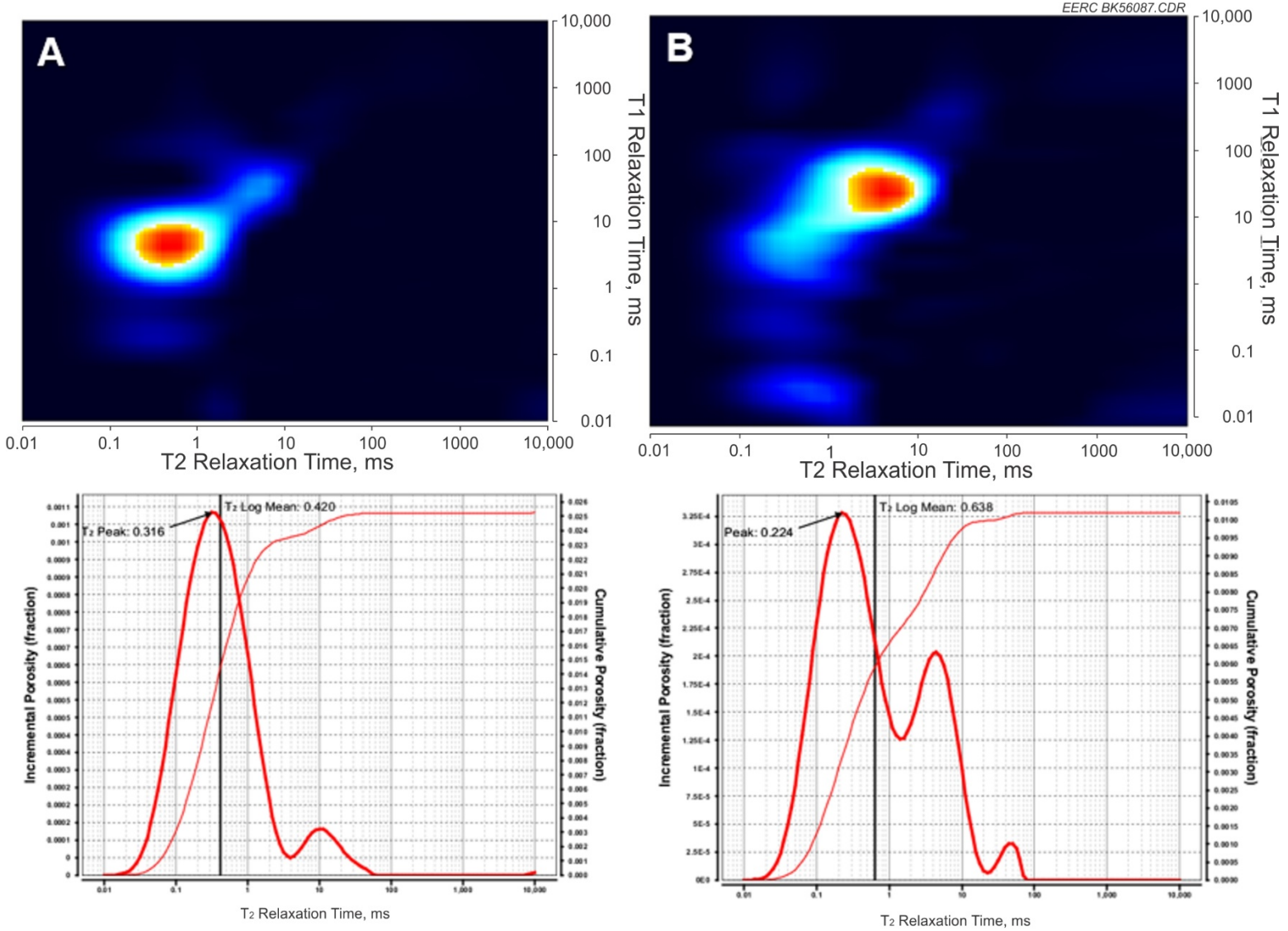

Figure 26. 2-D NMR maps and their corresponding 1-D profiles for UBS before (A) and after (B) exposure to CO_2.

Lower Bakken Shale, 120839

Results of testing for LBS Sample 120839 are presented in Figure 27. The data are presented in volumetric and mass equivalent. This sample was tested in a vertical, or perpendicular to bedding, orientation to mitigate concerns of early CO_2 breakthrough due to fractures along bedding. The test was conducted over a 420-hour time frame. As demonstrated, a consistent injection rate was maintained throughout the test (blue line); however, the receiving pump showed a significant change over the duration of the test (orange line). The green line shows the difference between the two curves. The first 80 hours of testing indicates only a small volume of CO_2 received. This can be attributed to pressure differential draining excess CO_2 from the tubing volume on the outlet side of the core. Over the next 60 hours, very little CO_2 was received in the pump. At approximately 125 hours of test time, CO_2 appeared to break through the core, and a consistent flow was observed for the duration of the test. The total volumetric change between injected CO_2 and received CO_2 was approximately 0.8 mL. While this is a very small volume for a long-duration test, it should be noted that it was nearly 25% of the total injected CO_2. Permeability for this sample was calculated to be 1.4 nD and is believed to be representative of true matrix flow.

Figure 28 shows select images from the LBS sample prior to and following the CO_2 injection test. In this case, the images are not a direct one-to-one match of before and after test locations because it was not possible to relocate to the exact frames after exposure tests. As a result, the images only capture specific features that were compared between the before and after exposure conditions. For example, the spherical OM particles imaged before exposure (Images A, C) are similar to those imaged after exposure (Images B, D), while Images E and F show relatively pristine quartz grains in the sample matrix before and after exposure tests, respectively. Also common in the matrix of this sample were fossil fragments like the one shown in Image A.

NMR work conducted on the LBS sample showed approximately 10.2% of the residual fluids (assumed to be hydrocarbons) in the as-received core were removed during testing. The 2-D map for the lower shale sample (Figure 29) shows that the fluids separated into two distinct clusters after the flow-through test. However, the fluid clusters appear to still be in the same general pore-size population since the relative position on the horizontal axis, which determines pore-size populations, is approximately the same. The fluid cluster separation along the y-axis in the after-test map compared to the before-test map is consistent with expulsion from the inlet to the outlet end of the core.

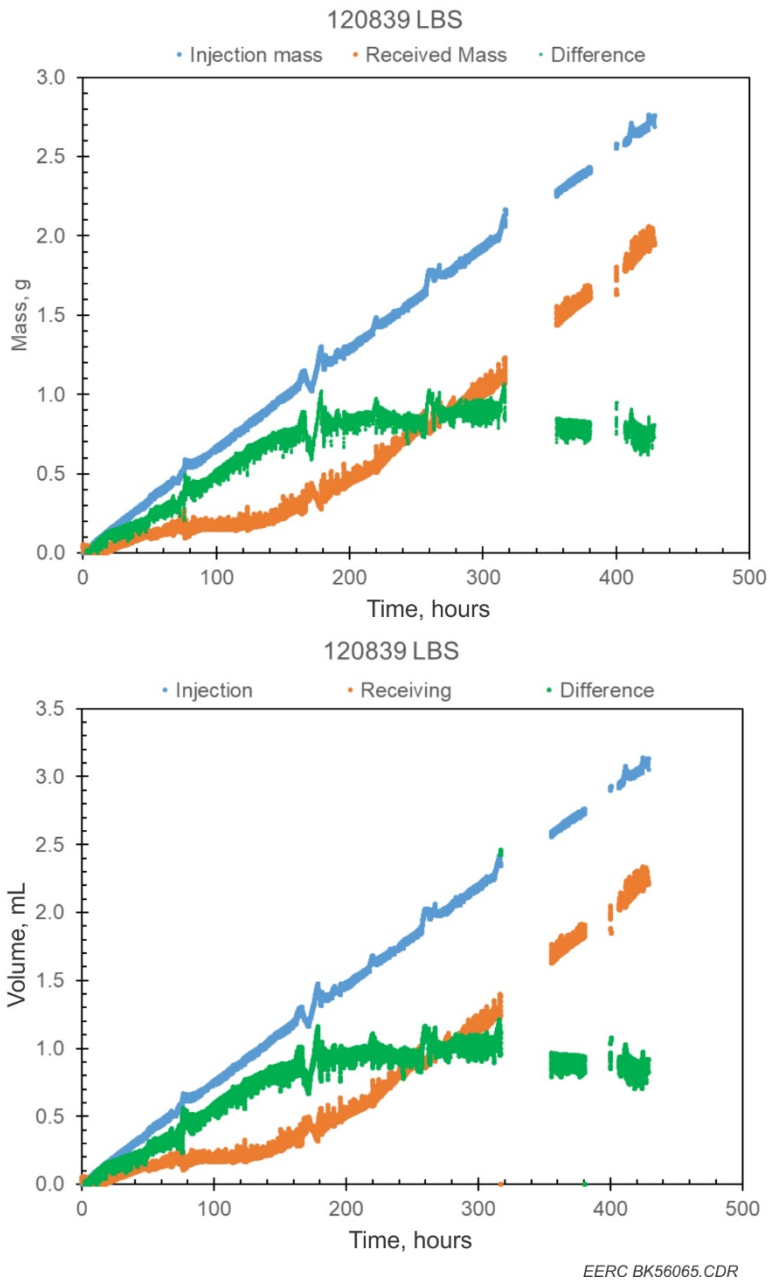

Figure 27. Results for the LBS sample tested. The “hockey stick” behavior of the receiving pump demonstrates a potential for CO_2 retention and then breakthrough of the injected CO_2.

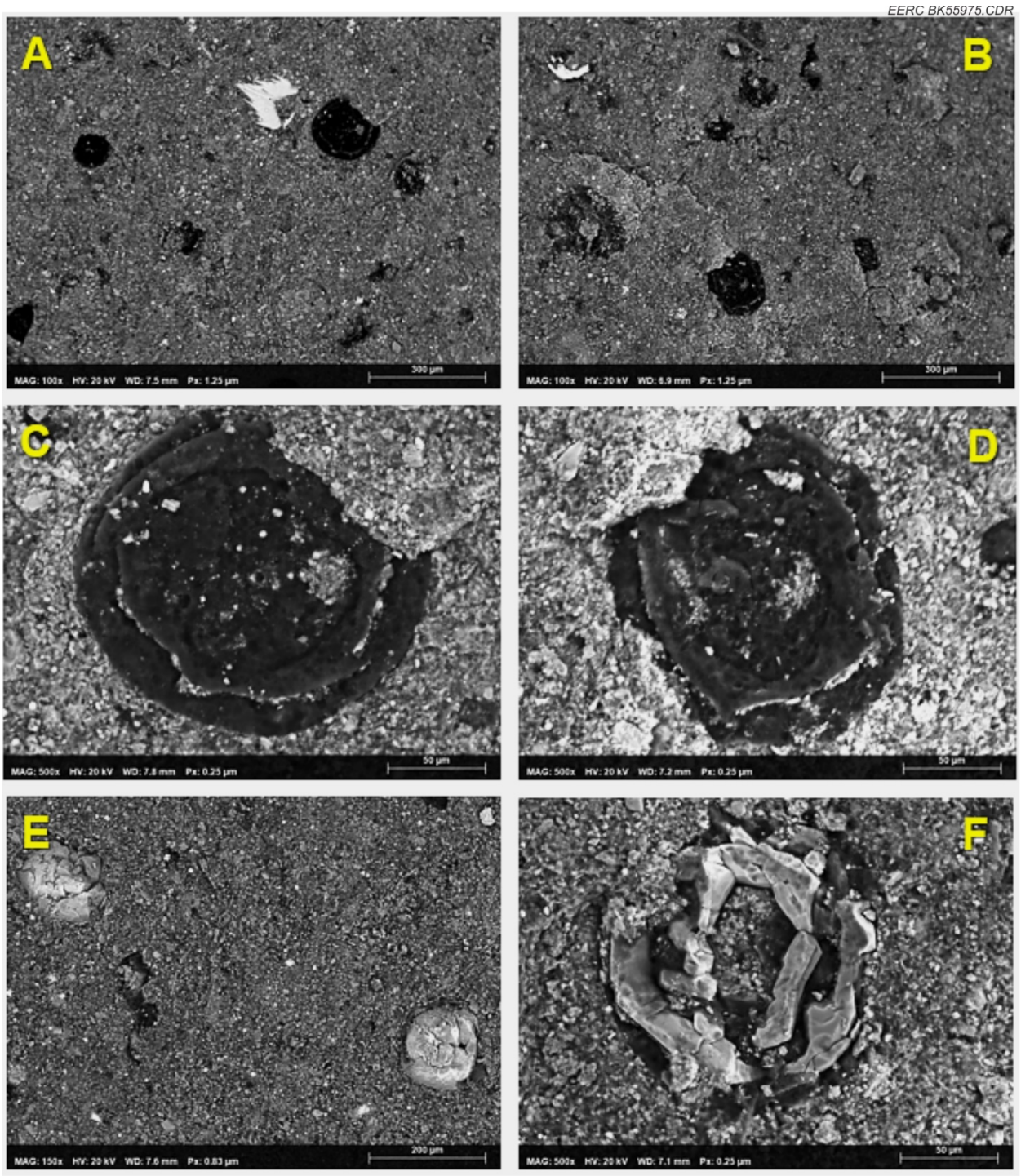

Figure 28. FESEM images of LBS sample before (Images A, C, E) and after CO_2 exposure (Images B, D, F).

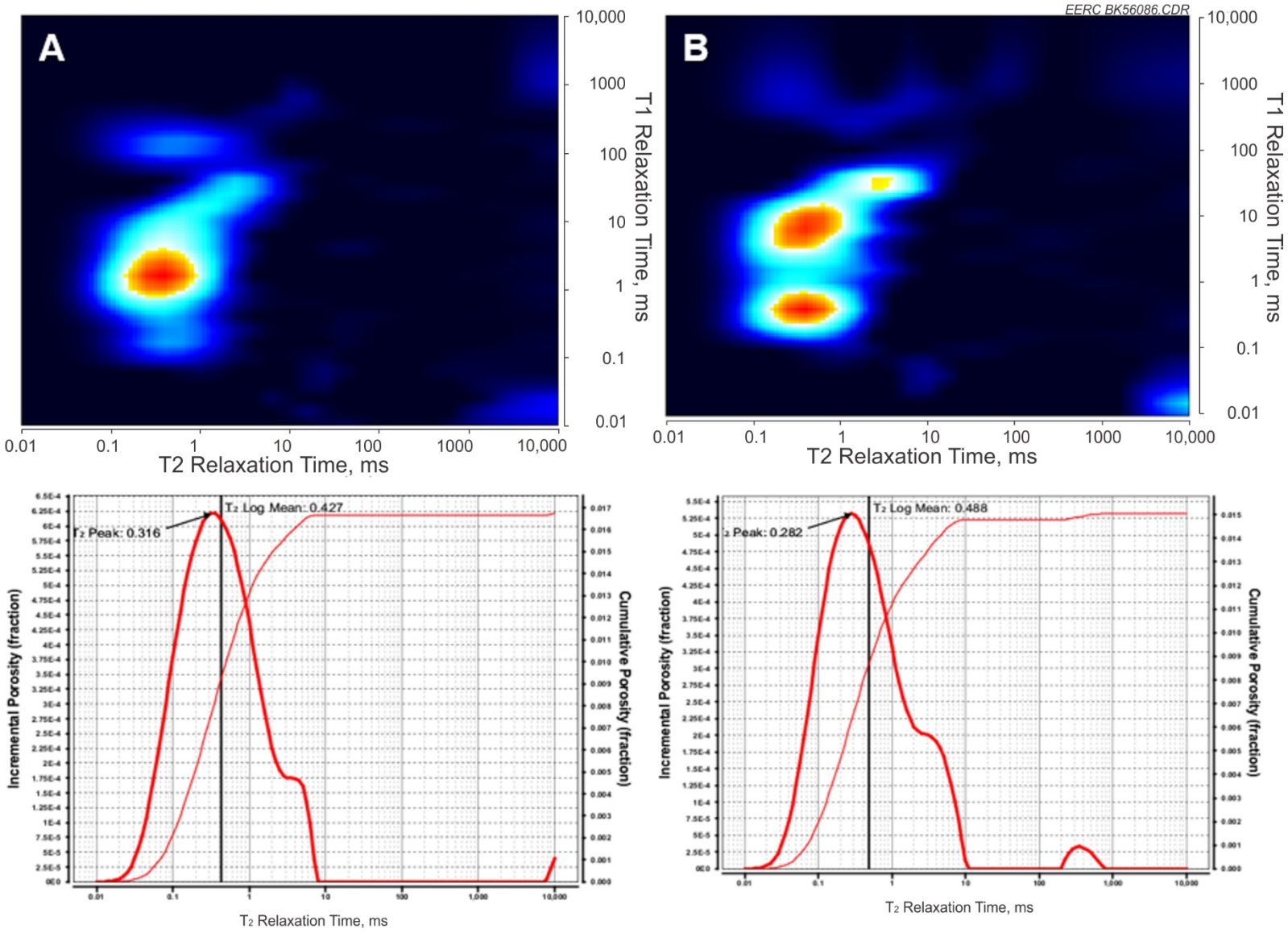

Figure 29. 2-D NMR maps and their corresponding 1-D profiles for LBS before (A) and after (B) exposure to CO_2.

Middle Bakken Siltstone, 122815

While the duration of this test was much shorter than the previous two tests, a similar trend was observed in the injection and receiving pumps. Figure 30 shows the results of testing and demonstrates the difference in connected pores and permeable pathways within the Middle Bakken. The permeability was calculated to be 54 nD, and the permeation rate was 13 cm/day. While a similar total volume of CO_2 penetrated the sample when compared to the UBS, it should be noted that the test duration was only 150 hours compared to the 500-hour duration necessary for the shale. It is believed that matrix flow was achieved in this test, but similar to the UBS sample, the data continue to diverge, suggesting that CO_2 may have still been permeating incrementally smaller pore throats as the test progressed. It is also possible that sorption onto clay minerals could have occurred as the CO_2 continued to permeate into smaller pore spaces. Figure 31 illustrates the same data set during the first 15 hours of testing. Unlike the shale sample, the two flow rates trended together at the onset of testing, then began to diverge after approximately 6 hours. This could be a function of CO_2 connecting through the larger and potentially better connected pore throats early in the test, then penetrating the remaining sample volume for the remainder of flow.

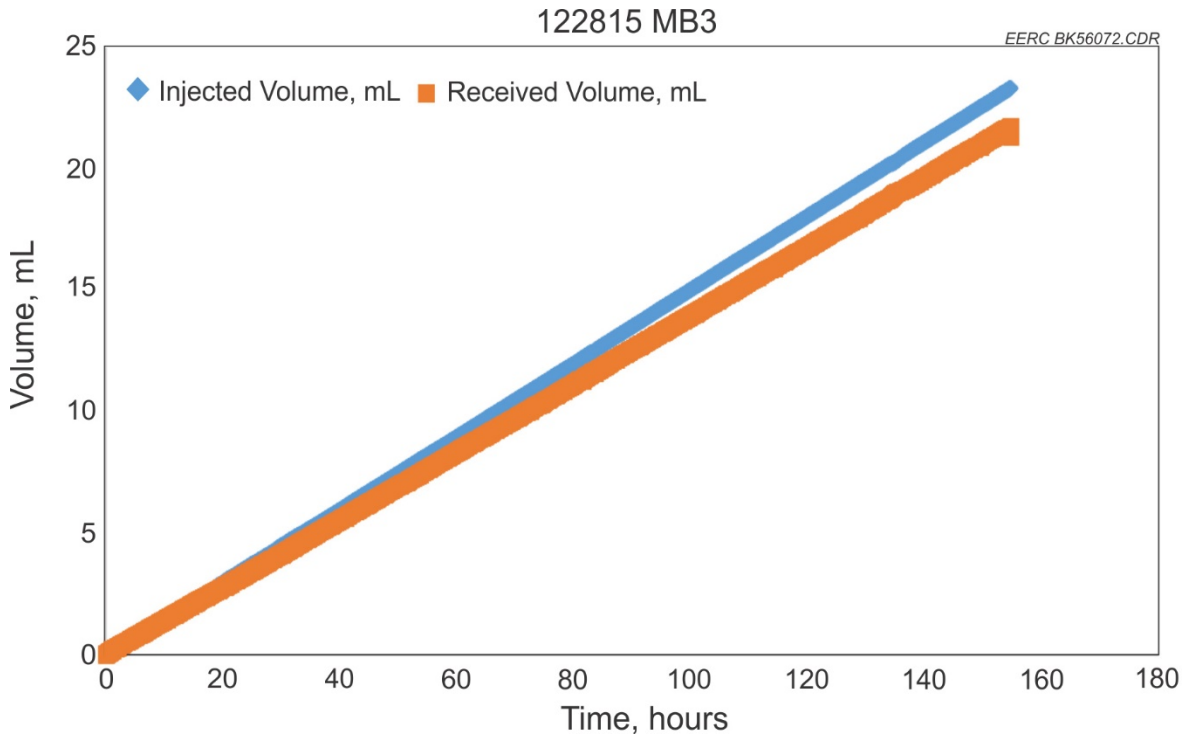

Figure 30. Results of dynamic flow-through testing for the Middle Bakken (MB) siltstone sample tested.

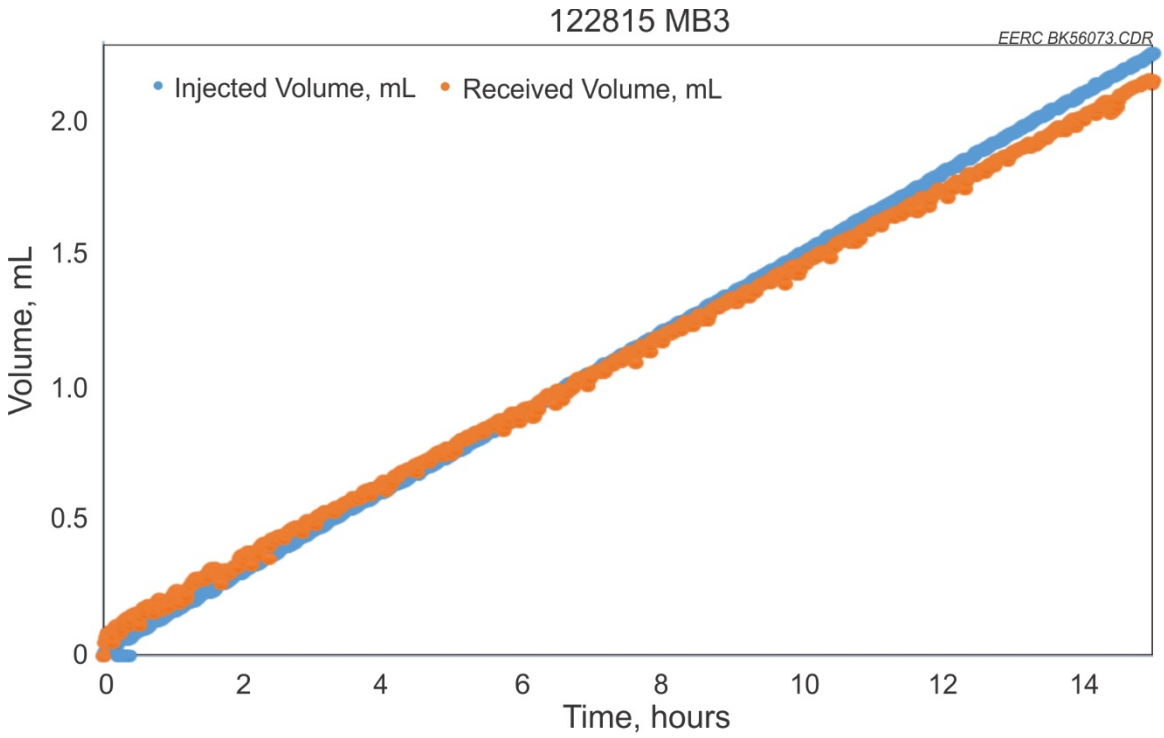

Figure 31. Test results during the first 15 hours of CO_2 flow.

The images obtained from the Middle Bakken sample before and after exposure tests are shown in Figure 32. Similar to the UBS sample, no major changes were observed at this scale. A general surface view of the sample with the scored mark in the middle of Image A (before exposure) and B (after exposure) did not exhibit any obvious changes in morphology or mineralogy. Also shown in Figure 32 are close-up images of before (C) and after exposure (D) taken at the apex of the scored mark. The bright particles are small steel pieces left on the sample during scoring, and the dark and light grains are quartz and calcite, respectively. The zoomed-in images do not appear to show any macroscopic mineral changes.

The NMR results depicted in Figure 33 show similar hydrocarbon mobilization for the Middle Bakken sample. T2 relaxation porosity measurements showed that the fraction of fluids expelled from the Middle Bakken was approximately 17% of the residual fluid volume of the as-received core. While the patterns on the 2-D NMR maps show little spread in the clusters, the 1-D T2 relaxation profiles show shifts in T2 peaks from smaller pore spaces to larger pore spaces. This result suggests that matrix flow was occurring and in-place fluids were being impacted by CO_2 flow.

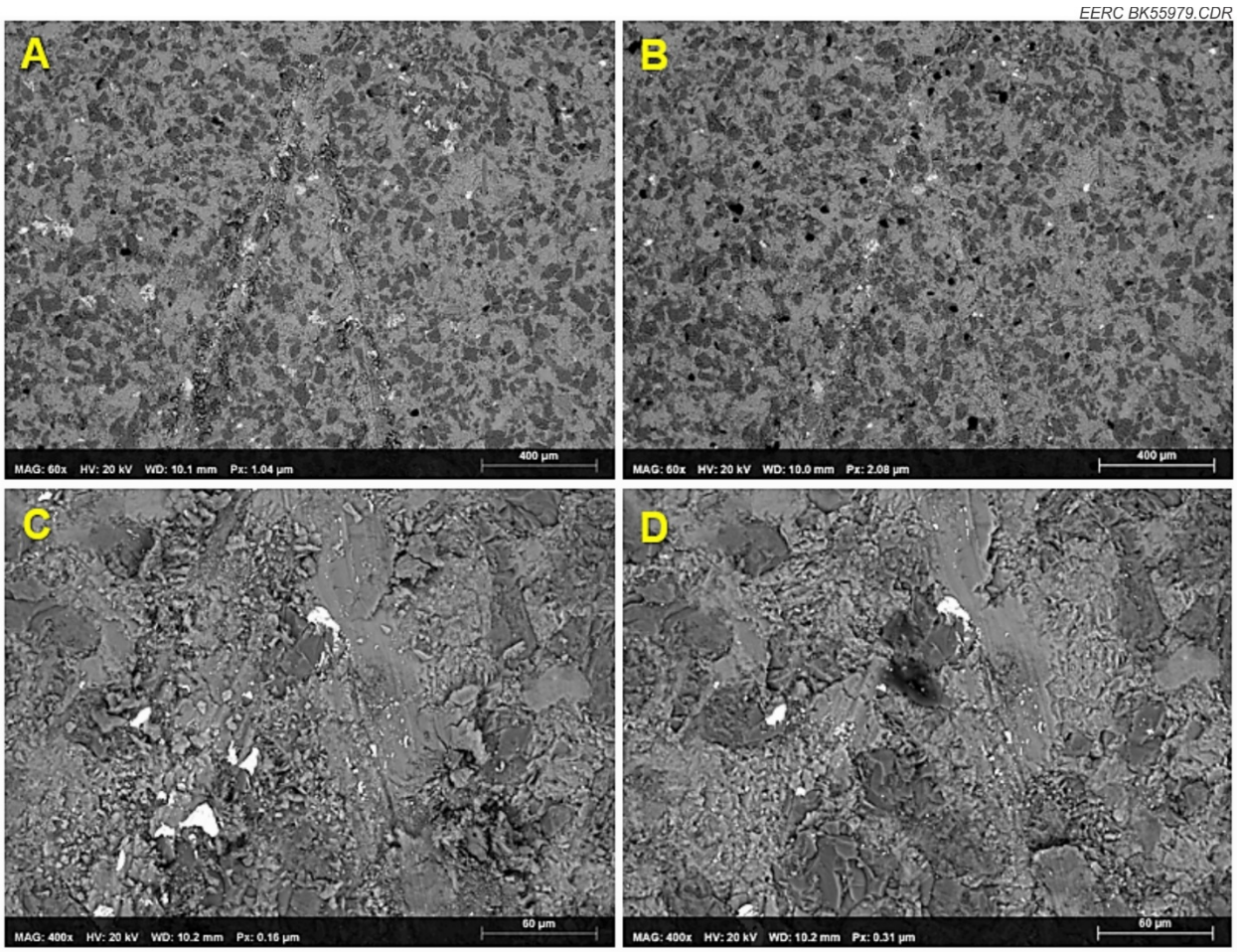

Figure 32. FESEM images of a Middle Bakken sample before (Images A, C) and after CO_2 exposure (Images B, D).

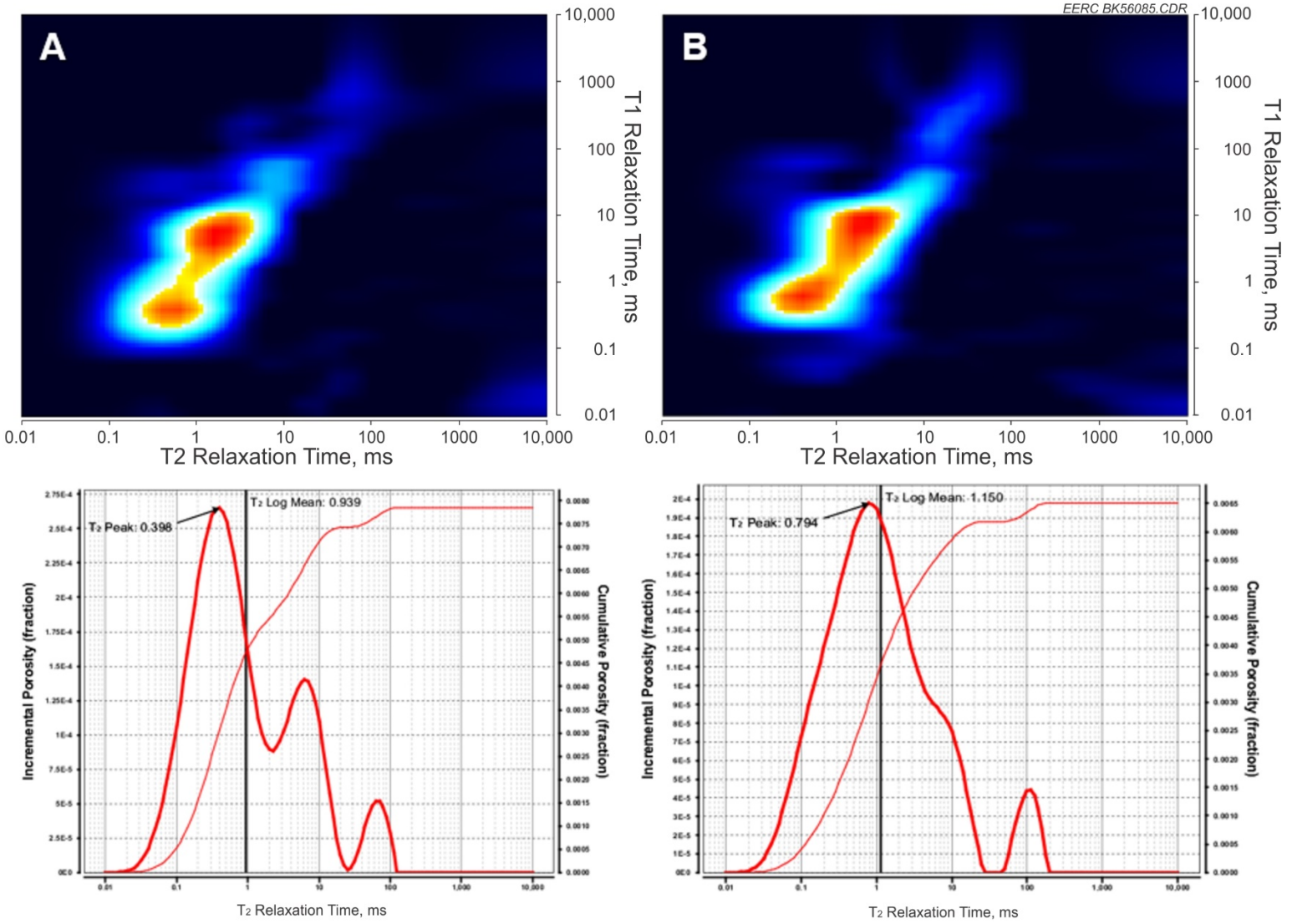

Figure 33. 2-D NMR maps and their corresponding 1-D profiles for Middle Bakken reservoir sample before (A) and after (B) exposure to CO_2.

Results of Sorption Testing

As noted previously, CO_2 isotherm data were generated to determine the potential maximum sorptive potential of the shales and middle siltstone member of the Bakken. Figures 34–36 show the combined results for each of the tests organized by lithofacies.

As shown in Figure 34, the UBS samples group together in a consistent trend. The total adsorptive potential is trending toward 14 mg of CO_2 per gram of rock. The consistency of this result is likely due to the fact that these samples were obtained from a reasonably close geographic proximity. The UBS sample shown in red is the same sample tested for dynamic CO_2 flow through testing. Based on the results of dynamic CO_2 testing, a volumetric difference of 3 mL (2.4 g, 2400 mg) was observed between the injection pump and the receiver pump, suggesting that approximately 2400 mg of CO_2 was retained in the sample. When compared to the CO_2 isotherm data (14 mg/g), the total sorptive potential for the sample is approximately 550 mg. The total pore volume of the sample was determined to be 1.5 mL. Using a CO_2 density of 0.808 g/mL, approximately 1200 mg of CO_2 could occupy this volume of pore space. Combining the mass of CO_2 sorbed with that which could be stored as a free phase in the pore space results in a theoretical CO_2 retention potential of 1765 mg. The results of the dynamic testing suggest that 600 mg of CO_2 more than the theoretical retention mass was retained in the sample. However, this may be explained by uncertainty in estimating the total porosity and pore volume of these tight rocks and a potentially increasing pore volume due to the extraction of hydrocarbons with CO_2.

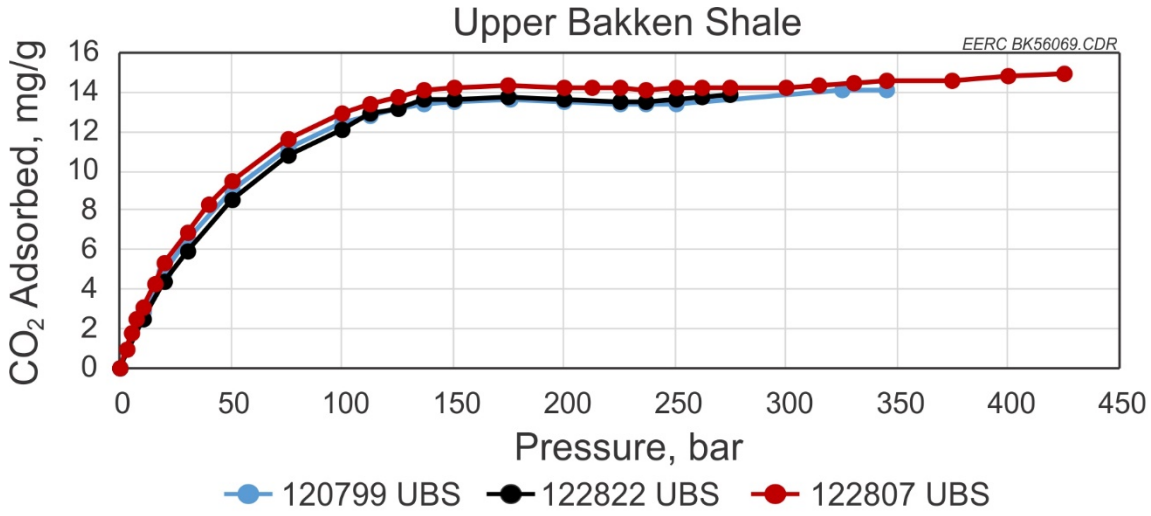

Figure 34. Plots of three UBS samples demonstrating a consistent trend of adsorptive capacity at near reservoir pressure and temperature conditions. These wells are in close geographic proximity. The sample in red is from the same well sampled and tested for CO_2 flow-through potential.

Figure 35 shows the results for the LBS sample set. In this data set, differences in thermal maturity and the potential for adsorption become evident. The sample shown in blue with comparatively low adsorptive capacity is taken from the least thermally mature, northern portion of the basin. In contrast, the curves shown in red and black are from two locations considered to have high production potential. Rock Eval data provide TOC and Tmax data for each sample in Figure 13 with 120818 at 13 wt% and 450°C, 122839 at 11 wt% and 457°C, and 122846 at 5 wt% and 424°C. These attributes are likely the key contributor for the low adsorptive capacity and provide insight regarding the storage potential in straight clay-rich shale lithologies compared to organic-rich shales. Regarding the dynamic flow-through tests, a volumetric difference of 0.7 mL (0.57 g, 570 mg) was observed. Using an estimated pore volume of 0.36 mL, a maximum of approximately 291 mg of CO_2 can fill this space. Given a measured sorption potential of 15 mg of CO_2 per gram of rock, the combined free-phase storage and sorption of CO_2 could be as high as 500 mg. This result is reasonably close to the observed pump difference of 570 mg.

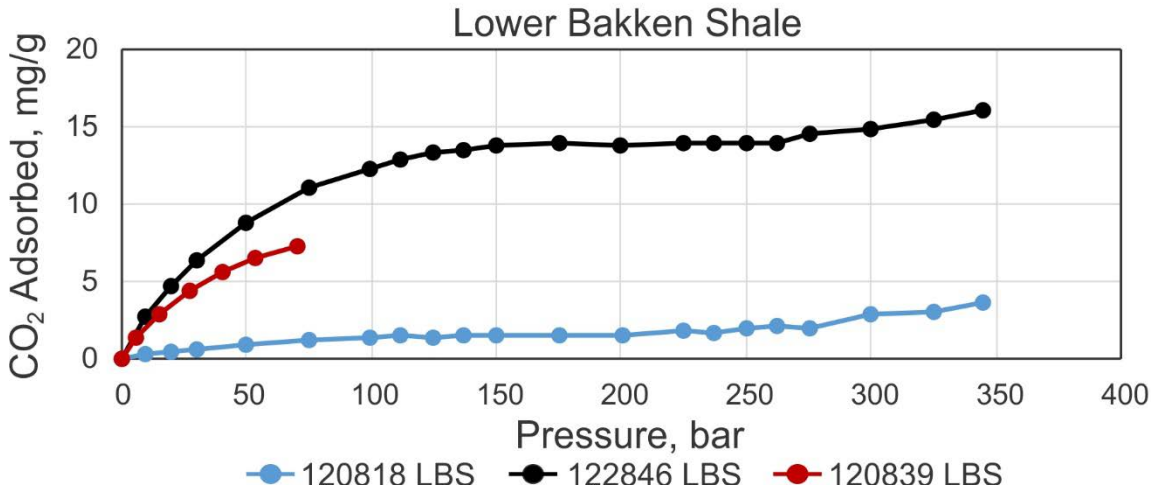

Figure 35. Results of adsorption isotherm testing for LBS samples. The spread on these curves is likely the result of thermal maturity differences between the samples tested. The sample in red was used for CO_2 flow-through testing discussed previously.

As noted previously, the Middle Bakken is known to contain very little organic content aside from the hydrocarbons that migrated from the Bakken shale source rocks into the unit. However, the adsorptive capacity of this interval is of interest due to the comparatively porous and permeable character it exhibits in contrast to the bounding shales, plus the fact that SEM imagery of Middle Bakken rocks shows that many of the pores are lined or filled with clay. Figure 36 shows the results of adsorption tests for the Middle Member. It should be reiterated that the samples tested here are taken from the siltstone interval considered the primary drilling and completion target. Additional tests will need to be performed to determine the overall performance of the additional lithofacies comprising the Middle Member.

The curves presented in Figure 36 demonstrate the low adsorptive potential for the MB siltstone. The red curve represents the sample tested for dynamic CO_2 flow-through tests. Based on the average isotherm data, approximately 1.2 mg CO_2 per gram of rock could be adsorbed per gram of sample. Considering the mass of the sample is 42.7 g, the resulting potential is approximately 51 mg of CO_2. The dynamic flow-through test results showed a volumetric difference of 1.6 mL or 1.3 grams between the injection and receiver pumps. With a starting sample pore volume of 0.84 mL available and assuming that all of this pore space becomes saturated with CO_2, the free-phase storage potential is 679 mg. When combined with the CO_2 sorption estimate, the combined CO_2 retention potential could be as high as 730 mg. While there is a considerable difference from the dynamic flow through test (1250 mg), the question of in-place fluids and their mobilization during testing must be considered. If the in-place fluids are mobilized and produced from the sample, it is likely that CO_2 is replacing this pore volume over the course of testing and may provide insight regarding the diverging curves shown during the test (Figures 30 and 31).

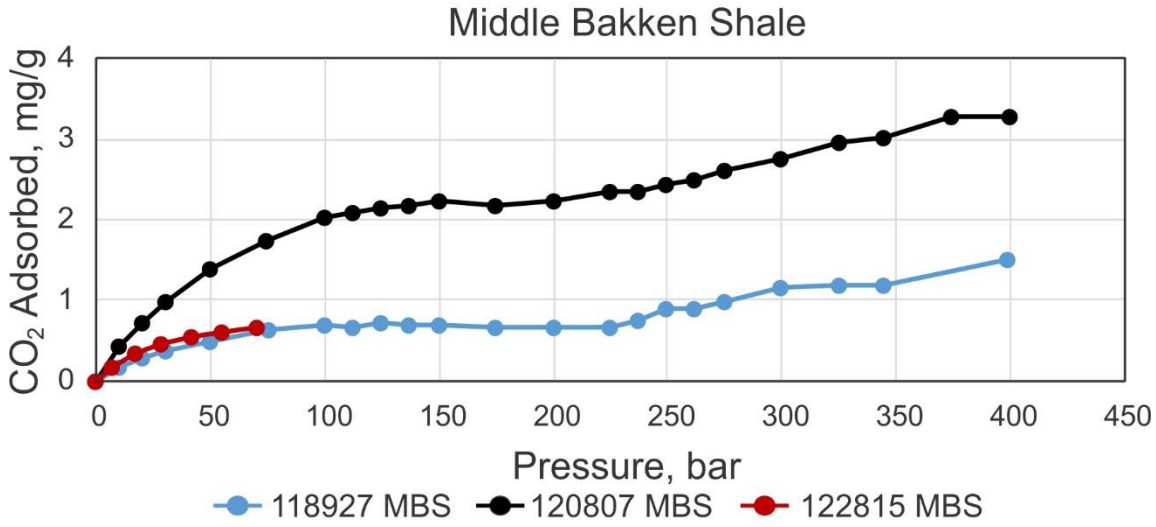

Figure 36. Middle Bakken siltstone samples were tested to determine the adsorptive potential in clastic rocks known to have low TOC content. The red curve is the sample used during CO_2 flow-through testing.

During each of the dynamic flow-through tests, the injected volume was higher than the volume received. While additional testing is needed to further validate these observations, the consistency of the results demonstrates the potential for CO_2 storage in organic-rich shales and clay-rich siltstones. Furthermore, each of the samples was permeated by CO_2 from the inlet to the outlet of the core sample. Mechanistically, the question remains whether this permeation is through diffusion, capillary flow, or a combination of the two. The authors of this study believe that a combination of diffusion and capillary flow are the likely mechanisms, with the OM within the shales providing the most likely pathways for fluid flow. Within the siltstone sample, CO_2 flow is likely contained to available connected porosity, and CO_2 trapping occurs onto clay particles lining the pores. While the sample plugs evaluated in the flow-through testing were not

the exact same samples used for the isotherm sorption testing, the sorption test data combined with the results of the dynamic flow-through tests can be used to estimate the sorptive capacity of samples from similar lithofacies. Table 4 shows a summary of the potential for CO_2 storage based on the experimental data. To arrive at these values, the following assumptions were made: 1) all of the available pore volume is filled with free-phase CO_2 and 2) the isotherm data are considered CO_2 sorbed onto the organics and clays within the matrix.

Table 4. Summary of Results Comparing the Dynamic Flow-Through Test Results with the CO_2 Adsorption Isotherm Testing

		UBS	LBS	MB
Oven Temperature, °F		160	160	160
Pressure, psi		4800	4800	4800
Pore Volume, mL		1.537	0.358	0.837
Mass of Rock, g		39.5	13.7	42.7
Observed CO_2 Volume Difference Between Inlet and Outlet, mL		3	0.7	1.56
Density of CO_2 (g/mL) at 160°F and 4800 psi	0.80836			
CO_2 Mass Difference Between Inlet and Outlet, g		2.425	0.566	1.262
CO_2 Mass Difference Between Inlet and Outlet, mg		2425	566	1262
Free-Phase CO_2 Stored PV * CO_2 ρ, mg		1212	291	679
Potential Sorbed CO_2 (isotherm potential), mg		553	205	51.4
Total Stored During Experiment, mg		1765	496	730

Results of NETL Flow-Through Testing

Several experiments were conducted by the NETL's CT scanning laboratory in Morgantown with the aim to evaluate the potential effects of CO_2 on organic-rich Bakken shales. Specifically, the NETL's flow-through system coupled with CT imaging capabilities was used to investigate potential changes in sample permeability and/or fracture and pore networks during dynamic CO_2 exposure tests. To complement these experiments, the EERC conducted FESEM analysis of the samples pre- and post-CO_2 exposure to determine whether any geochemical changes occurred to the minerals in the samples.

Five different experiments were conducted on Bakken shale core samples. Two of the tests utilized helium and xenon as the injection fluid, and the last three tests used CO_2 as the working fluid. The CO_2 tests were performed on an unfractured brine-saturated sample, a fractured brine-saturated sample, and a sample that had existing fractures in the as-received state. The results indicate that an attempt to inject helium into an unfractured Bakken shale sample that was saturated with brine yielded no observable flow after 24 hr with a differential pressure of about 400 psi. Similarly, an attempt to flow xenon in an unfractured, brine-saturated sample resulted in no observable flow after about 1 month in the flow-through system. The first CO_2 test was performed on a brine-saturated shale sample that had no microfractures. There was no observable CO_2 flow in this test; however, it is worth noting that the fluid pressures used in the NETL test were much less than the fluid pressures used in the EERC tests (1600–1200 psi vs. 5000–

4600 psi, respectively) which could explain the lack of fluid flow in the NETL results. Because the results of these tests showed no flow to the various gases within the test durations, it was impossible to determine changes in flow patterns due to CO_2 exposure.

Controlled induced fractures were created in another organic-rich shale core sample, and the flow-through test was conducted to investigate potential swelling of OM in the sample. While there was quick breakthrough of CO_2 through the sample because the fractures were propped with quartz sand, a determination of the swelling characteristics and/or any potential mineralogical changes was impeded because of sample contamination due to a ruptured heat-transfer fluid jacket during depressurization at the end of the test.

The last flow-through test was performed on an as-received sample with existing fractures and yielded some promising results. Figure 37 shows steady-state periods between refills of volumetric flow rates obtained during testing of the as-received sample with natural fractures. The negative slopes of the fitted line through the data indicate a general decreasing trend in CO_2 flow rates at the injection and receiver pumps. Given that the pressure drop across the core was kept constant at 400 psi, the negative flow rate slopes suggest a decreasing trend in transmissivity with increasing CO_2 exposure time as illustrated in Figure 38. Although the slopes are not consistent, the data illustrate an overall downward trend in transmissivity.

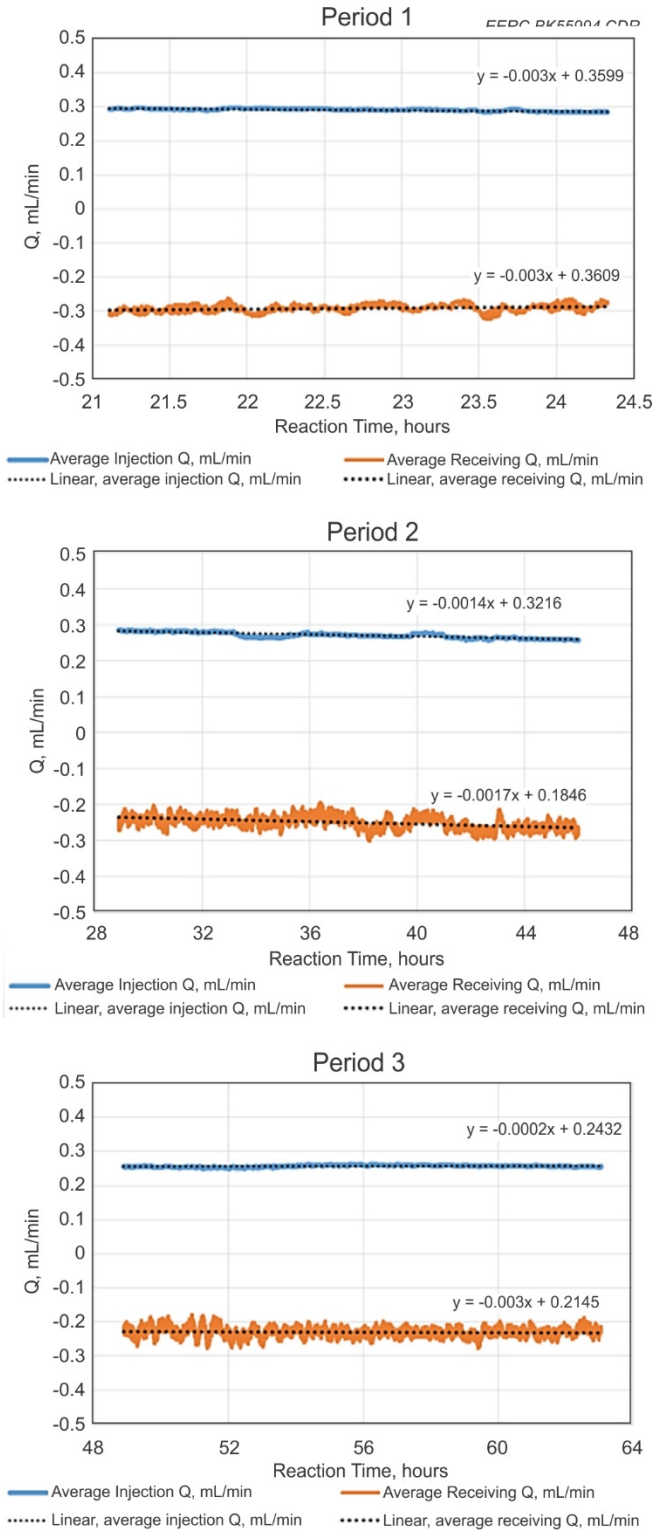

Figure 37. Steady-state periods of volumetric flow rates during testing of the as-received sample with natural fractures.

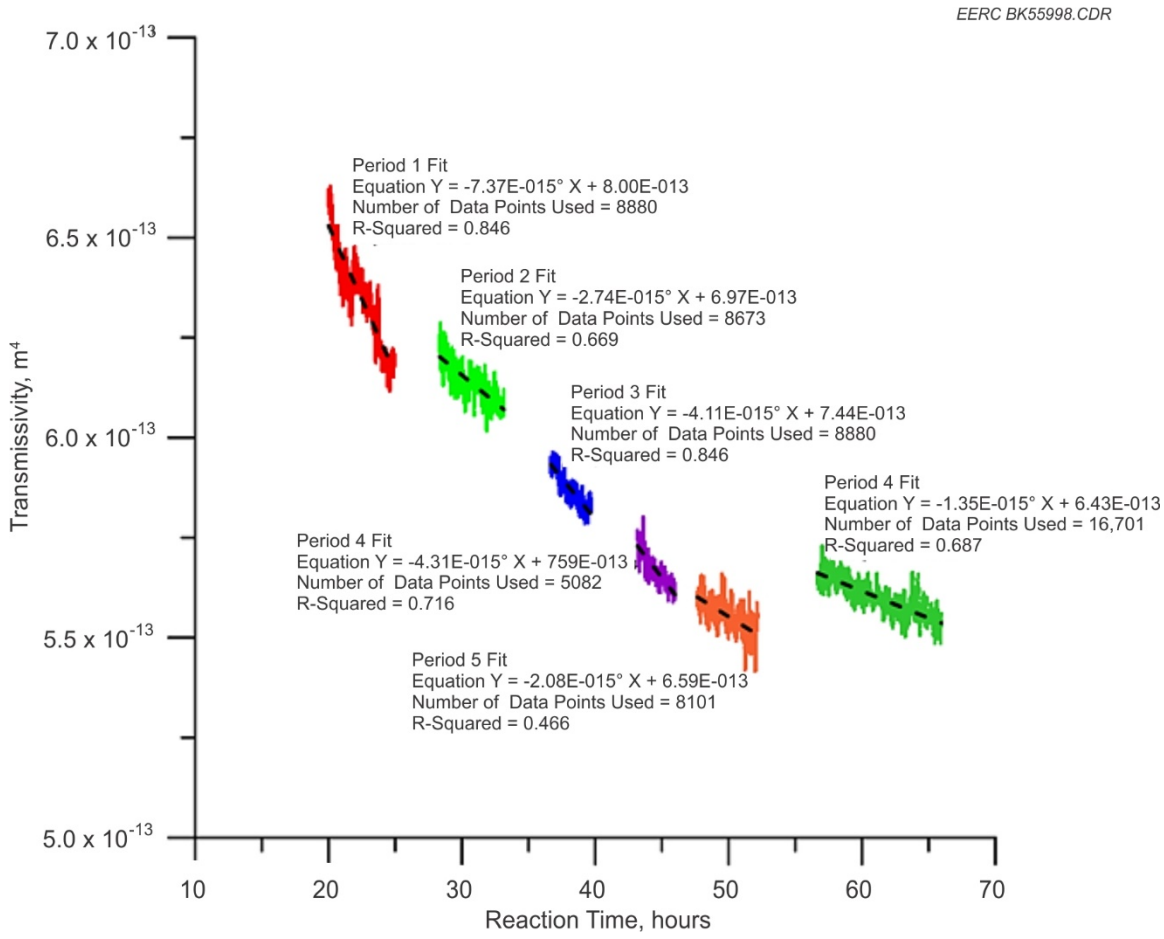

Figure 38. General trend in transmissivity with CO_2 exposure time.

FESEM Analysis of the As-Received Sample Before and after CO_2 Exposure

Figures 39–42 show representative FESEM images obtained on the inlet and outlet faces of the core before and after CO_2 flow-through testing. Although the images were not taken on the same spot on the sample pre- and posttest, they still provide a general overview of any major differences or changes that may or may not have occurred during testing. The images in Figures 39 and 41 show that the inlet and outlet faces of the core contain expected Bakken shale mineralogy and textures, with OM, pyrite, and occasional calcite grains all in the silty matrix of clays containing silt-size quartz, feldspars, and dolomite grains. The OM particle inclusions in Figure 39 show microfractures that are known to be common in the Bakken Formation shales as discussed earlier.

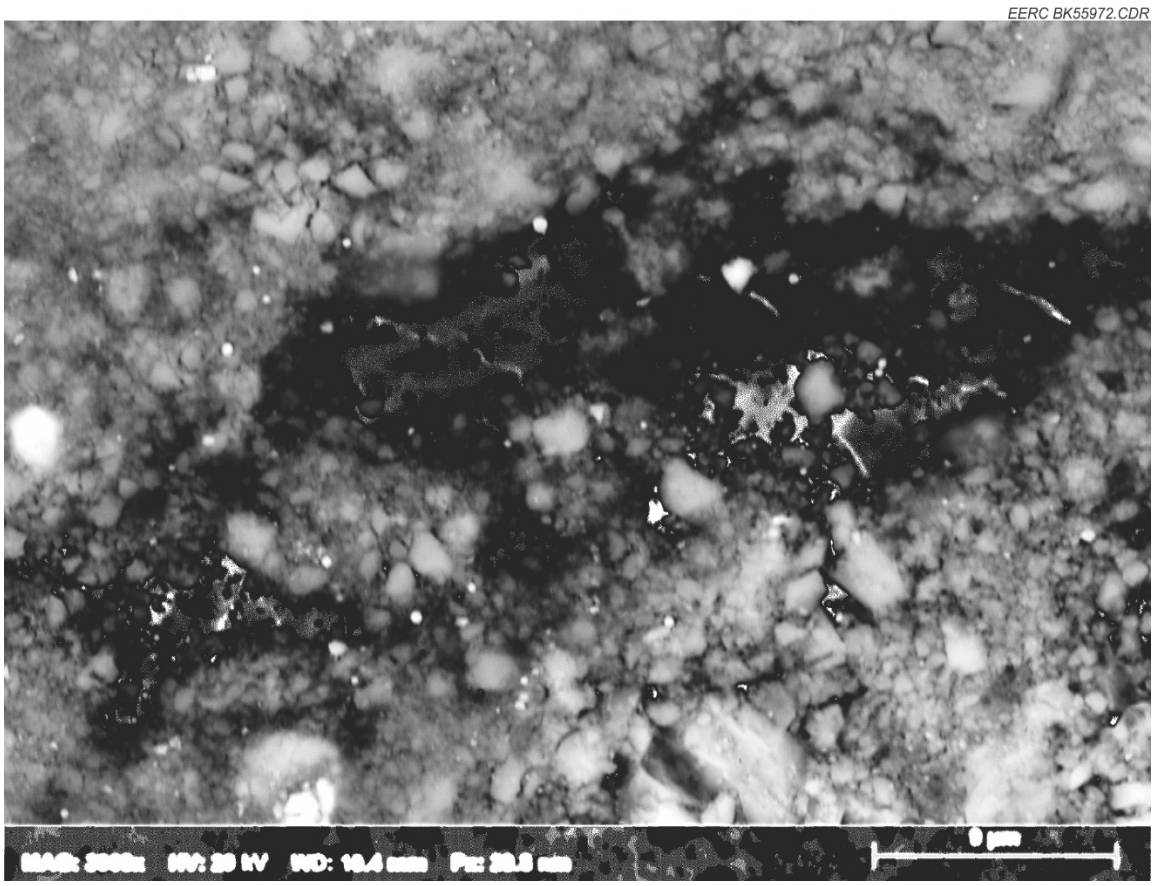

Figure 39. FESEM image of the inlet face of a LBS core before CO_2 exposure.

After exposure, FESEM analysis revealed that some geochemical events occurred. It should be noted that this sample was an as-received sample, which means it had only residual fluids and the liquid CO_2 exposed to it. The inlet face of the sample after CO_2 exposure showed precipitated grains of halite, calcite, calcium sulfate, iron oxide and, potentially, iron chloride.

There were also residues that contained other metals like chromium and nickel compounds that are believed to be steel corrosion products from flow-through system components. Figure 40 Images A, B, and C show various textures of iron oxide that precipitated during CO_2 exposure; Image D shows needlelike calcium sulfate crystals; Image E shows needlelike crystals of calcium aluminosilicate (which are not common in natural Bakken shales); and Image F shows mobilized OM, presumably hydrocarbons. The formation of calcium aluminosilicate suggests breakdown of minerals such as calcite, clays, or feldspar and reformation of the aluminosilicates under the exposure conditions. Analysis of the outlet face yielded results, shown in Figure 42, that were similar to those obtained from the inlet face of the core, with Images A and B being a display of different calcite textures. The flat faces on the calcite and calcium sulfate grains of Image A are restrictions to crystal growth due to flow-through system housing assembly. Like in the case of the inlet face, steel corrosion products (e.g., Cr, Ni, and Zn compounds) possibly coming from flow through system equipment were also noted.

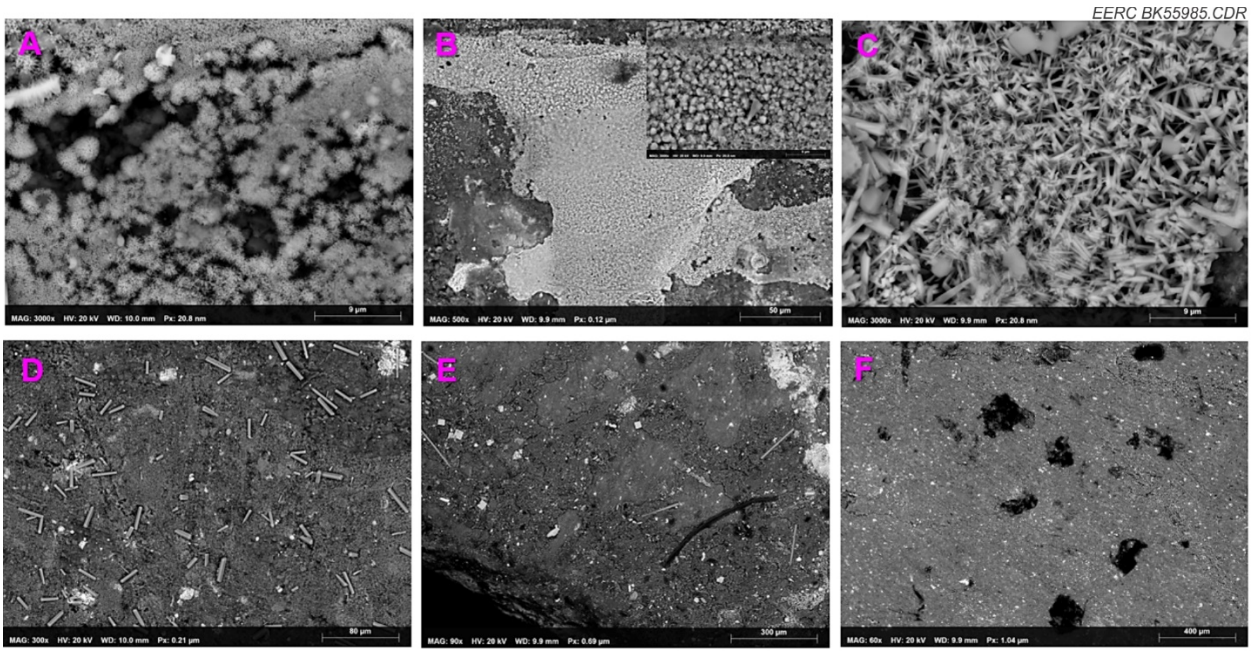

Figure 40. FESEM images of the inlet face of a LBS core after CO_2 exposure. Images A–C show various textures of precipitated iron oxide; Image D shows needlelike crystals of calcium sulfate; Image E shows needlelike crystals of calcium aluminosilicate; and Image F shows mobilized OM as dark spots on the surface.

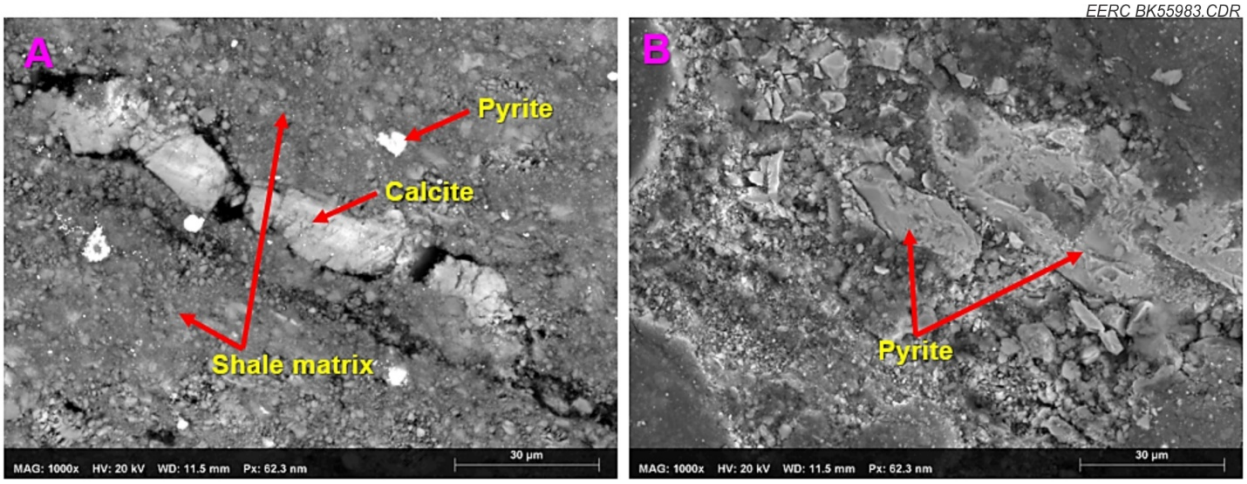

Figure 41. FESEM image of the outlet face of a LBS core before CO_2 exposure.

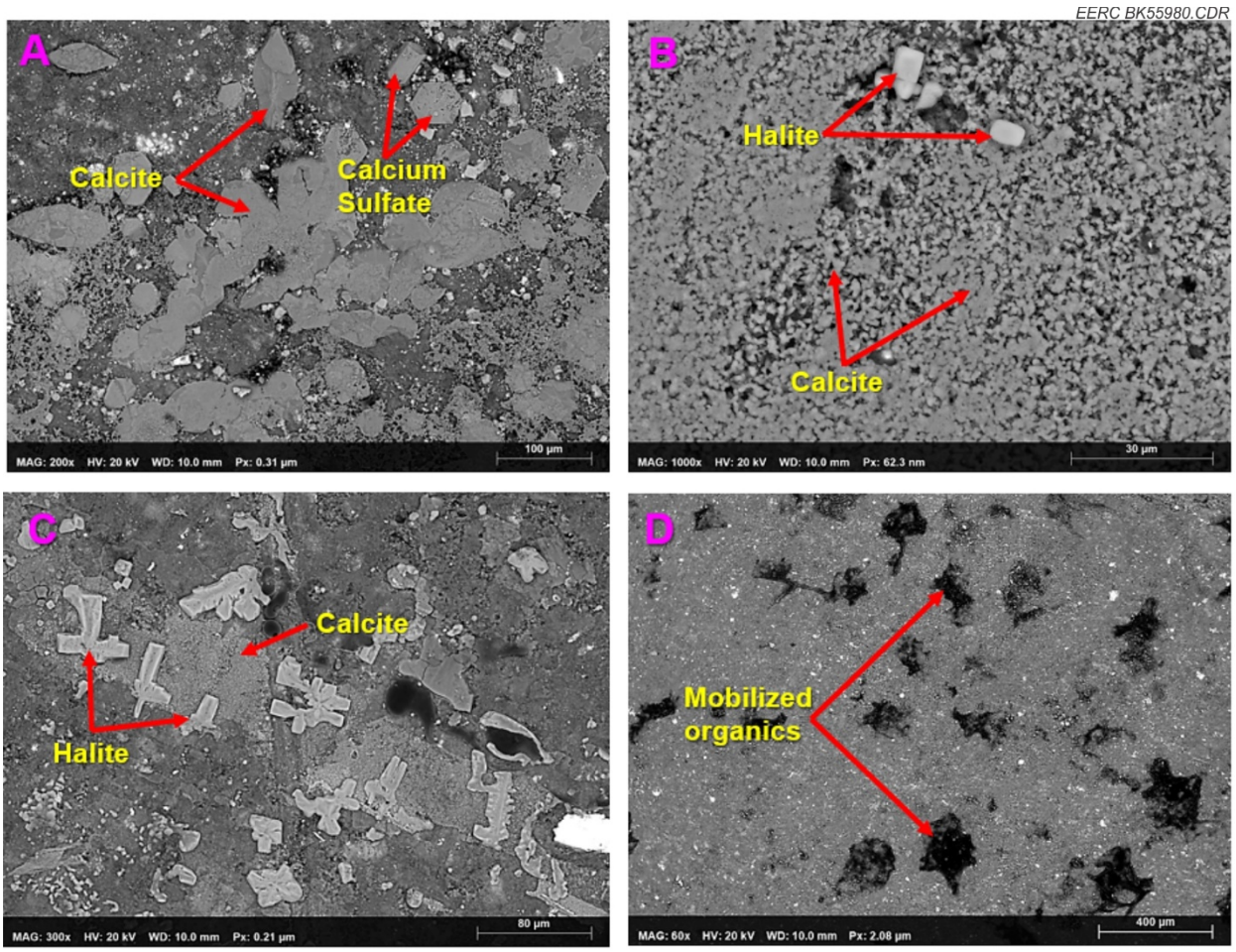

Figure 42. FESEM images of the outlet face of a LBS core after CO_2 exposure. Images A and B illustrate different calcite textures; Image C shows halite and calcite precipitates; and Image D shows hydrocarbons that were mobilized during CO_2 exposure.

CONCLUSIONS

Previous work conducted by the EERC (Kurz and others, 2018; Sorensen and others, 2018) has highlighted the importance of better understanding the porosity, fracture networks, OM, and mineral content of organic-rich shales and other unconventional formations to fully understand their potential as a CO_2 storage resource. Past EERC efforts (Hawthorne and others,2013 and 2014; Kurz and others, 2018) have also demonstrated that CO_2 is able to penetrate and extract oil from organic-rich shales efficiently and much faster than would be expected within low porosity, low permeability samples. The primary mechanism of CO_2 transport within the Bakken shales is thought to be through OM-associated fracture networks and porosity (Kurz and others, 2018), which implies that CO_2 is able to access material within the shales that has a high sorptive capacity for CO_2. The results of this work provide a method to quantify the relationships between flow pathways in very fine-grained rocks and the mineral or OM components that control CO_2 sorption. While this work focused on better understanding and quantifying the sorptive sample components (clays and OM) and their occurrence with respect to potential flow pathways (pores

and fractures), this approach can also be used to quantify the occurrence of reactive minerals, such as carbonates or feldspars, that CO_2 could contact upon permeation through the samples.

A summary of the key outcomes of this work include the following:

- The AMICS software developed in collaboration with Hitachi High Technologies was highly useful for advanced mineralogical characterization of fine-grain, unconventional formations, including organic-rich shales. The FESEM capabilities coupled with the AMICS software allowed for excellent detection, resolution, and classification of the key components of interest (OM, clays, fractures and porosity) for this effort, including detection of nanoscale porosity within OM.

- AIA methods developed using Ilastik were used to differentiate and quantify void space within pores versus fractures and to identify the sample components that were adjacent to potential flow pathways (pore spaces and fractures). These data, together with the shared border analysis approach, were used to develop efficiency factors associated with CO_2 sorption on clays and OM, which were used to expand the volumetric CO_2 resource equation to better differentiate sorption on clays versus OM.

- Flow-through testing of Bakken shale and nonshale core plugs illustrated the difference in flow behavior and CO_2 retention as a function of fractured versus unfractured rocks. The unfractured LBS sample exhibited flow behavior that was indicative of a period of CO_2 retention/sorption in the sample prior to breakthrough (as indicated by an increase in flow rate); the flow rate in the samples that contained microfractures showed little variation and followed a linear pattern throughout the duration of the test. Flow-through testing of a naturally fractured Bakken shale sample by NETL suggested a small decrease in flow rate over time which may have been indicative of swelling or other geochemical changes occurring along the flow pathways over time.

- Sorption testing of Bakken shale and nonshale samples revealed that the Bakken shales have approximately 10 times the CO_2 sorptive capacity than the nonshale reservoir rocks. This is likely due to the high OM and clay mineral content of the Bakken shales. The nonshale reservoir unit typically contains a lower clay content than the shales and very low, if any, OM. For example, based on the samples analyzed through this effort, the clay mineral content is about 35 wt% and 42 wt% for the UBS and LBS units, respectively, while the Middle Member contains only about 10 wt%. The smaller amount of CO_2 sorption observed in the nonshale Bakken reservoir rocks was likely a result of CO_2 interaction with clay minerals that line the pore spaces.

FUTURE WORK

The work performed through this effort represented only a small portion of the potential research that could be performed on organic-rich shales by applying image analysis and machine learning techniques to better understand potential gas and fluid migration pathways and the sorption potential of the rocks based on mineralogical and/or OM content. For example, future

work could be performed to better understand the number of images needed to use stereological approaches to estimate the volume of sample components using 2-D and 3-D imagery. Also, while image analysis techniques were successfully developed to better identify and quantify the void space in organic matter and to differentiate between void space in pores versus fractures, additional work is needed in that area to determine connected versus nonconnected porosity. Being able to derive this information would facilitate scaling up of the sample characterization data from the nano- and microscale to the core scale, well scale and, eventually, to the reservoir scale using log data, petrophysical analysis, and advanced mathematical techniques, including fractal analysis. This information would help facilitate and improve the accuracy of reservoir modeling and simulation to estimate the CO_2 storage resource potential of tight formations.

The modified storage resource equation developed by the EERC also expanded the porosity term to account for reservoir fluid displacement efficiency; however, the methods developed through this effort were not focused on calculating those parameters. Additional work, either through laboratory testing or reservoir modeling and simulation, is needed to better understand reservoir fluid displacement efficiencies in organic-rich shales and other tight formations.

Additional work is also needed to determine the sorptive capacity of the individual sample components (OM and clay minerals) at reservoir conditions. A better understanding of the sorption capacity of each component coupled with the image analysis approach developed through this effort would allow for improved estimation of the Bakken CO_2 storage resource. Evaluation of the sorptive potential of OM as a function of thermal maturity would also lend insight into the potential CO_2 storage resource of different organic-rich shales. While this effort focused on samples from the Bakken, this workflow could easily be applied to other shales and unconventional reservoirs to estimate the CO_2 storage resource potential.

MILESTONES

The completed milestone table can be found in Table 5.

Table 5. Milestones

Milestone Title/ Description	Planned Completion Date	Actual Completion Date	Verification Methods	Comments
M1 – Project Kickoff Meeting Held	7/31/16	7/7/16	Presentation file submitted to DOE.	Held via WebEx.
M2 – Installation of the FESEM, Training and Verification Testing	10/31/16	10/31/16	Reported in subsequent quarterly report.	Reported in October–December 2016 quarterly report.
M3 – Validation of Mineralogical Predictions Using AMICS	9/30/17	9/30/17	Reported in subsequent quarterly report.	Reported in July–September 2017 quarterly report.
M4 – Completion of Core Testing Conducted at NETL's CT Scanning Laboratory	6/30/18	6/30/18	Reported in subsequent quarterly report.	Reported in July–September 2018 quarterly report.
M5 – Completion and Validation of an Image Analysis-Based Method to Characterize Porosity in Tight Rocks	4/30/18	4/30/18	Reported in subsequent quarterly report.	Reported in July–September 2018 quarterly report.
M6 – Completion of Methods Development to Improve CO_2 Storage Resource Estimates in Unconventional Formations	8/31/18	8/31/18	Reported in subsequent quarterly report.	Reported in October–December 2018 quarterly report.
M7 – Completion of Journal Article	2/28/19	2/28/19	Provision of journal manuscript to DOE NETL for review.	Document submitted to DOE for review.
M8 – Completion of CO_2 Sorption Testing in Bakken Shales	8/31/18	8/31/18	Reported in subsequent quarterly report.	Reported in October–December 2018 quarterly report.

REFERENCES

Bousige, C., Ghimbeu, C.M., Vix-Guterl, C., Pomerantz, A.E., Suleimenova, A., Vaughan, G., Garbarino, G., Feygenson, M., Wildgruber, C., Ulm1, F-J., Pellenq, R. J-M., and Coasne, B., 2016, Realistic molecular model of kerogen's nanostructure: Nature Materials, February 2016, DOI: 10.1038/NMAT4541.

Bruker, 2019, High speed differentiation of mineral phases of similar BSE intensity with AMICS, Application Note # EDS-16: www.bruker.com/products/x-ray-diffraction-and-elemental-analysis/eds-wds-ebsd-sem-micro-xrf-and-sem-micro-ct/quantax-eds-for-sem/amics-software.html (accessed February 2019).

Chadwick, R.A., Zweigel, P., Gregersen, U., Kirby, G.A., Holloway, S., and Johannessen, P.N., 2004, Geological reservoir characterization of a CO_2 storage site—the Utsira Sand, Sleipner, northern North Sea: Energy, v. 29, p. 1371–1381.

Das, M., and Medhi, N., 2015, Clay minerals and its importance on hydrocarbon production potential in a part of Geleki oilfield of Upper Assam Basin: International Journal of Research in Engineering & Applied Sciences, v. 5, p. 25–33.

DMR, 2019, Overview of the petroleum geology of the North Dakota Williston Basin: www.dmr.nd.gov/ndgs/resources/ (accessed February 2019).

Duncan, D.C. and Swanson, V.E., 1965, Organic-rich shale of the United States and world land areas: Geological Survey Circular 523, Washington, DC, https://pubs.usgs.gov/circ/1965/0523/report.pdf (accessed January 2019).

Erdman, N., and Drenzek, N., 2013, Integrated preparation and imaging techniques for the microstructural and geochemical characterization of shale by scanning electron microscopy, *in* Camp, W., Diaz, E., and Wawak, B., Eds., Electron microscopy of shale hydrocarbon reservoirs: AAPG Memoir 102, p. 7–14.

Gilicz, A., and Bodi, T., 2012, Measurement of porosity and gas permeability of tight rocks by the pulse decay method. Geosciences and Engineering, v. 1, no. 1, p. 65–74.

GIT – Green Imaging Technologies LithoMetrix™, 2017, www.greenimaging.com/lithometrix/ (accessed January 2017).

Godec, M., Kiperna, G., Petrusak, R., and Oudinot, A., 2013, Assessment of factors influencing CO_2 storage capacity and injectivity in Eastern U.S. gas shales: Energy Procedia, www.elsevier.com/locate/procedia (accessed January 2016).

Goodman, A., Fukai, I., Dilmore, R., Frailey, S., Bromhal, G., Soeder, D., Gorecki, C., Peck, W., Rodosta, T., and Guthrie, G., 2014, Methodology for assessing CO_2 storage potential of organic-rich shale formations: Energy Procedia, v. 63, p. 5178–5184.

Gray, D.H., and Rex, R.W., 1966, Formation damage in sandstones caused by clay dispersion and migration: Clays and Clay Minerals, v. 14, no. 1, p. 355–366.

Gundersen, H.J.G. and Jensen, E.B., 1987, The efficiency of systematic sampling in stereology and its prediction: J. Microsc, v. 147, p. 229–263.

Hamling, J.A., Gorecki, C.D., Klapperich, R.J., Saini, D., and Steadman, E.N., 2013, Overview of the Bell Creek combined CO_2 storage and CO_2 enhanced oil recovery project: Energy Procedia, v. 37, p. 6402–6411.

Hawthorne, S.B., Gorecki, C.D., Sorensen, J.A., Steadman, E.N., Harju, J.A., and Melzer, S., 2013, Hydrocarbon mobilization mechanisms from Upper, Middle, and Lower Bakken reservoir rocks exposed to CO_2: SPE-167200, *in* SPE Unconventional Resources Conference–Canada, Calgary, Alberts, November 5–7, p. 1–9.

Hawthorne, S.B., Gorecki, C.D., Sorensen, J.A., Miller, D.J., Harju, J.A., and Melzer, S., 2014, Hydrocarbon mobilization mechanisms using CO_2 in an unconventional oil play: Energy Procedia, v. 63, p. 7717–7723.

Howard, C.V., and Reed, M.G., 1998, Unbiased stereology—three dimensional measurement in microscopy: Bios Scientific Publishers, Oxford.

IEAGHG, 2014, CO_2 Storage efficiency in deep saline formations—a comparison of volumetric and dynamic storage resource estimation methods: 2014/09, October 2014.

Kang, S.M., Tathi, E., Abrose, R.J., Akkutlu, I.Y., and Sigal, R.F., 2011, Carbon dioxide storage capacity of organic-rich shales: 2011 Society of Petroleum Engineers Journal, 14 p.

King, G.E., 2010, Thirty years of gas shale fracturing—what have we learned?: Society of Petroleum Engineers, Annual Technical Conference and Exhibition, September 19–22, Florence, Italy, SPE 133456.

Kurz, B.A., Sorensen, J.A., Hawthorne, S.B., Smith, S.A., Sanei, H, Ardakani, O., Walls, J., Jin, L., Butler, S.K., Beddoe, C.J., and Mibeck, B.A.F., 2018, The influence of organics on supercritical CO_2 migration in organic-rich shales: Paper prepared for the Unconventional Resources Technology Conference (URTeC), DOI 10.15530/urtec-2018-2902743.

Kwon, O., Kronenberg, A.K., Gangi, A.F., Johnson, B., and Herbert, B.E., 2004, Permeability of illite-bearing shale: 1—Anisotropy and effects of clay content and loading: Journal of Geophysical Research, v. 109, p. B10205.

LeFever, J.A., 2008, Rock-eval data of the Bakken Formation: NDGS Geologic Investigation 63. www.dmr.nd.gov/ndgs/Publication_List/gi.asp (accessed February 2019).

Levine, J.S., Fukaia, I., Soeder, D.J., Bromhal, G., Dilmore, R.M., Guthrie, G.D., Rodosta, T., Sanguinito, S., Frailey, S., Gorecki, C., Peck, W., and Goodman, A.L., 2016, U.S. DOE NETL methodology for estimating the prospective CO_2 storage resource of shales at the national and regional scale: International Journal of Greenhouse Gas Control, v. 51, p. 81–94.

Mao, G.Z., Liu, C.Y., Zhang, D.D., Qiu, X.W., Wang, J.Q., Liu, B.Q., Liu, J.J., Qu, S.D., Deng, Y., Wang, F., and Zhang, C., 2014, Effects of uranium on hydrocarbon generation of hydrocarbon source rocks with type-III kerogen: Science China: Earth Sciences, v. 57, p. 1168–1179.

Moore, D.M., and Reynolds, Jr., R.C., 1997, X-ray diffraction and the identification and analysis of clay minerals, 2nd ed.: Oxford University Press, New York.

National Institute of Standards and Technology, 2019, NIST chemistry webbook: https://webbook. nist.gov/cgi/fluid.cgi?T=160&PLow=3000&PHigh=5000&PInc=20&Applet=on&Digits=5&ID=C124389&Action=Load&Type=IsoTherm&TUnit=F&PUnit=psia&DUnit=g%2Fml&HUnit=kJ%2Fmol&WUnit=m%2Fs&VisUnit=cP&STUnit=N%2Fm&RefState=DEF (accessed February 2019).

Neuzil, C.E., Cooley, C., Silliman, S.E., Bredehoeft, J.D., and Hsieh, P.A., 1981, A transient laboratory method for determining the hydraulic properties of ‘tight’ rocks II. Application.

International Journal of Rock Mechanics and Mining Sciences and Geomechanics Abstracts, v. 18, p. 253–258.

Oxford Instruments, 2017, NMR and core analysis–technical datasheet: www.oxford-instruments.com/products/analysers/stationary-benchtop-analyser/core-analyser-geospec2plus (accessed January 2017).

Preston, C., Moneab, M., Jazrawib, W., Brown, K., Whittakerd, S., Whitee, D., Lawf, D., Chalaturnyk, R., and Rostron, B., 2005, IEA GHG Weyburn CO_2 monitoring and storage project: Fuel Processing Technology, v. 86, p. 1547–1568.

Rasband, W.S., 2016, ImageJ: U.S. National Institutes of Health, Bethesda, Maryland, USA, https://imagej.nih.gov/ij/, 1997–2016.

Schindelin, J., Arganda-Carreras, I., Frise, E., Kaynig, V., Longair, M., Pietzsch, T., Preibisch, S., Rueden, C., Saalfeld, S., Schmid, B., Tinevez, J-Y., White, D.J., Hartenstein, V., Eliceiri, K., Tomancak, P., and Cardona, A., 2012, Fiji: an open-source platform for biological-image analysis: Nature Methods, v. 9, no. 7, p. 676–682.

Sommer, C., Strähle, C., Köthe, U., and Hamprecht, F.A., 2011, Ilastik—interactive learning and segmentation toolkit, *in* Eighth IEEE International Symposium on Biomedical Imaging (ISBI). Proceedings, p. 230–233.

Sorensen, J.A., Kurz, B.A., Hawthorne, S.B., Jin, L., Smith, S.A., and Azenkeng, A., 2017, Laboratory characterization and modeling to examine CO_2 storage and enhanced oil recovery in an unconventional tight oil formation: Energy Procedia, v. 114, p. 5460–5478.

Sorensen, J.A., Hawthorne, S.B., Jin, L., Bosshart, N.W., Torres, J.A., Azzolina, N.A., Kurz, B.A., Smith, S.A., Jacobson, L.L., Doll, T.E., Gorecki, C.D., Harju, J.A., and Steadman, E.N., 2018, Bakken CO_2 storage and enhanced oil recovery program – Phase II: Final Report to DOE-NETL, Cooperative Agreement No. DE-FC26-08NT43291.

Span, P., and Wagner, W., 1996, A new equation of state for carbon dioxide covering the fluid region from the triple-point temperature to 1100 K at pressures up to 800 MPa: J. Chem. Ref. Data, v. 25, no. 6, p. 1509–1596.

Torp, T.A., and Gale, J., 2004, Demonstrating storage of CO_2 in geological reservoirs—the Sleipner and SACS projects: Energy, v. 29, p. 1361–1369.

U.S. Department of Energy National Energy Technology Laboratory, 2012, The United States 2012 carbon utilization and storage atlas, fourth edition: www.netl.doe.gov/File%20Library/Research/Coal/carbon-storage/atlasiv/Atlas-IV-2012.pdf (accessed January 2016).

U.S. Department of Energy National Energy Technology Laboratory, 2010, Carbon sequestration atlas of the United States and Canada (3rd ed.).

Watney, W.L., 2016, Horizontal drilling – technology review, current applications, and its future, in developing Kansas' petroleum resources: Kansas Geological Survey, Lawrence, Kansas, www.kgs.ku.edu/PRS/Unger/Watney-KBA-KIOGA--Horizontal_Drilling.pdf (accessed January 2016).

Webster, R.W., 1984, Petroleum source rocks and stratigraphy of the Bakken Formation in North Dakota, *in* Woodward, J., Meissner, F.F., and Clayton, J.L. Eds., Hydrocarbon source rocks of the greater Rocky Mountain region, Denver, Colorado: Rocky Mountain Association of Geologists, p. 57–82.

Weibel, E.R., 1979, Stereological methods, *in* Vol 1 – Practical methods for biological morphometry: Academic Press, London.

APPENDIX A

ANALYTICAL TESTING METHODS

ANALYTICAL TESTING METHODS

ROUTINE ANALYTICAL METHODS

The analytical techniques employed in the project include x-ray fluorescence (XRF) spectroscopy, x-ray diffraction (XRD), field emission scanning electron microscopy (FESEM) coupled with energy-dispersive x-ray spectroscopy (EDS), optical microscopy, and ultraviolet fluorescence microscopy of thin sections and software solutions including advanced mineral identification and characterization system (AMICS) and other advanced image analysis programs. Advance sample polishing for FESEM analysis was achieved using a broad ion beam (BIB) milling system. These techniques are briefly described below.

X-Ray Fluorescence Spectroscopy

XRF spectroscopy was used to obtain information about the bulk chemical composition of the samples, using a wavelength-dispersive (WD) XRF spectrometer (Rigakua ZSX Primus-II). Prior to analysis, the samples were ground to fine powder in a micronizing mill. About 2 g of the powder was mixed with a carbon-based collodion binder using acetone as dispersant fluid. The mixture was dried in an oven at 70°C overnight to expel the acetone, and the remaining sample powder was then pressed into 32-mm pellets for analysis. The quantification of major and minor chemical elements was based on predefined library calibrations that are derived from NIST standard reference materials. The presence of trace elements was investigated using a semiquantitative approach that is implemented in Rigaku's ZSX software.

X-Ray Diffraction

Analysis of the bulk crystalline mineralogy of the samples was performed by XRD methods using a Bruker® D8 Advance XRD spectrometer operated at 40 kV and 40 mA. Two sample preparation procedures were used to prepare samples for conventional XRD bulk powder pack analysis and for analysis of clay assemblages (< 16-µm-size fraction) that were separated from the framework matrix of the samples.

For bulk powder pack analysis, the samples were micronized in a McCrone® micronizing mill with ethanol for 20 minutes and then spun in a centrifuge for 20 minutes at 2000 rpm. The clear supernatant layer was decanted, and the remaining material was dried overnight in an oven at 70°C. After drying, the sample was homogenized in an agar mortar and pestle and then packed into a top-loading sample holder as a random bulk powder pack for analysis. For each sample, data was collected from 2° to 70° 2-theta degrees, with a fixed rate of 0.02° 2-theta every 4 seconds. All resulting traces were analyzed using Bruker's Topas® software.

Clay-size fractions (< 16 µm in particle diameter) were prepared following literature approaches (Glass and Killey, 1987; Hughes and others, 1994; Hughes and Warren, 1989; Moore and Reynolds, 1997) to separate clay minerals from framework grains, which facilitated the analysis of the clay mineral assemblages. Briefly, the samples were crushed in a jaw crusher and heated to near boiling in water. The hot mixture was then mixed with household bleach to

remove residual hydrocarbons, followed by treatment with acetic acid to dissolve out the carbonates. The <16-µm particles were then isolated by gravity settling, and the resultant paste was smeared onto glass slides. The slides were analyzed by XRD after further treatment under three different conditions: 1) air-dried, 2) exposed to ethylene glycol vapor for 24 hr, and 3) heated at 350°C for 1 hr. Like in the case of the bulk powder packs, the clay fractions were scanned from 2° to 34° 2-theta degrees at a fixed rate of 0.02° 2-theta every 4 seconds. The resulting XRD patterns were processed to obtain semiquantitative results using Bruker's Eva® software package.

Optical Microscopy and Ultraviolet Fluorescence Microscopy

Thin sections of the rock samples, about 30 µm thick, were made on glass slides for observation by optical microscopy using a Nikon 50i at the EERC and ultraviolet fluorescence (UVF) microscopy using a Nikon Eclipse 80i fluorescence microscope at the University of North Dakota (UND) School of Biomedical Sciences & Medicine. The samples were stained using traditional blue dye so that available pore spaces would show as blue color in plane polarized light images, which were segmented to characterize and quantify the porosity. For UVF analysis, the samples were additionally stained with Columbia blue dye that fluoresces under UV light and so facilitates characterization of micro- and nanofractures in the sample.

Sample Polishing by Broad Ion Beam Mill

The samples were prepared for FESEM analysis by ion mill polishing using a Hitachi BIB system, IM4000 Plus, which is capable of both cross-section milling and flat milling modes. In the cross-section milling mode, the size of the specimen area milled was maximized by choosing a rotation angle of ±60°. The flat milling mode was rarely used in this project but can provide a polished surface area of about 50 mm^2 by using the maximum beam eccentricity of 5 mm. Eccentricity is a capability that was used to move the ion beam cone from its center by up to 5 mm, thus increasing the size of the polished area.

Field Emission Scanning Electron Microscopy

The samples used in this effort were analyzed using a Hitachi SU5000 FESEM system that is also equipped with Bruker's EDS detector. The FESEM also has a backscatter electron (BSE) detector, secondary electron (SE) detector, and can operate in two modes, including variable pressure (VP) and high-vacuum (HV) modes. The VP mode was used to image polished samples under low-vacuum conditions to mitigate charging, especially when unaltered or uncoated samples were analyzed. For analysis under HV conditions, which was most suitable for EDS analysis, the samples were carbon-coated using a Cressington carbon sputter coater for 5 seconds.

To obtain high-resolution and high-quality images that show crisp morphological features of interest in the samples, proper sample preparation and FESEM imaging conditions were critical. The samples were polished using the BIB system in cross-section milling mode, with a rotation angle of ±60 degrees to maximize the size of the sample area polished to about 2 mm

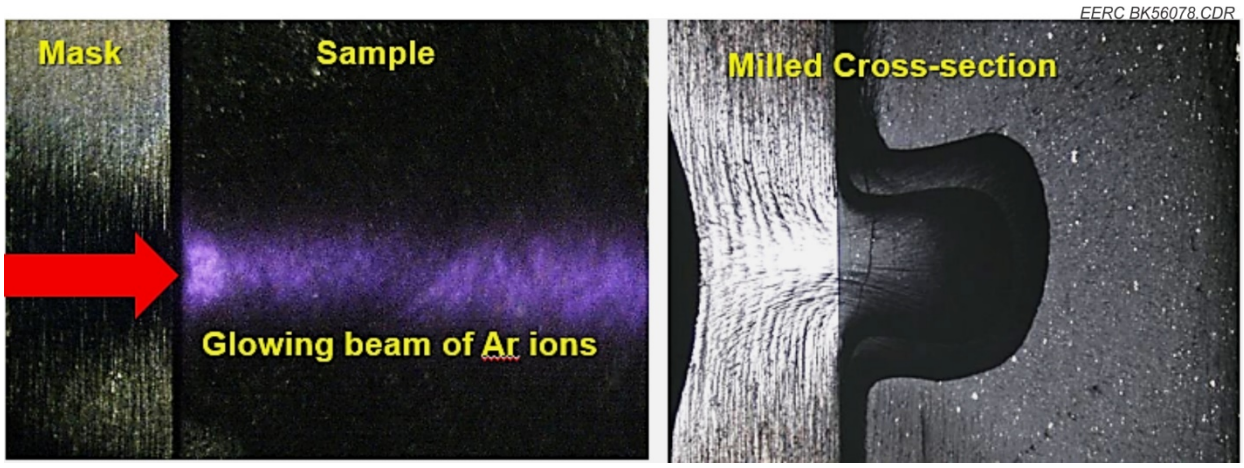

Figure A-1. Illustration of Ar ion mill polishing path (left) and large polished sample cross section (right).

wide by 4 mm deep. Figure A-1 shows a large polished trench on a sample after 10 hr of milling at 5-kV accelerating voltage to achieve a total polished surface area of about 8 mm^2. A large polished sample area was desired to increase the chances of imaging the different features of the rock matrix that represent the sampled interval.

For high-resolution imaging of features of interest, especially organic matter (OM) and clays, the FESEM was operated in VP, low-vacuum mode to mitigate charging. This was especially helpful for imaging unaltered, uncoated sample surfaces to obtain detailed OM and clay textures in the shales. Also by using the VP mode, undesirable effects of masking surface details and textures of clays and OM by a carbon coating layer were avoided. However, for EDS analysis, the samples were then coated with carbon and analyzed under high-vacuum conditions, which is best for collecting x-rays that were used by AMICS software for mineral characterization. Additional FESEM optimal operating parameters included lowering accelerating voltage to 10 kV or less in some cases, while raising beam current to enhance BSE and SE output for crisper images. The FESEM also maintains extreme beam stability, small spot size, and high resolution (about 2 nm even at 30 kV). High resolution and high beam stability were particularly useful for the observation of nanosize features of the rock matrix, especially OM porosity and clay minerals at high magnification.

By using the ultravariable pressure detector (UVD) of the SU5000 system, more fine structural details of uncoated samples were observed in VP mode. The UVD works like an SE detector under VP conditions and is suitable for observing detail surface structural features such as quartz overgrowths (see Figure A-2).

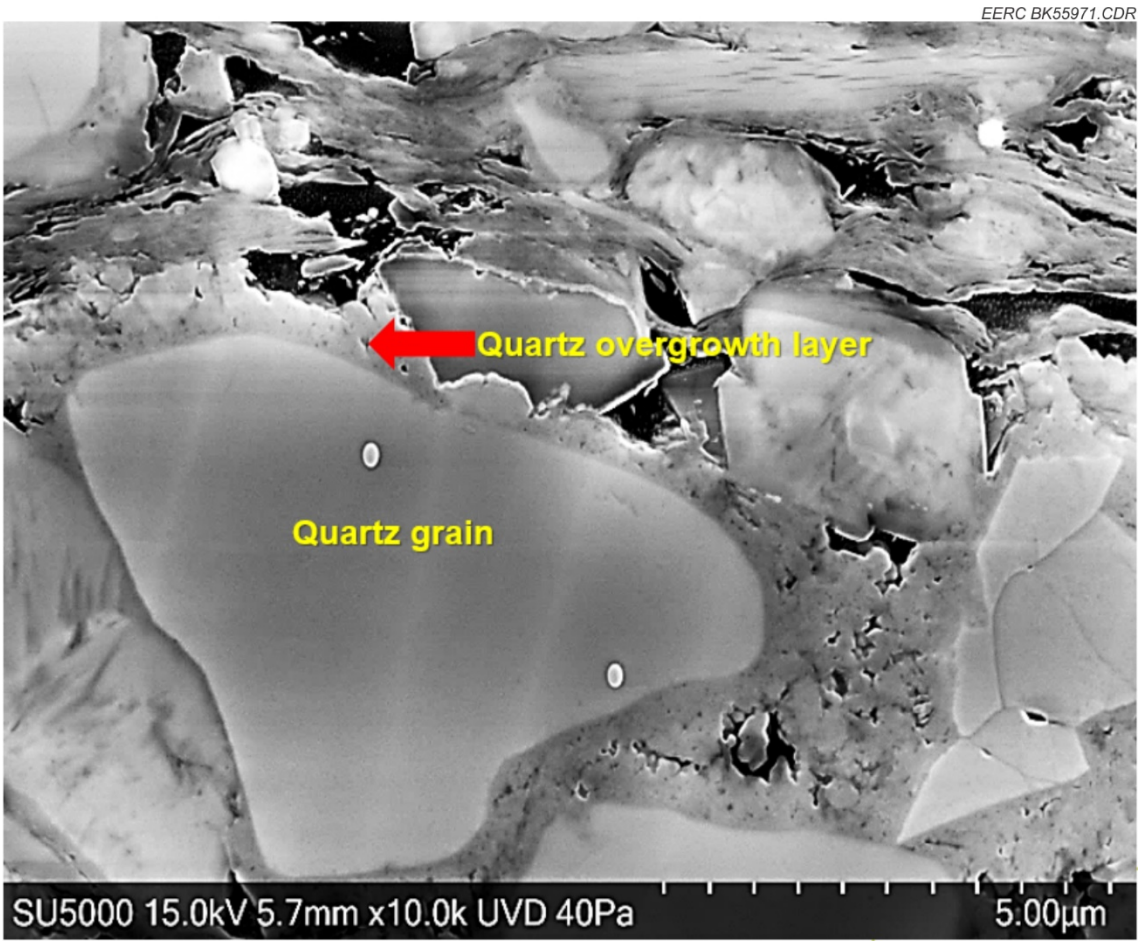

Figure A-2. Image of quartz overgrowths obtained in UVD mode on SU5000 system

NONROUTINE SAMPLE TESTING

Adsorption Test Procedures

Two types of tests were performed to determine the sorptive properties of the organic-rich shales of the Bakken. First, high-pressure, high-temperature adsorption and desorption testing was conducted using a Rubotherm magnetic suspension balance. Second, adsorption isotherms were generated using a more conventional Langmuir-type experiment. Each test procedure is described below.

The "Rubotherm" magnetic balance was used to determine CO_2 sorption isotherms in Middle Bakken and Bakken source shale rock samples at the reservoir temperature of 110°C. The magnetic balance uses a permanent magnet inside the pressure (sample cell) chamber and an electromagnet outside of the chamber which determines the force required to suspend the sample

basket as the CO_2 pressure is increased from near ambient to 5000 psi (Figure A-3). Approximately 6 to 8 grams of crushed rock samples were placed in the sample basket. Each rock sample was pre-extracted with CO_2 to remove crude oil hydrocarbons for 24 hours at 5000 psi and 100°C. Middle Bakken samples were 11-mm-diameter cores ca. 2–3 cm long. Bakken source shale samples were ground and sieved to 1–3.4 mm. These geometries were chosen since previous studies demonstrated that the 24-hour extractions yielded near-quantitative removal of all volatile hydrocarbons that could interfere with the isotherm determinations. One additional sample preparation step was performed after the rock samples were loaded into the magnetic balance chamber, and the chamber was evacuated and heated to remove any adsorbed water from the rock samples. Each test consists of 20 sequential pressure increases followed by 20 pressure decreases. After each pressure change, the balance was left to stabilize (often requiring hours) to allow the mass of adsorbed CO_2 to be accurately determined. The entire process including buoyancy calibrations to adjust the measured weight changes for the changes in CO_2 densities required approximately 2 weeks per sample. Equation A-1 provides the basis for determining the change in mass attained and attributed to adsorbed CO_2 throughout the experiment where Δm^A = adsorbed mass (units), Δm = balance reading (units), m^{sc} = sample chamber mass (units), m^s = sample mass (units), V^{sc} = sample chamber volume (units), V^s = buoyancy measurement (units), and V^A = adsorbate volume (units), $\rho(p,t,y)$ density at test conditions.

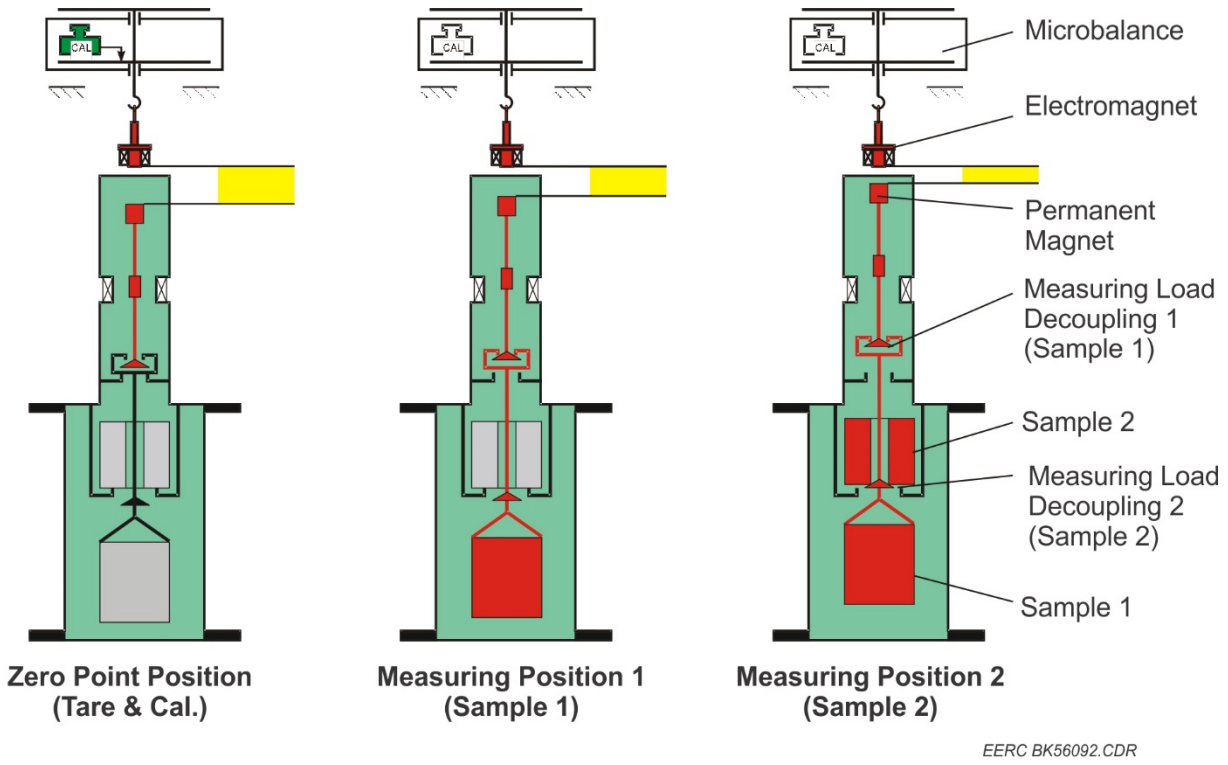

Figure A-3. Schematic diagram illustrating the instrument difference between a conventional microbalance (left) compared to the Rubotherm magnetic suspension balance (right).

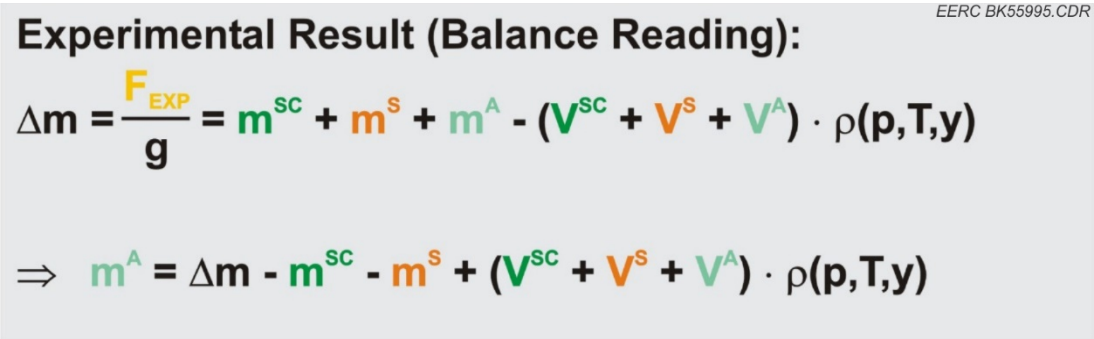

Equation A-1. Calculation used to determine the change in mass based on the force obtained between the two magnets contained in the instrument (taken from Rubotherm).

The following test procedures were used for the lower pressure tests. Prior to testing, samples are crushed to 120-mesh size fractions. One hundred grams of material is set aside for testing and preserved in airtight vials in a darkened space to prevent oxidation. While the apparatus used for testing is capable of testing helium and methane in excess of 175°F and 10,000 psi, this is not the case for gases that have moved into the supercritical phase window. Because CO_2 reaches this phase at a relatively low temperature and pressure (88°F and 1100 psi, respectively), test conditions were performed at a constant temperature of 160°F and a maximum pressure of 5000 psi. At the time of testing, crushed sample material is loaded in a sample holder and weighed to thousandths of a gram. Dead volumes are measured, and gas expansion is considered for the system. Reservoir temperature is maintained constant to 0.01°C throughout the duration of the test. Gas is injected into a reference cylinder of known volume at a predetermined pressure and allowed to expand into the sample container (Figure A-4). Over the test duration, a decrease in system pressure is observed and attributed to gas adsorbing onto the sample material. Each test is repeated six times while increasing the pressure step resulting in a pressure vs. time graph showing the results. Pressure data from testing are analyzed by converting to a volume of gas the sample can store per ton of sample (scf/ton rock). These data are plotted to form the Langmuir curves represented by the isotherm model as:

$$V = P * V_L/(P + P_L) \qquad \text{[Eq. A-2]}$$

Where V is the gas volume adsorbed at pressure P, VL is the maximum sorptive capacity of the material, and PL is the pressure at which the adsorbed gas concentration is one-half of the maximum sorptive capacity. In this interpretation, VL and PL are the Langmuir constants and specific to the sample type used.

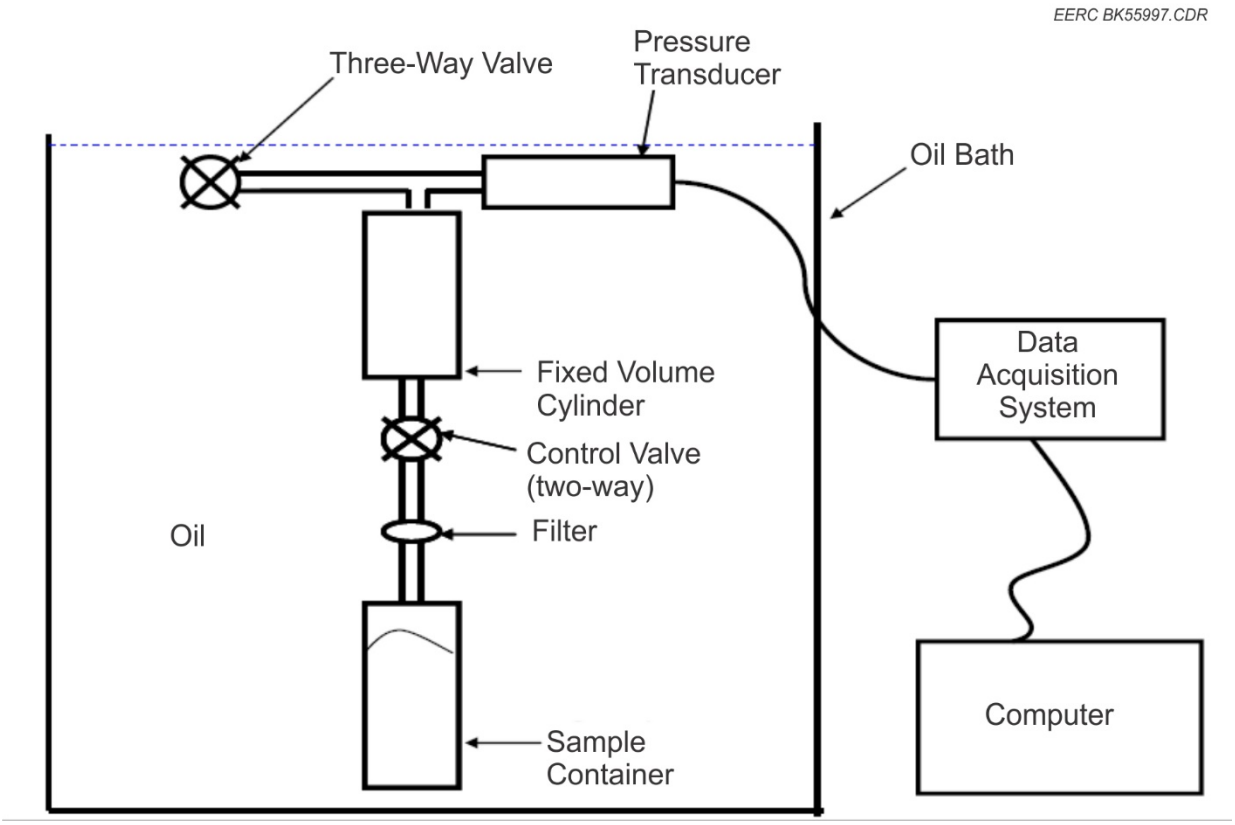

Figure A-4. Test apparatus used for the determination of CO_2 adsorption isotherms.

NMR Analysis

The fundamental principle of NMR as a special core analysis technique is based on the response of hydrogen nuclei to an external magnetic field (Coates and others, 1999; Oxford Instruments, 2015a, 2015b, 2017). Rocks containing hydrogen-rich fluids produce a signal when exposed to a magnetic field, and the signal decays with time after the magnetic field pulse is removed. The time it takes for NMR signals that are transverse to the magnetic field, referred to as T_2 relaxation time, to decay completely is directly related to the pore sizes that bear the fluids (Coates and others, 1999; Oxford Instruments, 2015a, 2017). Hence, the detected NMR signal contains T_2 components from every pore size in the measured rock volume. By using a mathematical process known as inversion, the different components corresponding to different pore sizes can be extracted from the total T_2 NMR signal to form a T_2 distribution. This distribution is generally known as NMR pore-size distribution, which is further processed to derive other petrophysical properties such as total porosity and permeability. In addition, proportions of different fluid types (e.g., mobile and bound fluids or water vs. hydrocarbon) can be determined.

An Oxford Instruments Geospec2 NMR system (Oxford Instruments, 2017), coupled with GIT software, LithoMetrix™ (GIT, 2017), was used for all scans reported herein. Prior to any scan, the NMR instrument was calibrated according to procedures provided by Oxford

Instruments and GIT. The instrument has a modular probe capability, with 29-mm, 53-mm, and 100-mm probe sizes, which are designed to hold 1-inch, 1.5–2-inch, and full-core diameters, respectively. For this study, only the 1-inch probe was used. Once the instrument was calibrated, a standard sample was used to verify proper functioning and accuracy of the results. Prior to analysis, the core samples were cut, and the bulk volumes were measured using calipers and laser scanning techniques at the EERC. The samples were then placed in the probe sample holder and lowered into the instrument. Sample centering was performed to adjust the sample so that it was located in the center of the magnetic field, and the analysis was initiated by setting up the appropriate test scan using the software user interface.

ADVANCED IMAGE ANALYSIS PROCEDURES

Advanced Mineral Characterization by AMICS Software

Figure A-5 shows an overview of the AMICS workflow that was employed to characterize the mineralogy of the Bakken and Marcellus shale samples. The stages include sample polishing using an ion mill system followed by imaging using the SU5000 FESEM system. The AMICS software is interfaced with the FESEM so that the images acquired (and subsequent x-rays) are automatically passed to the software for further processing. Each image frame is then segmented into several thousand segments based on differences in the BSE values, and x-rays are acquired on the segments. The smallest segment for which x-rays were acquired was determined based on the smallest feature of interest in the sample. For the analysis of shales, with very fine textures, the smallest segment area chosen was 0.75 µm. To improve the spatial resolution at a fixed image resolution of 2048 × 1536 pixels, the magnification of the images was set at 1500×. A

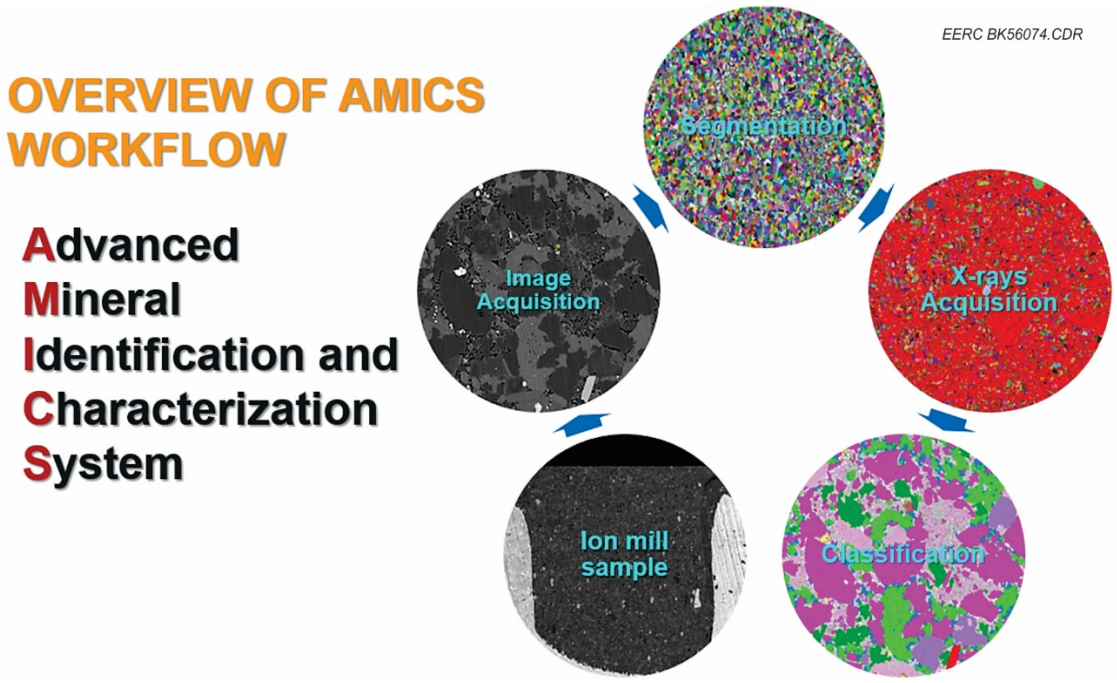

Figure A-5. Illustration of AMICS workflow.

typical frame of size 85 µm × 85 µm, 1500×, 40-nm/pixel resolution yielded about 4.5 million pixels; average of 66,000 segments; about 47,000 x-rays points! Hence, this was a big data process that was also computer memory-intensive, especially when using the AMICS spectrum tree discussed below.

Although a large database of about 2000 minerals was provided by Hitachi for use with the AMICS software, it was necessary to develop custom databases specific to Bakken shales to achieve effective characterization. The database development process involved acquisition of x-rays on the specific mineral in the sample at FESEM conditions suitable for analyzing organic-rich shales. Each spectrum for a given mineral was saved one at a time in the new standard database as it was acquired. The process for generating the custom database was facilitated by searching the available 2000-mineral global database and importing the applicable mineral properties.

A very powerful tool in AMICS that facilitates characterization of organic-rich shales, including OM content, clays, and other major/minor/trace mineral phases, is the spectrum tree. The spectrum tree is a tool by which detailed chemical spectra collected on the sample are used to fine-tune the mineral classification. This is vital for clay and OM delineation in the fine-textured matrix, especially considering the fact that clays and OM often occur as intermixed layers in the Bakken Formation shale matrix. In a typical shale sample, about 1.5 million x-rays were involved in the root cluster of 40 frames, thus requiring a large computer memory allocation for efficient processing. To process 40 frames acquired per sample in this project using the spectrum tree tool, it was necessary to upgrade the existing 8-GB RAM computer to a minimum of about 30 GB of total RAM.

Figure A-6 shows an illustration of the spectrum tree layout. The root cluster is classified based on standard database mineral-phase definitions. The unclassified fraction is then further split based on different criteria such as BSE clusters, energy filters, and x-ray count clusters. Specific clusters that ensue from further splitting are then matched to a mineral phase by searching either the custom, user-defined mineral database or the global mineral database. The process is continued with different criteria until the unclassified fraction reaches an acceptable level, e.g., less 5%, depending on the complexity of the material. In this project, it was demonstrated that the spectrum tree can be used to achieve nearly 100% resolution of the mineral phases in each sample; typically, any unknown or unclassified material was less 1%.

Identification of PAOM Using Feature Masks

To characterize and quantify the porosity associated with OM (PAOM), a process involving creation of specific masks of OM, clay particles, and pores was developed. In addition to obtaining information about pores within the OM particles, clays and nano- to microsize fractures were also identified and quantified. Pores and fractures within OM are important for estimating the total void volume fraction used in developing equations for calculating the CO_2 mass storage resource potential for shale and other tight rock reservoirs. The steps involved in the creation of each feature mask are depicted in Figure A-7 and described below.

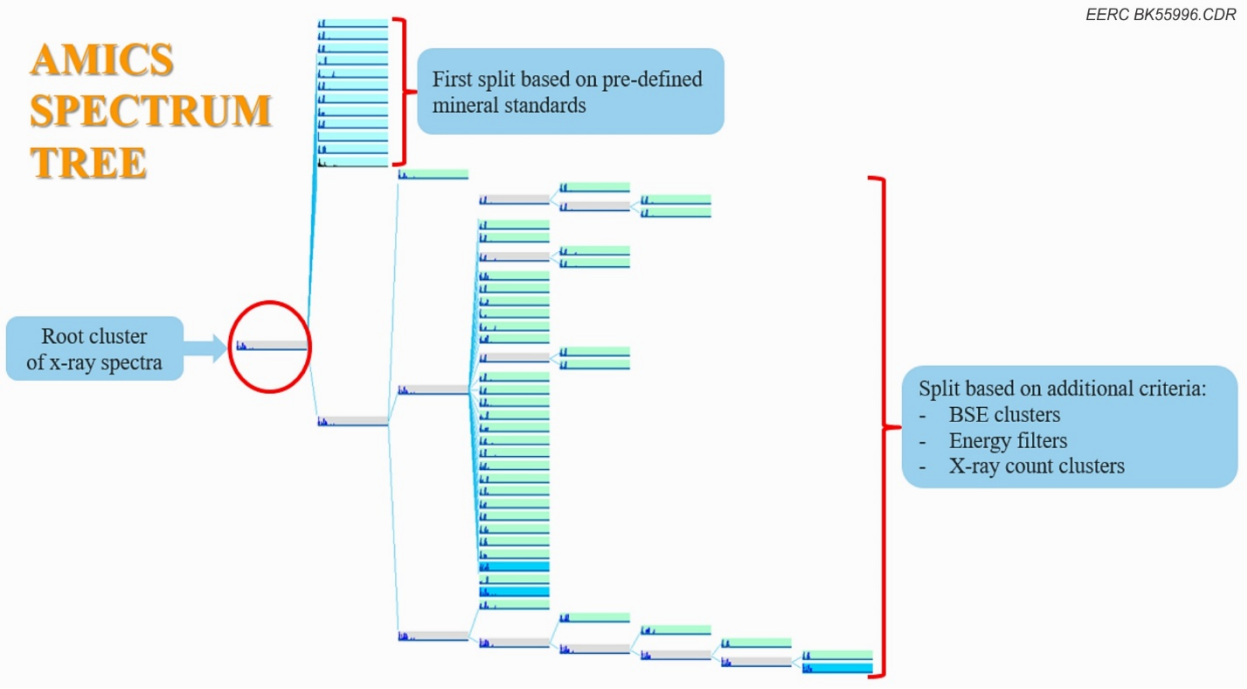

Figure A-6. Layout of AMICS spectrum tree.

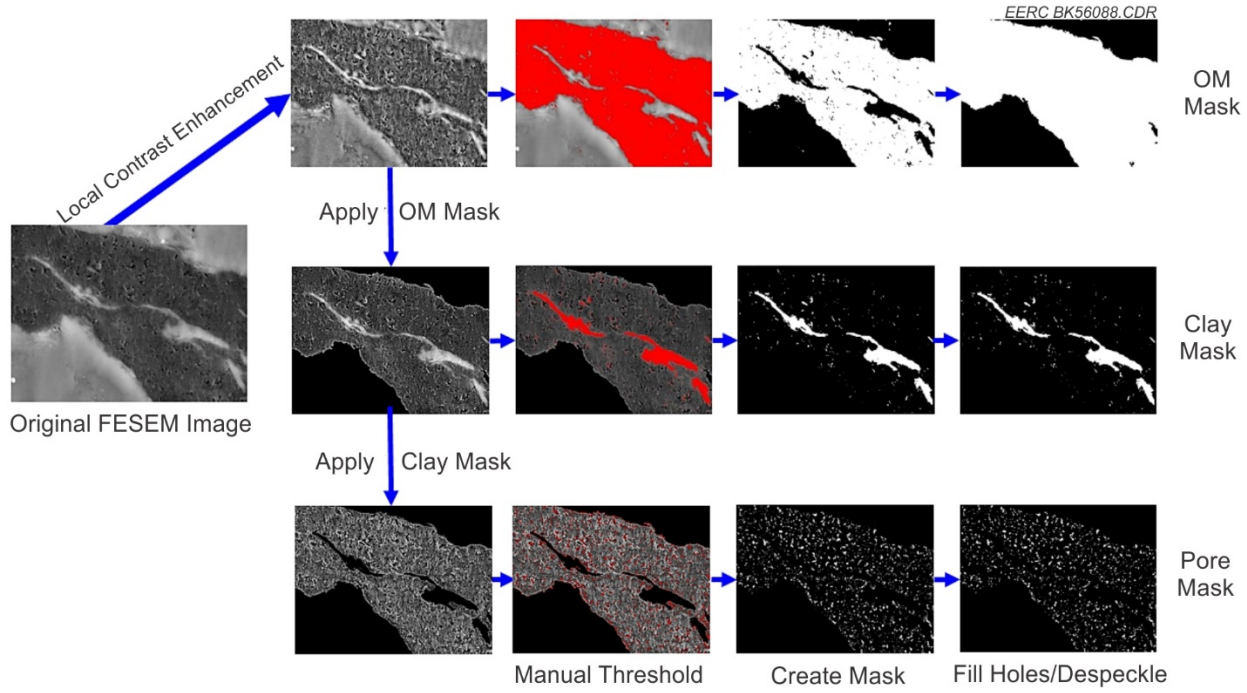

Figure A-7. Illustration of the process for creating specific feature masks.

OM Mask

- Perform local contrast enhancement on original FESEM image; call this original Image 1.
- Use manual threshold to separate OM with its embedded clay particles.
- Binarize the threshold image, file holes, and despeckle to obtain OM mask.

Clay Mask

- Apply the OM mask to original Image 1 to obtain an image of just OM matrix and embedded clays; call this original Image 2.
- Use manual threshold to separate clay particles from OM matrix in original Image 2.
- Binarize the threshold image, fill holes, and despeckle to create clay mask.

Pore Mask

- Apply the clay mask to original Image 2 to obtain an image of just OM matrix and pores; call this original Image 3.
- Use manual threshold to separate pores from OM matrix in original Image 3.
- Binarize the threshold image, fill holes, and despeckle to create pore mask.

Quality Assurance and Quality Control

To determine the quality of the feature masks in delineating the various particle types within the OM matrix, especially pores, the individual feature masks were combined and overlain on the original FESEM image for comparison. The OM, clay, and pore masks were assigned to the red, green, and blue channels, respectively, to obtain a composite RGB image of the masks. The RGB composite image was then devolved into edges of different features and overlain onto the original FESEM image for comparison. A zoomed section of the comparison image in Figure A-8 shows good agreement in the resolution of pores and clays within the OM matrix.

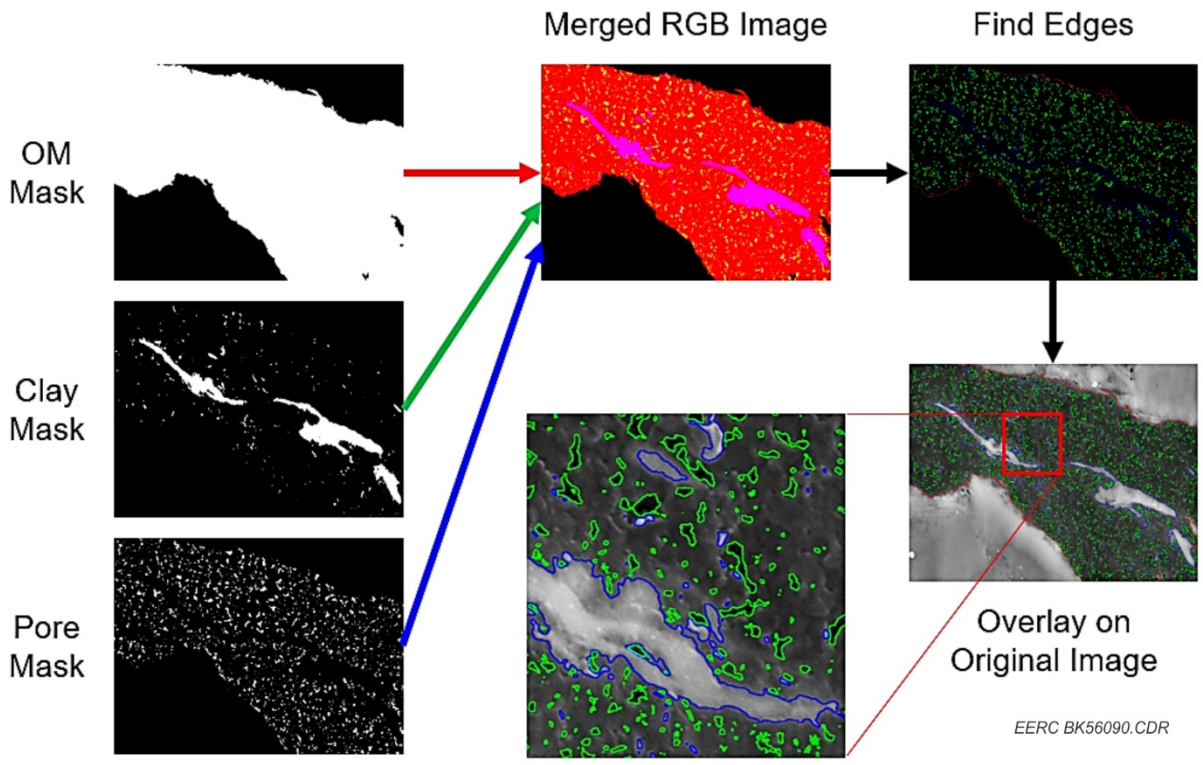

Figure A-8. Illustration of the QA/QC checks for specific feature masks.

REFERENCES

Coates, G.R., Xiao, L., and Prammer, M.G., 1999, NMR logging – principles and applications: Halliburton Energy Services, Houston, Texas, Publication H02308.

GIT – Green Imaging Technologies LithoMetrix™, 2017, www.greenimaging.com/lithometrix/ (accessed January 2017).

Glass, H.D., and Killey, M.M., 1987, Principles and application of clay mineral composition in quaternary stratigraphic—examples from Illinois, U.S.A., *in* van der Meer, J.J.M., Ed., INQUA Symposium of Genesis and Lithology of Glacial Deposits, Amsterdam, Netherlands.

Hughes, R.E., and Warren, R., 1989, Evaluation of the economic usefulness of earth materials by x-ray diffraction, *in* 23rd Forum Geology Industrial Minerals: Hughes, R.E., and Bradbury, L.C., Eds., Illinois State Geol. Surv.

Hughes, R.E., Moore, D.M., and Glass, H.D., 1994, Qualitative and quantitative analysis of clay minerals in soils, *in* quantitative methods in soil mineralogy: Soil Science Society of America, v. 677S.

Moore, D.M., and Reynolds, Jr., R.C., 1997, X-ray diffraction and the identification and analysis of clay minerals, 2nd ed.: Oxford University Press, New York.

Oxford Instruments, 2015a, NMR log calibration from laboratory core measurements: Application Note 3, www.oxford-instruments.com/products/analysers/stationary-benchtop-analyser/core-analyser-geospec2plus (accessed January 2017).

Oxford Instruments, 2015b, Rapid non-destructive capillary pressure measurements with NMR: Application Note 2, www.oxford-instruments.com/products/analysers/stationary-benchtop-analyser/core-analyser-geospec2plus (accessed January 2017).

Oxford Instruments, 2015c, Technical note – how to get the best out of your NMR system: www.oxford-instruments.com/products/analysers/stationary-benchtop-analyser/core-analyser-geospec2plus (accessed February 2017).

Oxford Instruments, 2017, NMR and core analysis–technical datasheet: www.oxford-instruments.com/products/analysers/stationary-benchtop-analyser/core-analyser-geospec2plus (accessed January 2017).